LBNL-45934

ERNEST ORLANDO LAWRENCE BERKELEY NATIONAL LABORATORY

Gradient Effects on the Fracture of Inhomogeneous Materials

Terrence L. Becker

Materials Sciences Division
Center for Advanced Materials

May 2000

Ph.D. Thesis

REFERENCE COPY
Does Not
Circulate
Bldg. 50 Library - Ref.
Lawrence Berkeley National Laboratory

LBNL-45934
Copy 1

DISCLAIMER

This document was prepared as an account of work sponsored by the United States Government. While this document is believed to contain correct information, neither the United States Government nor any agency thereof, nor The Regents of the University of California, nor any of their employees, makes any warranty, express or implied, or assumes any legal responsibility for the accuracy, completeness, or usefulness of any information, apparatus, product, or process disclosed, or represents that its use would not infringe privately owned rights. Reference herein to any specific commercial product, process, or service by its trade name, trademark, manufacturer, or otherwise, does not necessarily constitute or imply its endorsement, recommendation, or favoring by the United States Government or any agency thereof, or The Regents of the University of California. The views and opinions of authors expressed herein do not necessarily state or reflect those of the United States Government or any agency thereof, or The Regents of the University of California.

Ernest Orlando Lawrence Berkeley National Laboratory
is an equal opportunity employer.

DISCLAIMER

This document was prepared as an account of work sponsored by the United States Government. While this document is believed to contain correct information, neither the United States Government nor any agency thereof, nor the Regents of the University of California, nor any of their employees, makes any warranty, express or implied, or assumes any legal responsibility for the accuracy, completeness, or usefulness of any information, apparatus, product, or process disclosed, or represents that its use would not infringe privately owned rights. Reference herein to any specific commercial product, process, or service by its trade name, trademark, manufacturer, or otherwise, does not necessarily constitute or imply its endorsement, recommendation, or favoring by the United States Government or any agency thereof, or the Regents of the University of California. The views and opinions of authors expressed herein do not necessarily state or reflect those of the United States Government or any agency thereof or the Regents of the University of California.

LBNL-45934

Gradient Effects on the Fracture of Inhomogeneous Materials

Terrence Lee Becker
Ph.D. Thesis

Department of Mechanical Engineering
University of California, Berkeley

and

Materials Sciences Division
Center for Advanced Materials
Ernest Orlando Lawrence Berkeley National Laboratory
University of California
Berkeley, CA 94720

May 2000

This work was supported by the Director, Office of Science, Office of Basic Energy Sciences, Materials Sciences Division, of the U.S. Department of Energy under Contract No. DE-AC03-76SF00098.

Gradient Effects on the Fracture of Inhomogeneous Materials

by

Terrence Lee Becker

B.S. (University of California, Berkeley) 1994
M.S. (University of California, Berkeley) 1995

A dissertation submitted in partial satisfaction of the

requirements for the degree of

Doctor of Philosophy

in

Engineering-Mechanical Engineering

in the

GRADUATE DIVISION

of the

UNIVERSITY of CALIFORNIA, BERKELEY

Committee in charge:

Professor Robert O. Ritchie, Co-chair
Professor Panayiotis Papadopoulos, Co-chair
Professor George C. Johnson
Professor Daryl C. Chrzan

Spring 2000

Abstract

Gradient Effects on the Fracture of Inhomogeneous Materials

by

Terrence Lee Becker

Doctor of Philosophy in Engineering – Mechanical Engineering

University of California, Berkeley

Professor Robert O. Ritchie, Co-chair

Professor Panayiotis Papadopoulos, Co-chair

Functionally Graded Materials (FGMs) have a spatial variation in physical properties that can be tailored to meet the needs of a specific application and/or to minimize internal stresses arising from thermal and elastic mismatch. Modeling these materials as inhomogeneous continua allows assessment of the role of the gradient without requiring detailed knowledge of the microstructure. Motivated by the relative difficulty of obtaining analytical solutions to boundary value problems for FGMs, an accurate finite-element code is developed for obtaining numerical planar and axisymmetric linear thermoelastic solutions. In addition an approximate analytical technique for mapping homogeneous-modulus solutions to those for FGMs is assessed and classes of problems to which it applies accurately are identified. The fracture mechanics analysis of FGMs can be characterized by the classic stress intensities, K_I and K_{II}, but there has been scarce progress in understanding the role of the modulus gradient in determining fracture initiation and propagation. To address this question, a statistical fracture model is used to correlate near-tip stresses with brittle fracture initiation behavior. This

describes the behavior of a material experiencing fracture initiation away from the crack tip. Widely dispersed zones of fracture initiation sites are expected. Finite-length kinks are analyzed to describe the crack path for continuous crack growth. For kink lengths much shorter than the gradient dimension, a parallel stress term describes the deviation of the kinking angle from that for homogeneous materials. For longer kinks there is a divergence of the kink angle predicted by the maximum energy release rate and the pure opening mode criteria.

Chapter 3: An Approximate Method for Residual Stress Calculation in Functionally Graded Materials 25

3.1 Introduction 25

3.2 Problem Formulation 26

3.2.1 Residual Thermal Stresses in Elastically Homogeneous Bodies 26

3.2.2 Approximate Solution for FGMs 29

3.3 Procedures 31

3.4 Results and Discussion 33

3.4.1 Comparison with Analytical Solutions 33

3.4.2 The Axially Graded Cylinder 35

3.4.2.1 Stress Functions for an FGM Cylinder 36

3.4.2.2 Gradients with the Same Material Curvature 36

3.4.2.3 Gradients with the Differing Material Curvature 37

3.4.2.4 Sigmoidal Gradients 38

3.5 Summary 39

3.6 References 40

3.7 Figure Captions 42

Chapter 3 Figures 43-56

Chapter 4: Statistical Fracture Modeling: Crack Path and Fracture Criteria with Application to Homogeneous and Functionally Graded Materials 57

Nomenclature List 57

4.1 Introduction 58

4.2 FGM Fracture Mechanics 59

4.3 RKR Fracture Modeling 61

4.3.1 Weibull Statistics 61

4.3.2 Statistical Fracture Modeling 63

4.3.3 Crack Trajectory 65

4.4 Procedures 67

4.5 Results and Discussion 69

4.5.1 Homogeneous Body Analyses 69

4.5.1.1 Mixed-Mode Fracture Toughness 69

4.5.1.2 Mixed-Mode Initiation Angle 71

4.5.1.3 Contours of Failure Probability 72

4.5.1.4 Mean fracture Initiation Distance 73

4.5.1.5 Physical Implications 73

4.5.2 FGM Infinite Body Analyses 77

4.5.2.1 Parallel Strength gradient $\sigma_0(x)$ 78

4.5.2.2 Infinite body with parallel stiffness gradient, $E(x)$ 79

4.5.2.3 Infinite body with perpendicular strength gradient, $\sigma_0(y)$ 79

4.5.2.4 Infinite body with normal stiffness gradient, $E(y)$ 80

4.5.2.5 Implications 82

4.5.3 FEA of Finite-Sized Specimens 86

4.5.3.1 Specimen Calibration 87

4.5.3.2 SE(T) with Parallel Strength Gradient, $\sigma_0(x)$ 88

4.5.3.3 SE(T) with Parallel Modulus Gradient, $E(x)$ 88

4.5.3.4 SE(T) Specimen with Perpendicular Strength Gradient, $\sigma_o(y)$ 90

4.5.3.5 SE(T) Specimen with Perpendicular Modulus Gradient, $E(y)$ 91

4.5.3.6 M(T) Specimen with Perpendicular Modulus Gradient, $E(y)$ 92

4.5.3.7 Implications for Fracture Experiments and Application to FGMs 92

4.6 Summary and Conclusions 94

4.7 References 96

Appendix A: Monte Carlo Simulations 102

4.8 Figure captions 103

Chapter 4 Figures 106-125

Chapter 5: Finite Crack Kinking in Functionally Graded Materials 126

5.1 Introduction 126

5.2 Crack Kinking in Homogeneous Materials 126

5.3 Crack Kinking in FGMs 130

5.4 Problem Formulation 130

5.4.1 Kinked Crack Geometry 130

5.4.2 Kink Angle Selection Methodologies 132

5.4.2.1 Maximum Energy Release Rate Criteria 132

5.4.2.2 Pure Opening Mode Criteria 134

5.4.3 Procedures 135

5.5 Results and Discussion 135

5.5.1 Homogeneous Material Kink Angles 135

5.5.2 Graded Material 137

5.5.2.1 Kink Angles 137

5.5.2.2 Modulus Affected Stresses 138

5.5.2.3 Parallel Stress Approximation 139

5.5.2.4 Bifurcation in Energy Criteria 141

5.6 Concluding Remarks 142

5.7 Summary 143

5.8 References 143

5.9 Figure Captions 146

Chapter 5 Figures 148-161

List of Tables

Table 3.1 Physical constants for the materials under study 32

Table 4.1 Parameters for local maxima in cracking probability 83

Table 4.2 Effect of gradient on angular dispersion of first fracture 84

Table 5.1 Tip parameters for graded sheet 137

Table 5.2 Normalized apparent *T*-stress 140

Acknowledgments

At the completion of my work at Berkeley, I am overwhelmed by feelings of gratitude to the many people who helped me achieve my goals. First, Professor Robert Ritchie has been an exemplary thesis advisor. The level and quality of his support have been only secondary to his enthusiasm and encouragement. Through a series of intense and detailed discussions, Dr. Rowland Cannon guided my research beyond my own narrow intentions and into its present form. Dr. Jim McNaney has made himself available on innumerable occasions for consultation and has been generous with his time, opinions and computer code. I would like to also thank Dr. Tony Tomsia for his support and friendship. I thank Professor Panos Papadopoulos for his perspective, advice and excellent teaching that enabled me to tackle the problems in this dissertation.

The members at large of the Ritchie group: Alexander, Aindrea, Avinash, Brad, Chris (B., G. & M.), Don, Heeman, Jay, Josh, K.B., Ravi, Valeska all provided an cooperative and stimulating environment in which to work.

Six years of graduate school requires more than the effort of the student. I'd like to particularly acknowledge the generosity of my grandparents, Robert and Rosemary Denkewalter. It was my Grandfather who first advised me to obtain a Ph.D., as he had, and I'm happy to have received such good advice. My mother, Mary, has been unswerving in her confidence of my abilities, often in direct opposition to my own opinion regarding the challenge of the moment. My wife Camolin deserves special

recognition for not only enduring the most grueling aspects of this endeavor, but for providing me with inspiration beyond words.

Work supported by the Director, Office of Energy Research, Office of Basic Energy Sciences, Materials Sciences Division of the U.S. Department of Energy under Contract No. DE-AC03-76SF00098

Chapter 1: Introduction

1.1 FGMs: DEFINITION AND MOTIVATION

The technological motivation for the development of functionally graded materials (FGMs) is the same as for any composite material: to obtain properties unavailable in any one homogeneous material. The ultimate goal of any composite design is to achieve the best properties of the constituent materials with none of the liabilities. Invariably there are factors that mitigate the success of such a goal. Stress that arises due to the joining two dissimilar materials is one such factor. A global misfit stress is evolved when materials with differing coefficients of thermal expansion (CTE) are mated and experience a change in temperature (from processing or from in-service conditions). At a free surface of a joint, the sharp discontinuity in CTE leads to a singularity, with the linear elastic stresses approaching infinity at the surface (Muntz & Yang, 1992). The imposition of mechanical load on a joint between two materials with differing elastic stiffnesses also results in a singularity (Dunders, 1969; Bogy, 1971). For a material without layers, where the properties vary *continuously* with position, these singularities are eliminated. The remaining residual stresses can be optimized (in the context of a certain geometry and application) by varying the shape of the gradient (e.g. Tanaka *et al.*, 1996).

A gradient in properties can be designed not only to optimize the stresses, but also to be functional so that the spatial change in properties is beneficial to the application. For instance, an FGM comprised of a chemically resistant ceramic and a tough metal

could be implemented to protect a structure in a chemically aggressive environment.

Although the term "FGM" is a result of Japanese research in the 1980's (Suresh and Mortensen, 1998), materials that meet that definition are by no means recent inventions. Case hardening steel is an ancient practice, first used to increase the strength of weapons and still used in modern steel making (ASM International, 1991). This process introduces a chemical (carbon or nitrogen), and thereby mechanical hardness gradient, from the surface of a part to the interior. Furthermore, the working of cutlery blades yields a microstructure that is graded, yielding a hard cutting edge (with a fine, highly worked microstructure) on a tough (coarser microstructure) blade (Suresh and Mortensen, 1998).

Bamboo has been analyzed as a functionally graded material. Amada (1997) noted a macroscopically graded structure of the fiber in the walls of the bamboo plant. There is a higher volume-fraction of the stiff fibers in the outer part of the wall, where the bending stress from wind loading is the greatest.

A major motivation for the use of advanced ceramics and intermetallics is high-temperature service in transportation and power generation. This has also been the focus of FGM research. The development of modern nickel-based superalloys allows for the increased operating temperature and efficiency of turbines in military and civilian aircraft and electric power turbines (Sims *et al.*, 1987). Monolithic ceramics and intermetallics have not yet achieved their promise as replacement materials, mainly because of their low fracture toughness, extensive research and relative improvement notwithstanding. The coating of a high-toughness superalloy with a high melting point ceramic, typically ZrO_2, (Suresh and Mortensen, 1998) has allowed for yet higher combustor operating

temperatures.

The implantation of foreign objects into the human body (knee and hip implants, artificial teeth, etc) is an example of the need for a bio-compatibility as well as the previously mentioned structure properties (Tomsia, 2000). For applications that endure wear, FGM coatings are also used to improve tribological behavior by suppressing surface cracking (Jitcharoen *et al.*, 1998).

1.2 State of FGM fracture mechanics research

The most useful developments in linear elastic fracture mechanics (LEFM) for FGMs can be credited to Erdogan and coauthors (1985, 1995). The primary results are:

1) the form and strength of the stress singularity near the sharp tip of a linear elastic crack is the same in an FGM as in a homogeneous material, and

2) the magnitude and phase of the stress intensity factors are determined not only by the crack geometry and loading, but also by gradients in elastic modulus.

The first of these results admits a large body of LEFM literature to the study of FGMs, although under tighter restrictions than for homogeneous materials (Jin and Noda, 1996). The second result complicates study of the fracture behavior of a specific geometry, but the shielding/amplification of the stress intensity factor will not change any of the fundamental mechanics of crack growth (the effects of higher order terms on crack path stability may be greater).

The work on the toughness of FGMs has been limited. Examples include a simple rule-of-mixtures and a crack bridging model (Jin and Bata, 1996). Study of

contour integrals results in a conservation *J*-integral (Rice, 1966) analogue for FGMs with varying elastic modulus (Honein and Hermann, 1997). The toughness of an elastic-perfectly plastic FGM with varying yield strength has been established by a similar formulation (Kolednik, 2000).

1.3 Overview of this work

This project seeks to quantify the effect of gradients in elastic properties on the fracture behavior of brittle FGMs. To address the computational need for efficient mechanics analysis, a finite element routine that is capable of varying the material parameters within each finite element is developed. This program is validated and compared to using discrete inter-element changes in Chapter 2. In Chapter 3, an approximation for the stresses in FGMs with a modulus gradient was developed. This allowed the approximate solution of FGM problems based on the solution for a homogeneous material. This methodology was validated for a number of thermal stress problems, with the approximate solution coinciding to the exact in some cases.

Chapter 4 develops a statistical formulation for the fracture of brittle materials in which the modeling describes the onset of brittle fracture in terms of the material state in the neighborhood of a crack. Therefore, the influence of the gradient can be assessed via these statistical methods. The extension of the existing fracture models to mixed-mode loading yields new results for both homogeneous and inhomogeneous materials. Gradient-dominated effects are evident in both infinite bodies (formulated using the FGM approximation of Ch. 3) and finite bodies (calculated via Ch. 2's FEA). The angle of

crack initiation is drastically affected by gradients perpendicular to the crack plane.

In Chapter 5 the kink angle for continuous crack extension in a FGM is determined. The angle is determined by two criteria: that which minimizes the mechanical potential of the system and that which leads to a shear-free (mode-I) kink. For homogeneous materials and infinitely short crack lengths, these two criteria are virtually equivalent. For kink lengths smaller than the scale of the gradient, the angles determined by these two criteria are nearly the same. But, the kink angle is not entirely determined by the mode-mixity. There is as much as 10° disagreement from the angle predicted for an asymptotic kink. This can be attributed to a *T*-stress like term caused by the modulus gradient.

1.4 References

Amada, S., Ichikawa, Y., Munekata, T., Nagase, Y. and Shimizu, H. , 1997. Fiber texture and mechanical graded structure of bamboo. *Composites Part B*, 28B, 13-20.

Bogy, D., 1971. Two edge-bonded elastic wedges of different materials and wedge angles under surface tractions. *J. Appl. Mech.*, 38, 377-89.

Delale, F. and Erdogan, F., 1983. Interface crack in a nonhomogeneous elastic medium. *Int. J. Engng. Sci.*, 26, 559-68.

Dundurs, J. J. , 1969. Edge-bonded dissimilar orthogonal elastic wedges under normal and shear loading. *J. Appl. Mech.*, 36, 650-2.

Erdogan, F. and Sih, G. C. , 1963. On the crack extension in plates under plane loading and transverse shear. *J. Basic Engng.*, 85, 519-27.

Erdogan, F., 1995. Fracture mechanics of functionally graded materials. *Compos. Engng.* 5, 753-70.

Sims, C.T., Stoloff. N.S., Hagel, W.C., eds. 1987. *Superalloys II.* New York : Wiley, 1987.

Honein, T. and Hermann, G., 1997. Conservation laws in nonhomogeneous plane elastostatics, *J. Mech. Phys. Solids*, 45 789-805.

Jitcharoen, J.; Padture, N.P.; Giannakopoulos, A.E.; Suresh, S. 1998. Hertzian-crack suppression in ceramics with elastic-modulus-graded surfaces. *J. American Ceramic Soc.*, 81, 2301-8.

Kolednik, O. , 2000. The yield stress gradient effect in inhomogeneous materials. *Int. J. Solids Structures*, 37, 781-808.

Konda, N. and Erdogan, F., 1994. The mixed mode crack problem in a nonhomoegneous elastic medium. *Engng. Frac. Mech.*, 47, 533-45.

Jin, Z.-H. and Batra, R. C. , 1996. Some basic fracture mechanics concepts in functionally graded materials. *J. Mech. Phys. Solids*, 44, 1221-35.

Munz, D. and Yang, Y. Y., 1992. Stress singularities at the interface in bonded dissimilar materials under mechanial and thermal loading. *J. Appl. Mech.*, 59, 856-61.

Rice, J. R. , 1968. A path independent integral and the approximate analysis of strain concentratino by notches and cracks. *J. Appl. Mech.*, 35, 379-86.

Suresh, S., and Mortensen, A., 1998. *Fundamentals of functionally graded materials.* The University Press, Cambridge.

Tanaka, K., Watanabe, H. and Sugano, Y., 1996. A multicriterial material tailoring of a hollow cylinder in functionally gradient materials: scheme to global reduction of thermoelastic stresses. *Comput. Methods Appl. Mech. Engrg.*, 135, 369-80.

Chapter 2: Fracture and Computational Mechanics for FGMs

2.1 Introduction

This chapter briefly reviews the mechanics of functionally graded materials. Micromechanical approaches for modeling the mechanical behavior of composite materials are discussed. These formulations do not contain an explicit reference to the microstructure of the FGM, but assume that the behavior of the composite can be calculated solely from the properties and volume fractions of the constituents. Using the effective properties of the FGM and tracking the changes in the composition though the effective properties, continuum mechanics solutions are obtainable without specific microstructural modeling. A limited number of analytical solutions exist to boundary value problems for inhomogeneous linear elastic materials. The sharp crack problem is one such solution and its key features are discussed. The implementation of an FGM finite element code is validated with two example problems.

2.2 Micromechanical analysis of composite structures

The microstructure of an FGM is in large part determined by the method of processing. In general, statistically isotropic materials can be characterized as particles of material A in material B, particles of material B in material A, or an interconnected network of both A and B. In any of these cases the modeling of a composite on the microstructural level would be dominated by the particular local geometry and interface conditions. Results with more generality are obtained by analyses that study the effective properties of the composite material. The effect of the gradient in composition of an

FGM is modeled though the gradient in these effective properties.

The problem of determining the effective properties of a mixture of two materials has been long studied, with pioneering work by Maxwell, Rayleigh, and Einstien (Hashin, 1983). For simple elastic composites, modeling the structure as two springs provides wide bounds for the aggregate behavior of the composite. For two springs in parallel, the total stiffness in is the sum of the stiffnesses of the two springs, $k_t=k_1+k_2$. Likewise, the linear rule of mixtures uses a volume-fraction weighted sum of the Young's moduli to predict the Young's modulus of the composite

$$E_c = \mathrm{v}_1 E_1 + \mathrm{v}_2 E_2 \tag{2.1}$$

where v_1 and v_2 are the volume fraction of phases 1 and 2, respectively, and $\mathrm{v}_1+\mathrm{v}_2=1$. For two springs in series, the inverse of the total stiffness is the sum of the inverse stiffnesses, $1/k_t=1/k_1+1/k_2$. The inverse rule of mixtures

$$E_c = \left(\frac{1}{\mathrm{v}_1 E_1} + \frac{1}{\mathrm{v}_2 E_2} \right)^{-1} \tag{2.2}$$

yields a nonlinear relation which is dominated by the more compliant material. For specific morphologies, e.g. unidirectional fiber composites loaded along the fiber direction, the linear rule of mixtures provides the appropriate behavior. However, for more general, isotropic composites, these bounds are too wide to be considered useful predictors of composite behavior.

More stringent bounds can be found in the work of Hashin and Shtrikman (1963), which provides a set of upper and lower bounds, more narrow than the linear and inverse rules of mixture, for both bulk and shear moduli, K and μ. The "effective" elastic constants for *all* isotropic composites fall within these bounds. Important to this type of

analysis is the notion of a representative volume element (RVE). This is a volume of material within which, it is expected that all of the important microstructural features are found. Using the example of a composite with non-periodic spherical inclusions, the RVE would have to be large enough that, on average, a number of inclusions will be contained within it.

A wide variety of analysis schemes attempt to reproduce the effective elastic (or elastic-plastic) behavior of an isotropic composite. Most assume some type of geometric model (e.g., a spherical inclusion of material 1 in a matrix of material 2) and satisfy some simplified set of boundary and compatibility conditions for an RVE. An RVE of the effectively homogenized material would respond the same as the original composite. Different analyses require different combinations of the elastic constants of the constituents and/or fitting parameters. Reviews of a number of these methods is given in Christensen (1990) and Zuiker (1995), where the Self Consistent Method (SCM) (Hill, 1965), is determined to be the micromechanical theory with the characteristics most desirable for analysis of FGMs. To compare the differing predictions by these models, the effective Young's modulus for composites of materials with E_2/E_1=10, are displayed in Fig 2.1.

The effective coefficient of thermal expansion of a composite has also been modeled. In addition to a linear rule of mixtures, more advanced models weight the CTE of the constituents with their elastic properties (Hashin, 1983; Kingery *et al.*, 1965).

The accuracy of micromechanical methods can be limited when microstructure is sufficiently coarse compared to the overall geometry. In addition, many models are not accurate for mixtures of very dissimilar materials, and may result in substantial errors in

the limit of rigid inclusions, voids, or very high volume fracture of inclusions (Christensen, 1990). This limits the ability of continuum mechanics to describe the problem without detailed and expensive modeling of the microstructure. However, it is proposed that the study of the mechanics of continuously inhomogeneous materials will be beneficial to the majority of practical FGM material combinations.

2.3 Continuum mechanics for FGMs

The governing linear thermoelastic constitutive equation for an inhomogeneous material is

$$\sigma_{ij} = 2\mu(\mathbf{x})\varepsilon_{ij} + \lambda(\mathbf{x})\varepsilon_{kk}\delta_{ij} - \Delta T\alpha(\mathbf{x})(3\lambda(\mathbf{x}) + 2\mu(\mathbf{x}))\delta_{ij} \qquad (2.3)$$

and reduces to the standard equation when constant properties, μ, λ, and α, are used. The Lamé constants are related to the Young's modulus, E, and the Poisson's ratio, ν, via:

$$\mu = \frac{E}{2(1+\nu)} \qquad \lambda = \frac{\nu E}{(1-2\nu)(1+\nu)}. \qquad (2.4\ \text{a,b})$$

Included in Eq. 2.3 is the effect thermal stress, where ΔT is the change in temperature from a stress-free reference temperature and α is the linear coefficient of thermal expansion (CTE). None of the other fundamental equations of linear elasticity are affected by the materials inhomogeneity, but almost all derived equations are affected (such as the Beltrami-Mitchell equations of stress compatibility); thus standard solution methodologies are not pertinent for FGM problems.

2.4 Some boundary value problems for FGMs

The scope of solutions available in the technical literature for inhomogeneous

materials (FGMs) is much narrower than those for homogeneous materials. Nonetheless, there are a handful of solutions for linear elastic problems. For example, Lekhnitskii (1981) solved problem of the tension and the torsion of an inhomogeneous rod. This later solution was later corrected and expanded to include flexure of an inhomogeneous beam (Rooney & Ferrari, 1995). George (1976) performed similar work on axisymmetric rods. The problem of the rigid indentation a semi-infinite inhomogeneous substrate was also solved (Kassir, 1972; Kassir and Chuaprasert, 1974).

Due to the important potential of FGMs for application to high-temperature service environments (or the importance of minimizing post-processing residual stresses), a number of thermoelastic solutions have been developed. Most employ simplifying geometric assumptions, such as beam-like deformation, (Ravichandran, 1995) or spherical symmetry (Lutz and Zimmerman, 1996). For infinite bodies, the stress rise due to the material inhomogeneity was calculated by Munz and Yang (1992).

Because of the analytic complexity of mechanics problems with spatially varying E, finite element analysis (FEA) is widely used to solve problems of practical interest like the spherical indentations of an FGM (Giannakopoulos and Suresh, 1997abc) and elastic-plastic thermal stress problems (Giannakopoulos *et al.*, 1995; Rabin and Williamson *et al.*, 1996).

2.5 Linear elastic fracture mechanics for FGMs

For FGMs with a brittle phase, e.g., ceramic, intermetallic or glass, fracture is an important design limitation. If the FGM is a brittle/brittle composite (e.g., Mo/SiO_2 (Ishibashi *et al.*, 1997); Al_2O_3/Si_3N_4 (Gopal, 1997); SiC/TiC (Sand *et al.*, 1999),

ZrO_2/Al_2O_3 (Krell *et al.*, 1999)), linear elastic fracture mechanics (LEFM) can be used to characterize such failure, providing that the effects of the gradients in elastic modulus and strength are taken into account.

FGMs with sharp cracks necessitate new solutions of the elasticity problem. In a series of papers Erdogan and co-authors (Delale and Erdogan, 1983; Konda and Erdogan, 1994; Erdogan, 1995) considered Mode-I, -II, and –III cracks in FGMs with constant Poisson's ratios and Young's moduli which vary exponentially with distance. FGM fracture mechanics share features of that for cracks in homogeneous materials and for cracks in discrete interfaces between dissimilar elastic materials.

For locations asymptotically close to the tip of the crack, the Williams (1957) solution for homogeneous materials describes the stress state in an FGM. That is, the strength of the elastic stress singularity is $\sigma \rightarrow 1/\sqrt{r}$ as $r \rightarrow 0$. Furthermore, the angular variation of the stresses is identical to that for the homogeneous case. This is referred to as the K-dominant region.

The form of the stress solution leads to an unambiguous definition of the stress intensity factors K_I, K_{II}, which have the same physical interpretation as in the homogeneous case. K_I and K_{II} characterize the magnitude of the symmetric (opening) and nonsymmetric (sliding) in-plane deformation modes. (K_{III} characterizes out-of-plane shear and will not be discussed further.) This is in contrast to the case of interface cracks, where the strength of the stress singularity is a function of the elastic mismatch and the distinction between tension- and shear-mode stress intensities is lost (Rice, 1985). Like the interface case, the determination of the value of $K_{I,II}$ for a given geometry and loading is influenced by the elastic properties. For cracks running parallel to the direction of the

gradient, "far field" mode-I loading[1] results in a pure mode-I crack opening. The value of K_I will be affected by the gradient such that the tip may be shielded (K_I reduced) compared to the same crack geometry in a homogeneous material. However, for cracks that grow at an angle with the gradient, mode-mixity is developed where the crack tip exhibits both normal and shear deformations.

The presumed existence of the Williams crack-tip field in a material with varying modulus would violate the conditions of compatibility in linear elasticity. Therefore, for distances away from the crack-tip (at locations with modulus different from that at the tip) the stress field must take on a different character. Jin & Batra (1994) performed an asymptotic analysis on the incompatibility created by using the Williams stress solution in an inhomogeneous material and estimated the size of the K-dominant region. They state that the homogeneous equation will govern over a region with near the crack tip where $\frac{\nabla E}{E} << \frac{1}{r}, \frac{\nabla^2 E}{E} << \frac{1}{r^2}$. Therefore the size of the K-dominant region is limited by the "steepness" of the modulus variation. There is sparse accounting for this effect in the literature. For a mixed-mode crack in a material with $E(x,y)/E(0,0) = e^{(\beta \cdot x + \gamma \cdot y)}$, Konda and Erdogan (1995) describe the stress field near the crack as

$$\sigma_{ij} \approx \frac{E(x,y)}{E(0,0)}\left[\frac{K_I}{\sqrt{2\pi r}} f_{ij}^{I}(\theta) + \frac{K_{II}}{\sqrt{2\pi r}} f_{ij}^{II}(\theta)\right] \tag{2.4}$$

where the quantity in brackets is the Williams (1957) solution. This gives the first-order

---

[1]Far field loading refers to loading conditions irrespective of the material gradient. It is determined by nature of the crack-tip solution for the same geometry in the homogeneous case.

description of the effect of the modulus gradient on the stress behavior; although it is not an exact solution for finite r, it is valid over a larger region than the strict K-dominant region.

The path independent property of the J-integral (Rice, 1966) is lost when applied to a material with varying modulus. Honein and Hermann (1997) formulated a path-independent integral for FGMs, J_e, which includes terms relating to the modulus gradient in the plane of the crack. A J-integral methodology was used to calculate the effect variation in yield strength on resistance to crack growth (Kolednik, 2000). The analysis of the effects of material gradient on the fracture toughness of an FGM has included a rule of mixtures analysis to assess the fracture resistance as a function of location as well as a crack bridging analysis (Gu & Asaro, 1997).

2.6 A FINITE ELEMENT PROGRAM FOR FGMS

The spatial variation of the thermoelastic constants in the FGM problem induces the substantial complication of non-constant coefficients in the set of governing equations. The computer program FEAP (Finite Element Analysis Program) (Zienkiewicz and Taylor, 1989) was used to used to calculate the approximate solutions to linear thermoelastic boundary value problems for FGMs. For an FGM problem, the effect of material gradient effects two steps in the finite element algorithm. First, the elasticity matrix D_{ij} is proportional to E and is used in the calculation of the element stiffness matrix $K_{ij}^{e} = \int B_i^T D_{ij}(\mathbf{x}) B_j dV$. Second, for thermal stress problems the forcing

vector $f_j^e = -\int B_i^T D_{ij}(\mathbf{x})\alpha(\mathbf{x})\Delta T dV$ contains variable $D_{ij}(\mathbf{x})$ and $\alpha(\mathbf{x})$. Last, any stress calculation must also take into account $E(x)$, $\nu(x)$, and $\alpha(x)$ via Eq 2.3. Each of these procedures requires calculations based on the location of the Gauss points. For a 9-node quadrilateral element, a quadratic variation in each in-plane direction can be accomplished within a single element.

The solution to the FGM problem could also be accomplished by assigning a single set of elastic constants to each element, based on an average location of its nodes, for instance. However, the variation of the elastic constants within each element yields superior results. Two test cases are used to verify the accuracy of this formulation.

2.7 CODE VALIDATION PROBLEMS

2.7.1 Elastic graded film on a rigid substrate

Figure 2.2 displays the in-plane stress for a thin film on a rigid substrate subject to a uniform change in temperature. This is a simplified model of the common problem of the development of stresses in a thin metallic film deposited on a thick, stiff, low-CTE substrate. The CTE is constant, with the Young's modulus varying sigmoidaly with z. The analytical solution for this problem is obtained for zero in-plane displacements, with the corresponding stress being $\sigma = -\alpha\ \Delta T\ E(z)$. The improved accuracy of the FGM finite element scheme over a multi-layer approximation is apparent.

2.7.2 A rigid indentor in contact with a graded elastic half-space

A rigid punch impinging on a graded material with a shear modulus varying with depth has been solved analytically (Kassir and Chuapraser, 1974; Kassir,1972) to model

the effect of varying soil response on structures. To further verify the validity of the finite element formulation, this problem was analyzed using the mesh displayed in Fig 2.3. To minimize the effects of the boundary conditions, a large disk was modeled, with the radius being ten times that of the indentor. The axial stress, σ_{zz} under the indentor is displayed in Fig 2.4 for $\mu(z) = \mu_o(1+z/c)^b$ with c=0.5 and b=0.75. Also shown for comparison is the homogeneous solution for $\mu=\mu_o$. The finite element solution well matches the analytical solution, capturing the strength of the elastic singularity near the corner of the indentor.

2.8 Conclusions

The solution to the elastic crack problem has been obtained in the asymptotic near-tip limit. This allows the interpretation of stresses in terms of the classic fracture mechanic parameters. For problems without analytical solutions, finite element analysis can be used to approximate the stresses. The use of finite elements that allows for internal property variation dramatically increases the accuracy of results compared to element-wise homogeneous solutions.

2.9 References

ASM International Handbook Committee, 1991. *Metals Handbook: v4. Heat Treatment Revised ed.*, ASM International Materials Park, Ohio.

Christensen, R. M. , 1990. A critical evaluation for a class of micro-mechanics models. *J. Mech. Phys. Solids*, 38, 379-404.

Delale, F. and Erdogan, F. , 1983. Interface crack in a nonhomogeneous elastic medium. *Int. J. Engng. Sci.*, 26, 559-68.

Dundurs, J. J. , 1969. Edge-bonded dissimilar orthogonal elastic wedges under normal and shear loading. *J. Appl. Mech.*, 36, 650-2.

Erdogan, F. and Sih, G. C. , 1963. On the crack extension in plates under plane loading and transverse shear. *J. Basic Engng.*, 85, 519-27.

Erdogan, F., 1995. Fracture mechanics of functionally graded materials. *Compos. Engng.* 5, 753-70.

George, O. D. , 1976. Torsion of an elastic solid cylinder with a radial variation in the shear modulus. *J. Elasticity*, 6, 229-44.

Giannakopoulos, A. E., Suresh, S., Finot, M. and Olsson, M. , 1995. Elastoplastic analysis of thermal cycling layered materials with compositional gradients. *Acta Metall. Mater.*, 43, 1335-54.

Giannakopoulos, A. G. and Suresh, S. , 1997. Indentation of solids with gradients in elastic properties. I. Point force. *Int J. Solids Struct.*, 34, 2357-92.

Giannakopoulos, A. G. and Suresh, S. , 1997. Indentation of solids with gradients in elastic properties. II. Axisymmetric indentors. *Int J. Solids Struct.*, 34, 2393-428.

Giannakopoulos, A. G. and Suresh, S. , 1997. Spherical indentation of compositionally graded materials: theory and experiments. *Acta. Mater.*, 45, 1307-21.

Gopal, M. (1997). Joining of silicon nitride ceramics to itself and to the other materials using chemically compatible interlayers. Ph.D. thesis, Dept. Mater. Sci. Miner. Engng., Berkeley, University of California.

Gu, P., Dao, M., Asaro, R.J., 1999. A simplified method for calculating the crack-tip field of functionally graded materials using the domain integral. *J. Appl. Mech.*, 66, 101-8.

Hashin, Z. , 1983. Analysis of composite materials – A survey. *J. Appl. Mech.*, 105, 481-505.

Hashin, Z. and Shtrikman, S. , 1963. A variational approach to the theory of elastic behavior of multiphase materials. *J. Mech. Phys. Solids*, 11, 127-40.

Hill, R. , 1965. A self-consistent mechanics of composite materials. *J. Mech. Phys. Solids*, 13, 213-22.

Honein, T. and Hermann, G., 1997. Conservation laws in nonhomogeneous plane elastostatics, *J. Mech. Phys. Solids*, 45 789-805.

Ishibashi, H., Saiz, E. and Tomsia, A. P. , 1997. Mo/SiO2 FGMs fabricated by slip casting. *Am. Ceram. Soc. Bull.*, 76, 231.

Jin, Z. and Noda, N. , 1994. Crack-tip singular fields in nonhomogeneous materials. *J. Appl. Mech.*, 61, 738-40.

Jin, Z.-H. and Batra, R. C. , 1996. Some basic fracture mechanics concepts in functionally graded materials. *J. Mech. Phys. Solids*, 44, 1221-35.

Kassir, M. K. , 1972. Boussinesq problems for nonhomogeneous solid. *J. Engrg. Mech. Division, ASCE*, 98, 457-70.

Kassir, M. K. and Chuaprasert, M. F. , 1976. A rigid punch in contact with a nonhomogeneous elastic solid. *J. Appl. Mech.*, 41, 1019-24.

Kolednik, O. , 2000. The yield stress gradient effect in inhomogeneous materials. *Int. J. Solids Struct.*, 37, 781-808.

Konda, N. and Erdogan, F., 1994. The mixed mode crack problem in a nonhomoegneous elastic medium. *Engng. Frac. Mech.*, 47, 533-45.

Kingery, W. D., Bowen, H. K. and Uhlmann, D. R. , 1965. *Introduction to Ceramics*, Second Edition. Wiley and Sons, New York.

Krell, T., Schulz, U., Peters, M., Kayseer, W.A., 1999. Grade EB-PVD alumina-zirconia thermal barrier coatings-an experimental approach. *Mater. Sci. Forum* 308-311, 396-401.

Lekhnitskii, S. G. , 1981. *The Theory of Elasticity of an Anisotropic Body*. Mir, Moscow.

Lutz, M. P. and Zimmerman, R. W. , 1996. Thermal stresses and effective thermal expansion coefficient of a functionally gradient sphere. *J. Thermal Stress*, 19, 39-54.

Munz, D. and Yang, Y. Y., 1992. Stress singularities at the interface in bonded dissimilar materials under mechanical and thermal loading. *J. Appl. Mech.*, 59, 856-61.

Rabin, B. H. and Williamson, R. L. , 1996. The Effect of Interlayer Properties on Residual Stresses in Ceramic-Metal Joining. In: I. E. Reimanis, C. H. Henager, and A. P. Tomsia, eds. *Ceramic Joining: Ceramic Transactions*, 77, 137-148.

Ravichandran, K. S. , 1995. Thermal residual stresses in a functionally graded material system. *Mater. Sci. Engng.* A, A201, 269-76.

Rice, J. R., 1968. A path independent integral and the approximate analysis of strain concentration by notches and cracks. *J. Appl. Mech.*, 35, 379-86.

Rice, J. R. , 1988. Elastic fracture mechanics concepts for interfacial cracks. *J. Appl. Mech.*, 55, 98-103.

Rooney, F. J. and Ferrari, M. , 1995. Torsion and flexure of inhomogeneous elements. *Compos. Engrg.*, 5, 901-11.

Sand, Ch., Adler, J., Lenk, R., 1999. A new concert for manufacturing sintered materials with a three dimensional composition gradient using a silicon carbide-titanium carbide composite. *Mater. Sci. Forum* 308-311, 65-70.

Suresh, S., and Mortensen, A., 1998. *Fundamentals of functionally graded materials.* The University Press, Cambridge.

Singh, B. M. , R. S. Dhaliwal. Asymmetric problem of a Griffith crack in a nonhomogeneous medium under shear. *J. Elasticity*, 8, 313-8.

Williams, M. L. , 1957. On the stress distribution at the base of a stationary crack. *J. App. Mech.*, 79, 109-14.

Williamson, R. L., Rabin, B. H. and Byerly, G. E. , 1995. FEM study of the effects of interlayers and creep in reducing residual stresses and strains in ceramic-metal joints. *Composites Engineering*, 5, 851-63.

Zienkiewicz, O. C. and Taylor, R. L. , 1987. *The Finite Element Method.* McGraw-Hill, New York, N.Y.

Zuiker, J. R. , 1995. Functionally graded materials: choice of micromechanical model and limitations in property variation. *Composites Engineering*, 5, 807-19.

2.9 FIGURE CAPTIONS

Figure 2.1 Effective modulus for an isotropic composite of two materials with $E_2/E_1=10$ under various micromechanical theories, including the Hashin-Shtrikman bounds and the Self-Consistent Method.

Figure 2.2 In-plane thermal stresses for a thin FGM film bonded to a rigid substrate. Analytical solution is $\sigma = -\alpha\, \Delta T\ E(z)$. The accuracy of stepwise homogeneous elements (with internally constant E) is compared to that of an inhomogeneous element with $E(z)$.

Figure 2.3 Mesh used to analyze the impinging of a graded half-space by a rigid flat indentor. To minimize the effects of the finite geometry, a large mesh was used, with an outer radius ten times that of the indentor.

Figure 2.4 Axial stress, σ_{zz}, under the face of the indentor modeled in Figure 2.3. Comparison of FEA with FGM element and analytical solution. The elastic singularity at the corner is captured as the mesh is refined. The solution for a homogeneous material is included for comparison.

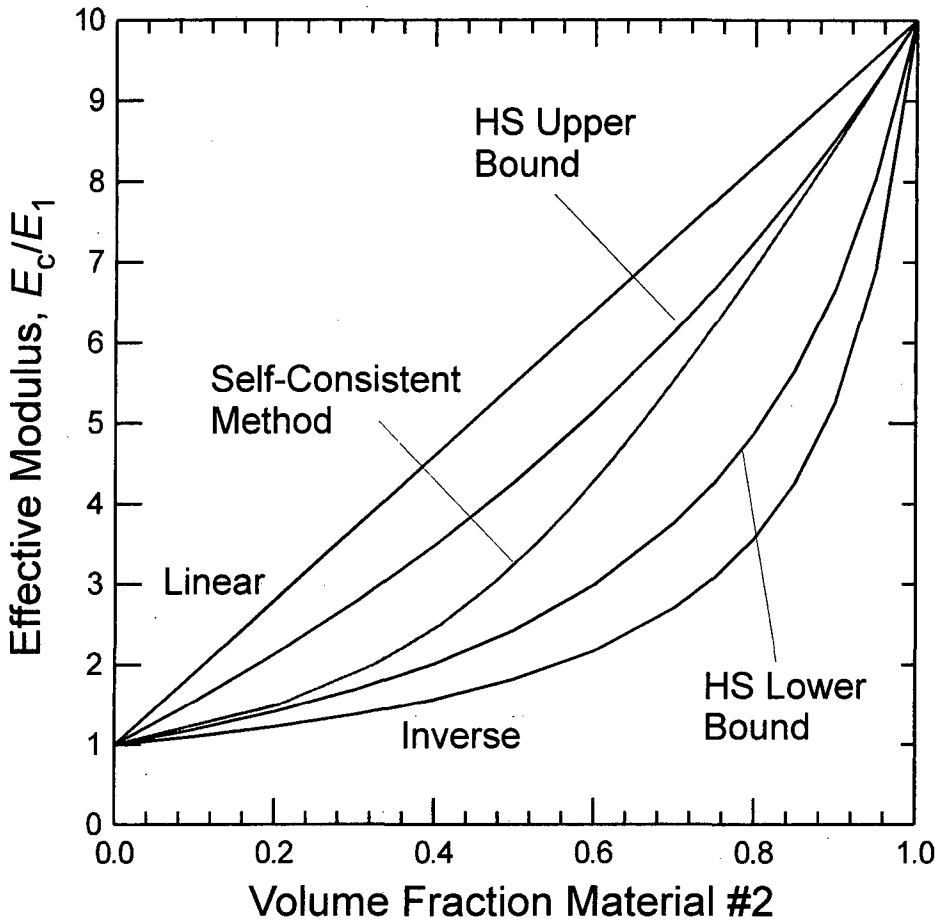

Figure 2.1 Effective modulus for an isotropic composite of two materials with E_2/E_1=10 under various micromechanical theories: the Hashin-Shtrikman bounds, the linear and inverse rules of mixture and the Self-Consistent Method.

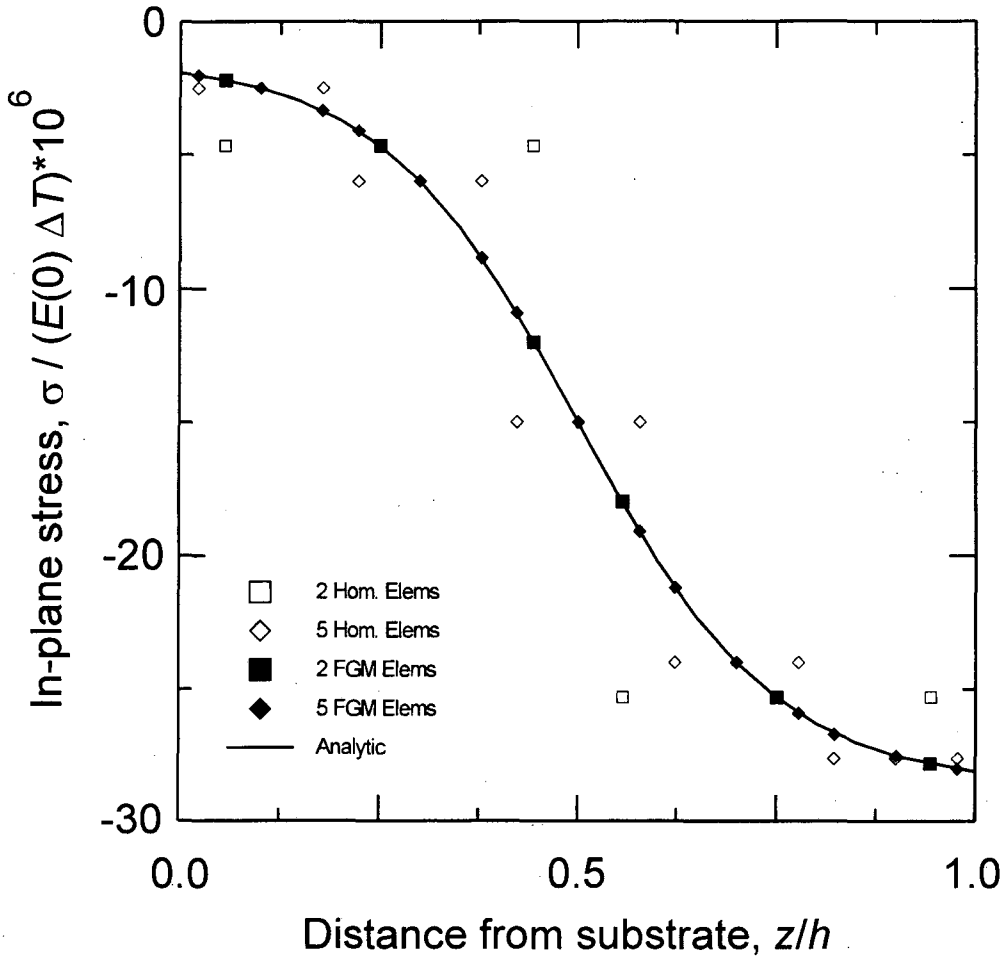

Figure 2.2 In-plane thermal stresses for a thin FGM film bonded to a rigid substrate. Analytical solution is $\sigma = -\alpha\ \Delta T\ E(z)$. The accuracy of stepwise homogeneous elements (with internally constant E) is compared to that of an inhomogeneous element with $E(z)$.

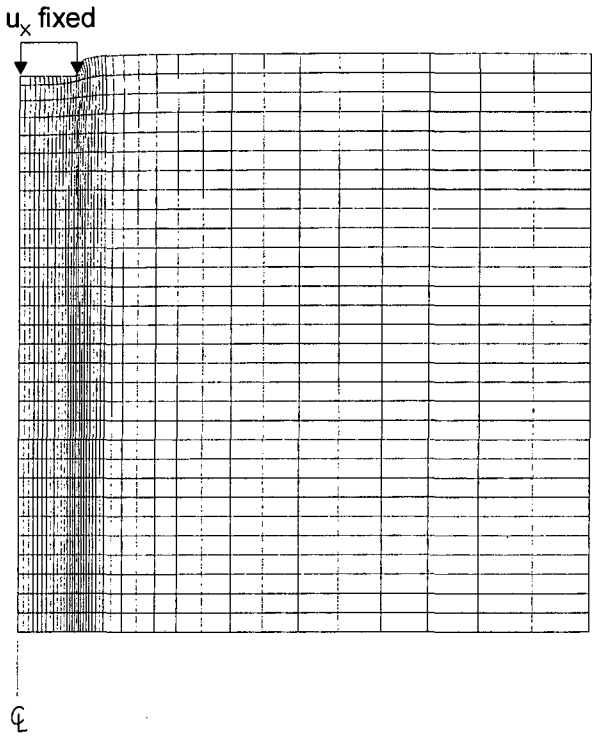

Figure 2.3 Mesh used to analyze the impinging of a graded half-space by a rigid flat indentor. To minimize the effects of the finite geometry, a large mesh was used, with an outer radius ten times that of the indentor.

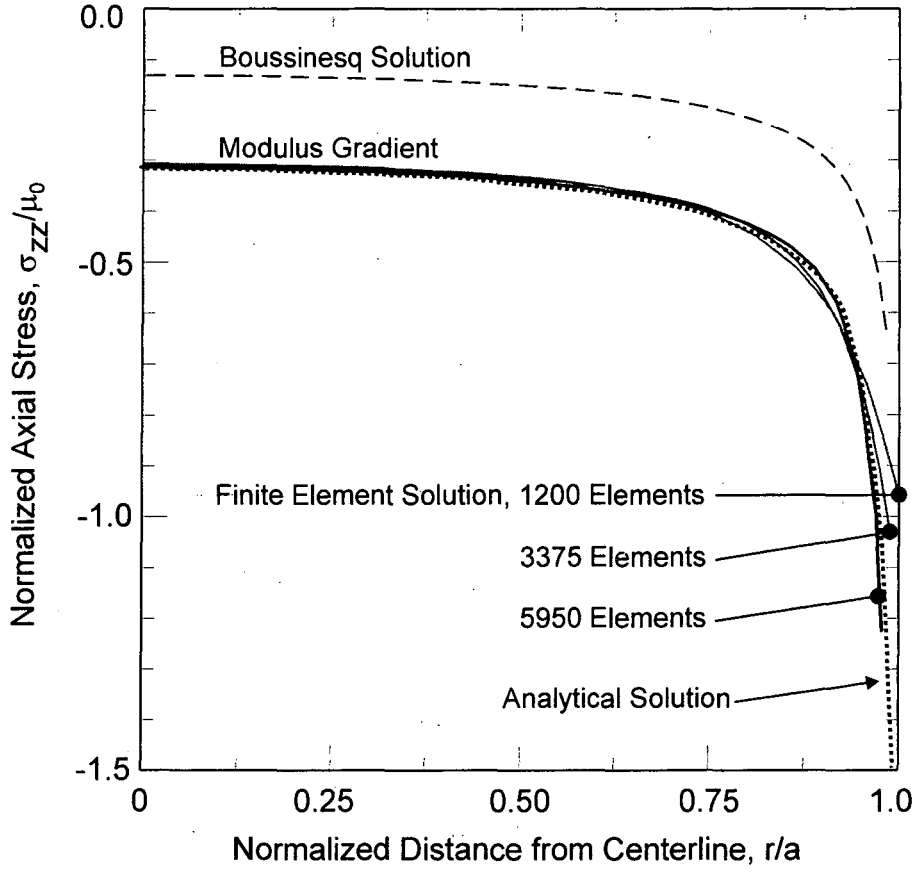

Figure 2.4 Axial stress, σ_{zz}, under the face of the indentor modeled in Figure 2.3. Comparison of FEA with FGM element and analytical solution. The elastic singularity at the corner is captured as the mesh is refined. The solution for a homogeneous material is included for comparison.

Chapter 3:

An Approximate Method for Residual Stress Calculation in Functionally Graded Materials

3.1 Introduction

In many joining and composites problems, residual stresses, arising either from processing or from in-service temperature variations, are important. The determination of the optimal thermal stress state needs to incorporate the thermal and mechanical properties of the constituents as well as their variation. The optimization of such stresses is a critical design goal and a driving force in FGM research. Indeed, several studies have focused on the experimental (Delfosse *et al.*, 1992) and theoretical assessment of these stresses in FGMs. Simple analyses yield results for which residual stress can be eliminated (e.g., Giannakopoulos *et al.*, 1995); however, this may not provide the optimum mechanical performance. The generation of surface compressive residual stress can result in superior strengths and fracture resistance compared to the stress-free configuration for both ductile and brittle materials (eg, shot-peened aircraft components and tempered glass, respectively).

The effect of composition shape on residual thermal stresses has been studied for both the elastic and elastic-plastic conditions (Rabin *et al.*, 1998, Giannakopoulos *et al.*, 1995; Grujicic and Zhao, 1998). However, the complicating effect of modulus variation with position severely limits the scope of problems that can be solved analytically. A majority of this analytical work has been for FGM films or other simple structures, for

which geometric assumptions allow for much simplified 1-D linear elastic calculations (Lutz & Zimmerman, 1996; Ravichandran, 1995; Obata & Noda, 1994; Tanaka *et al.*, 1996; Tanigawa *et al.*, 1996; Markworth and Saunders, 1995). For a more general 2-D or 3-D problem, numerical methods such as finite element analysis (FEA) are required. These are, by comparison, costly, as a full analysis for each material pairing, geometry and gradient must be performed.

In the present study, a method for estimating the influence of elastic gradients on the stress state of an FGM is considered. Analytical thermal stress solutions as well as finite element calculations are used for a variety of problems with varying modulus. Model material systems, Mo-SiO_2 and Ni-Al_2O_3, were used for numerical examples. The approximate method was found to be very accurate for a number of important problems. The use of this methodology allows for the application of thermal stress solutions for homogeneous materials to FGMs.

3.2 Problem Formulation

The full description of the thermal stress problem in an FGM must include the variation in modulus. However, most standard thermoelastic analyses pertain to materials with constant E. These equations are recapitulated to provide groundwork for the discussion of the FGM problem.

3.2.1 Residual Thermal Stresses in Elastically Homogeneous Bodies

The residual thermal stress state of an elastic body subject to temperature change ΔT is considered. This ΔT is assumed to vary smoothly with position in one arbitrary direction (with cartesian coordinate x) and will be described by a polynomial function of

position, $\Delta T(x) = \sum_{i=0}^{m} \delta_i x^i$. For a homogeneous thermoelastic body with free boundaries and constant coefficient of thermal expansion (CTE) α, Young's modulus E and Poisson's ratio ν, stresses can be computed from the spatial derivatives of the Goodier potential (Boley & Winer, 1985). This potential is obtained from a weighted integration of the temperature field over the body. The stresses are therefore linearly related to each of the coefficients of the temperature field, δ_i, or equivalently, to $\alpha\delta_i$.

A smoothly varying composition in an FGM will result in smoothly varying effective thermomechanical properties, and the Goodier potential argument can be used to analyze the residual stresses arising from CTE gradients in elastically homogeneous materials. This is true because temperature change and CTE only appear as the product $\alpha\Delta T$ in the uncoupled thermoelastic problem and therefore the Goodier framework for $\Delta T(x)*\alpha$ solves the identical problem[1] as for $\alpha(x)*\Delta T$. The problem of variable $\alpha(x)$ and constant ΔT is representative of the behavior of an FGM after processing at high temperature, e.g. sintering or CVD.

For FGMs, it is natural to formulate the problem in terms of the gradient in the composition, rather than directly in terms of $\alpha(x)$. Assuming that the volume fraction, v, of material #2 in a matrix of material #1 varies as a polynomial function in one dimension:

$$v(x) = v_0 + v_1 x^1 + v_2 x^2 + \cdots + v_n x^n = \sum_{i=0}^{n} v_i x^i \qquad (3.1)$$

[1] This, of course, does not guarantee that there can exist such a steady-state temperature field, but rather if one existed, its stress state would be the same as that of the FGM under consideration.

then with the coefficient of thermal expansion assumed to be a linear function of composition

$$\alpha = \alpha_1 + (\alpha_2 - \alpha_1)\mathrm{v} = \alpha_1 + \Delta\alpha\mathrm{v} \tag{3.2}$$

it follows that:

$$\alpha(\mathrm{x}) = \alpha_1 + \mathrm{v}_0\Delta\alpha + \sum_{i=1}^{n}\Delta\alpha\mathrm{v}_i\mathrm{x}^i \,. \tag{3.3}$$

For a material with constant modulus E_o, Eq. 3.3 combined with the implications of the Goodier potential arguments yields

$$\sigma_{jk} = \Delta\alpha\Delta TE_o\sum_{i=1}^{n}\mathrm{v}_i S_{jk}^i + (\alpha_1 + \Delta\alpha v_0)\Delta TE_o S_{jk}^0 \tag{3.4}$$

where $S_{jk}^i = \sigma_{jk} / \Delta\alpha\Delta TE$ is the nondimensional *stress function* for the *jk* component of stress associated with degree *i* of the gradient polynomial. Practically, these stress functions can be obtained via the Goodier potiential, or any other analytical, numerical or experimental method.

If variation of $\alpha\Delta T$ is linear in each of the cartesian coordinates, then the body remains stress-free (Boley and Winer, 1985) and $S_{jk}^o = S_{jk}^1 = 0$. Therefore,

$$\sigma_{jk} = \Delta\alpha\Delta TE_o\sum_{i=2}^{n}\mathrm{v}_i S_{jk}^i \tag{3.5}$$

This equation yields information on how the materials properties and the gradient shape affect the residual stress state of the FGM with constant modulus. Namely, the residual stresses are linear in the difference in thermal expansion, total temperature change, elastic modulus, and in each coefficient of a polynomial gradient shape, v_i.

3.2.2 Approximate Solution for FGMs

Exact analytical solutions to problems with $E(x)$ are rare. To explore the possibility of constructing an approximate FGM solution from that of a homogeneous body, the solution to the FGM problem is decomposed into two separate displacements,

$$\boldsymbol{u} = \boldsymbol{u}^{o} + \boldsymbol{u}' \tag{3.6}$$

(see Fig 1). The first displacement field, $\boldsymbol{u}^{o}$ represents the solution to the residual stress problem with $\alpha\Delta T\,(x)$ and a constant E=E_o (Fig 3.1a). The stresses that arise, σ^{o}, are the same as in Eq 3.5. Applying the linear strain-displacement equations, it follows that $\varepsilon = \varepsilon^{o} + \varepsilon'$. These strains can be substituted in the stress-strain relation (in indicial notation)

$$\sigma_{ij} = 2\varepsilon_{ij}\mu(x) + \lambda(x)\varepsilon_{kk}\delta_{ij} - (3\lambda(x) + 2\mu(x))\Delta T\alpha(x)\delta_{ij} \tag{3.7}$$

$$\mu(x) = \frac{E(x)}{2(1+v_o)} \qquad \lambda(x) = \frac{v_o E(x)}{(1-2v_o)(1+v_o)} \tag{3.8}$$

Identifying the stresses for the E_o (and therefore λ_o and μ_o) case and those associated with the displacements $\boldsymbol{u}'$:

$$\sigma_{ij}^{o} = 2\varepsilon_{ij}^{o}\mu_o + \lambda_o\varepsilon_{ij}^{o}\delta_{ij} - (3\lambda_o + 2\mu_o)\Delta T\alpha(x)\delta_{ij} \tag{3.9}$$

$$\sigma_{ij}' = 2\varepsilon_{ij}'\mu(x) + \lambda(x)\varepsilon_{kk}'\delta_{ij} \tag{3.10}$$

yields

$$\sigma_{ij} = \sigma_{ij}^{o}\frac{E(z)}{E_o} + \sigma_{ij}'. \tag{3.11}$$

For cases in which the stresses caused by the gradient are small,

$$\sigma_{ij} \approx \sigma_{ij}^{o}\frac{E(x)}{E_o}. \tag{3.12}$$

Formally, the analysis in Section 3.2.1 is only applicable to materials with homogeneous elastic constants. However, it is clear that Eq. 3.12 can be attained by substituting $E(x)$ for E_o in Eq. 3.5, $\sigma_{jk} \approx \Delta\alpha\Delta T E(x)\sum_{i=2}^{n} \mathrm{v}_i S^i_{jk}$.

Comparing Eq. 3.11 and Eq. 3.12, it is clear that σ'_{ij} represents the error in the approximation, arising from modulus gradient induced displacements, u'_i. This approximate method will be most successful in cases where the gradient in modulus affects the displacements the least. It is now possible to investigate the nature of this error. Enforcing the balance of linear momentum by taking "$\nabla\bullet$" on both sides of Eq. 3.11 and noting that $\nabla\bullet\sigma = \nabla\bullet\sigma^o = 0$ leads to

$$\nabla \cdot \sigma' + \frac{\nabla E(x)}{E_o} \cdot \sigma^o = 0 \cdot \tag{3.13}$$

These are the equilibrium equations for a material subjected to a body force. Now the problem of determining the error σ' is re-cast to that of the linear elastic problem of a inhomogeneous body (E=$E(x)$) with a traction-free surface, subjected not to a temperature change, but only to the body force $\boldsymbol{b} = \frac{\nabla E(x)}{E_o} \cdot \sigma^o$. This, however, is still not a trivial problem and can only be used to identify the trends in the error.

Due to the linearity of this body force problem, it follows that the magnitude of the error stress will scale with $\boldsymbol{b}$, $\sigma' \propto \frac{\nabla E(x)}{E_o} \cdot \sigma^o$. More specifically, the error in the approximation enumerated in Eq. 3.12 scales linearly with: 1) the slope of the gradient in $E(x)$, and 2) with the magnitude of the stress in the homogeneous (E=E_o) solution. The first of these conclusions meets our expectations that at an interface between two

materials with $E_1 \neq E_2$, the stresses are known to be singular, which here corresponds to the fact that ∇E is not defined.

In lieu of the solution to this body force problem, a number of FMG thermal stress problems are considered as examples of the application of the approximate method. In addition to a series of analytical solutions, finite element calculations have been performed for an FGM cylinder in order to explore a range of material combinations and gradient shapes and to determine the accuracy of the approximation.

3.3 Procedures

In analyzing the thermal stresses of FGMs, we consider using the full finite element solution taking into account both CTE and modulus variation. The geometry chosen for FEA was a "short" cylinder (length to radius ratio, L/R_o = 5), with the compositional gradient lying along the z-direction. The material composition is taken to be constant in both the radial and circumferential directions. However, this is a geometry for which symmetry places no useful (non-trivial) restrictions on the residual stress state (Hoger, 1986) and is not amenable to approximate methods that rely on Saint-Venant arguments (e.g., Nikishin, 1966). Two different material sets were considered, namely molybdenum - silica and nickel - alumina. The Mo-SiO_2 system is used in an arc-lighting application and the Ni-Al_2O_3 is a common model system for numerical studies, with application to thermal barrier coatings. These represent two contrasting types of systems, with the higher coefficient of thermal expansion material having higher modulus in the first, and lower in the second. The room temperature moduli were used; however, the

CTE that was used was the average between 25 and 1000 °C. The values of the constants are given in Table 3.1 (Touloukian, 1975; Touloukian, 1977).

Table 3.1: Physical constants for the materials under study

	Molybdenum	SiO_2	Nickel	Al_2O_3
α (ave) (10^{-6} m/m)	5.72	0.5	16.43	8.8
E (GPa)	320	72	207	380
ν	0.30 ($\approx$ 0.25)	.20 ($\approx$ 0.25)	0.33 ($\approx$ 0.25)	0.23 ($\approx$ 0.25)

The residual stresses were calculated via the finite element method, using the computer program FEAP (Zienkiewicz & Taylor, 1989). The problem was analyzed in axisymmetric mode using a mesh of 400-1100 nine-node quadrilateral FGM elements. E was varied as a function of composition as prescribed by the Self Consistent Method (SCM) (Hill, 1965), which has been determined to be the micromechanical theory with the characteristics most desirable for analysis of FGMs (Zuiker, 1995). Consideration was given to other micromechanical methods and differences in the results were negligible.

The difficulty of implementing the SCM is that it does not, in general, allow explicit correlation between volume fraction and stiffness. However, this relation can be inferred via a curve fit of the effective modulus. This resulted in the variation of Young's modulus and fitted polynomial coefficients displayed in Fig. 3.2. Poisson's ratio was assumed to be constant ($\nu = 0.25$) in this analysis. The small magnitude of such variation is neglected for simplicity. The CTE was assumed to be a linear function of composition (Eq. 3.2).

3.4 Results and Discussion

3.4.1 Comparison with Analytical Solutions

As mentioned in Section 3.1, elasticity problems with varying modulus are much more difficult to solve than those with constant E, and therefore only the simplest one-dimensional cases can be considered. For the problems that can be solved analytically, restrictions must usually be placed on the allowable form of modulus variation. Specifically, a linear variation of modulus will be considered, varying from E_{metal} to $E_{ceramic}$. Similarly, unless specified otherwise the CTE was varied linearly from α_{metal} to $\alpha_{ceramic}$. This does not necessarily represent the solution to problems for any specific material gradient, linear or otherwise. These analyses are formulated in terms of E and α; in contrast, problems formulated in terms of the material gradient parameters, v_i, will be addressed in Section 3.4.2.

Several simple FGM structures were analyzed and their thermal stress state computed, some self-constrained, other constrained by bonding to a massive material with α=0. This exact solution is compared to that of homogeneous "average modulus" problem with $E_{ave} = (E_{metal} + E_{ceramic})/2$ and to the approximate solution (Eq. 3.12).

For the film on a rigid substrate with α=0 (Fig. 3.3) the solution displacement, $\boldsymbol{u}$, is independent of the modulus variation, therefore the approximate method yields the exact solution. These solutions of do not require any specific form of $E(z)$ (although a linear function was used for the data in Fig. 3.3). The general form for the residual stress after a temperature change, ΔT, is

$$\sigma_{xx} = \sigma_{yy} = -\frac{E(z)\alpha(z)\Delta T}{(1-\nu)} \quad . \qquad (3.14a,b)$$
$$\sigma_{zz} = 0$$

Also consider the problem of an axially graded peg in a rigid hole. If only radial contraction is restricted and the ends are free, then Eq. 3.14 represents the solution as well. If axial motions are also fixed, then for a peg with a small diameter the solution displacement will tend towards $\boldsymbol{u} = \mathbf{0}$. Normal stresses will coincided with Eq. 3.14(a) after scaling by a factor of $(1-2\nu)/(1-\nu)$.

Lutz & Zimmerman (1996) solved the problem of an FGM sphere with free boundaries and with modulus and CTE being linear functions of radial position. The analytical solution was applied for both material sets for both the full $E(r)$ and $\alpha(r)$ problem and for homogeneous E_o. The homogeneous solution was used to compute the "average modulus" and approximate (Eq. 3.12) stress states. Fig. 3.4 displays their exact solution for tangential stress, $\sigma_{\theta\theta}$, with the approximate method and with the homogeneous E_{ave} solution. Eq. 3.12. was found to well incorporate the modulus effect, mapping the linear variation of stress (as seen in the "average E" dashed line) into a nonlinear distribution more like the full solution. Although at $r = 0$ the difference between the exact and the approximate is large (40% in the Mo-SiO_2 case), at the location of greatest importance for particle cracking, $r = R_o$, the difference is only 10%. Ignoring the effect of varying modulus, as in the E_{ave} case, leads to ~10 times the error at the surface.

For the free beam with a linear E gradient (similar to Giannakopoulos *et al.*, 1995), a linear $\alpha(z)\Delta T$ will cause the beam to bend, but will result in a stress-free final configuration. Therefore, the beam problem was chosen with $\alpha(z) = \alpha_{metal}$ +

$(\alpha_{ceramic} - \alpha_{metal})(z/H)^2$, with the resulting stresses displayed in Fig. 3.5. For both the materials sets, Eq. 3.12 skews the symmetric stress variation (as in the "average E" dashed line) such that stresses are higher in the region with the stiffer material.

For a film sandwiched between two rigid platens (α=0) (Fig. 3.6) the approximate solution does not yield accurate results. The cause of this is the redistribution of strain (compared to the homogeneous E case) from stiffer regions to more compliant regions. A simple case to consider would be that of two springs in series held at constant non-zero displacement. As the stiffness of one spring increased, its displacement would decrease, requiring an increase in displacement in the other spring.

Highly constrained problems represent the upper bound for thermal stresses, which, in the absence of this internal redistribution will tend to the exact $\boldsymbol{u}$=**0** solution discussed previously. For bodies with finite thickness, however, displacements will be affected by E(z) such that Eq. 3.12 is inaccurate. In contrast, for bodies that are free to expand at their boundaries (such as deposited films or ceramics manufactured by free sintering), it is clear that Eq. 3.12 can provide accurate (or exact) results.

3.4.2 The Axially Graded Cylinder

The joining of a metal/glass seal is one potential application for FGMs (Ishibashi *et al.*, 1997). FGM parts are manufactured using a free-sintering method where the residual stresses arise from the cool-down from the sintering temperature. The corresponding mechanics problem is that of a right cylinder with free boundaries and the gradient along the z-direction. This is a two-dimensional problem, allowing contraction

in both the radial and axial directions. Lacking an analytical solution to this problem, FEA is used to compare the approximate method to complete FGM solutions.

3.4.2.1 Stress Functions for an FGM Cylinder

Using methods described in Section 4.3 (with constant modulus), the stress functions were calculated. The stress functions $S^2_{zz}, S^2_{\theta\theta}, S^3_{zz}$ and $S^3_{\theta\theta}$, i.e., those corresponding to the residual cool-down stress for quadratic and cubic gradients, are shown in Figs. 3.7a and 3.7b, at the centerline (r = 0) and surface ($r = R_o$). Fig. 3.8 displays the radial variations midway along the cylinder, $z = L/2$. Note that at the centerline, the circumferential and radial stress components are equal ($S^i_{rr} = S^i_{\theta\theta}$ at $r = 0$), as dictated by equilibrium considerations, and at the free lateral surface, $S^i_{rr} = 0$.

3.4.2.2 Gradients with the Same Material Curvature

Since the constant and linear aspects of a thermal gradient do not contribute to the residual stress state, the deviation from linearity can be considered to be the "driving force" for residual thermal stresses. As discussed earlier, for problems with constant modulus, the residual stresses scale exactly linearly with the magnitudes of these deviations (the coefficients v_i, $i \geq 2$) . Therefore, for such a material, the three gradients in the insert of Fig. 3.9, each with v_2 = -0.001/mm^2, will result in an identical residual stress state. However, for a Ni-Al_2O_3 FGM, with the moduli of the components differing by 83%, the residual stresses will increase with increasing average gradient slope (and, in this case, average Al_2O_3 volume fraction). This is shown by the symbols in Fig. 3.9, which represent the centerline stresses per degree of cool-down, calculated via FEA. This demonstrates that the effect of the gradient in elastic modulus on the residual stress

state is substantial and that the deviation from linearity does not entirely predict the result (~20% difference between the cases). However, using the homogeneous stress function S_{zz}^2 and by employing the approximation in Eq. 3.12 (solid lines), it is apparent that the error incurred is slight (less than 1% error between Eq. 3.12 and the full FEA results). Restated, for problems with variations in both thermal and elastic constants, the effect of modulus mismatch can be captured quite accurately by Eq. 3.12.

3.4.2.3 Gradients with the Differing Material Curvature

In addition to comparing gradients with the same curvature, the series in Fig. 3.10 can be considered. For each gradient, the composition changes smoothly from 10% to 90% ceramic with the balance being the metal phase. Each gradient is a quadratic function of axial position with v_2 = 0.002, 0.001, 0.0, -0.001, and -0.002 mm^{-2}. Both of the material systems were considered for each of the gradients and the axial residual stresses per degree of cool-down $\sigma_{zz} / |\Delta T|$ are displayed as symbols in Figs. 3.11a,b and 3.12a,b. The strong influence of gradient curvature on residual stress can be seen in both figures.

Results are broadly similar between the two material systems, with a few noticable differences. For gradients with a positive curvature ($v_2 > 0$), the residual stress is compressive on the surface ($r = R_o$). For brittle materials where the overall strength is greatly controlled by surface flaws, this can be regarded as a more favorable condition than stress-free.

As can be seen in Fig. 3.10, the relation between v_2 and σ postulated in Eq. 3.12 holds well even including the effects of $E(z)$. For some composites, Eq. 3.2 may not hold and a nonlinear compostion-CTE relation should be used. In such a case the achievement of a favorable compressive stress-state upon cool-down would be dependent not on $v_2 = \frac{1}{2}\frac{d^2v}{dz^2} > 0$ but on $\frac{d^2\alpha}{dz^2} = \left(\frac{\partial v}{\partial z}\right)^2 \frac{\partial^2\alpha}{\partial v^2} + \frac{\partial^2 v}{\partial z^2}\frac{\partial\alpha}{\partial v} < 0$. Both $\frac{d\alpha}{dv}$ and $\frac{d^2\alpha}{dv^2}$ would be determined by the specific micromechanical model used, but for a typical metal/ceramic FGM the former would be expected to be negative (ie, $\alpha_{ceramic} < \alpha_{metal}$). Therefore, for a quadric material gradient a positive value of $v_2\Delta\alpha\Delta T$ would still be desirable.

The solids lines in Figs. 3.11a,b and 3.12a,b represents the application of Eq. 3.12. The stress states of the SiO_2-Mo system are more asymmetric in the z-direction due to the greater mismatch in Young's modulus. It is apparent that this is a good approximation for either material system, although the error incurred is greater for the larger curvatures. This follows because the coupling effect of elastic gradient change and residual stress, as described in Section 4.2.2.

3.4.2.4 Sigmoidal Gradients

Previous discussion has been limited to polynomial gradients. For certain problems a polynomial description of the gradient is advantageous and allows the superposition of $\alpha\Delta T$ fields. However, Eq. 3.12 is in no way restricted to such gradients.

Sigmoidal gradient shapes are important since they simulate grading resulting from the interdiffusion of two materials.

Hyperbolic tangent gradients are shown in the insert of Fig. 3.13 and the surface residual stresses calculated via FEA for the Ni-Al_2O_3 system are displayed as the symbols in Fig. 3.13. The approximation (Eq. 3.12) results are shown as solid lines.

For the sigmoidal gradient, areas of positive gradient curvature correspond to a beneficial compressive stress at the surface. Likewise, areas of negative gradient curvature correspond to a tensile stress, in agreement with the results for the quadratic gradients (Fig. 3.12b).

As in the case of the pure quadratic, the approximation for the residual stresses works well; however, the error in the steepest of the sigmoidal gradients is indicative of the limitations of this procedure for problems with rapid changes in modulus. Still, for the sharpest gradient studied the error in the approximation of the maximum σ_{zz} was less than 15% even though the transition from 10% to 90% Al_2O_3 took place within a distance of $L/5$.

3.5 Summary

A method is presented for approximating the residual stress state in an FGM structure with free surfaces. For FGM films, the results of the approximation coincide with the exact solution. Numerical solutions for an FGM cylinder have shown this method to be accurate within 15% for all gradients studied. The method allows the application of a wide class of homogeneous-modulus residual stress analyses to FGMs. This allows, at lower cost than a full finite element analysis, the identification of

favorable and unfavorable aspects of the gradient nonlinearity, for either avoiding stresses or building desirable compressive stresses.

3.6 References

Boley, B. and Winer, J. ,1985. *Theory of Thermal Stresses*. R. E. Krieger Pub. Co., Malabar, Fla.

Christensen, R. M. , 1990. A critical evaluation for a class of micro-mechanics models. *J. Mech. Phys. Solids*, 38, 379-404.

Delfosse, D., Kunzi, H.-U. and Ilschner, B. ,1992. Experimental determination of residual stresses with a one-dimensional gradient of composition. *Acta Metall. Mater.*, 40, 2219-24.

Giannakopoulos, A. E., Suresh, S., M.Finot and Olsson, M. ,1995. Elastoplastic analysis of thermal cycling: layered materials with compositional gradients. *Acta Metall. Mater.*, 43, 1335-54.

Grujicic, M. and Zhao, H. ,1998. Optimization of 316 stainless steel/alumina functionally graded material for reduction of damage induced by thermal residual stresses. *Mater. Sci. Eng A*, A252, 117-32.

Hill, R. ,1965. A self-consistent mechanics of composite materials. *J. Mech. Phys. Solids*, 13, 213-22.

Hoger, A. ,1986. On the determination of residual stress in an elastic body. *J. Elasticity*, 16, 303-24.

Ishibashi, H., Saiz, E. and Tomsia, A. P. ,1997. Mo/SiO_2 FGMs fabricated by slip casting. *Am. Ceram. Soc. Bull.*, 76, 231.

Lutz, M. P. and Zimmerman, R. W. ,1996. Thermal stresses and effective thermal expansion coefficient of a functionally gradient sphere. *J. Thermal Stress*, 19, 39-54.

Markworth, A. J. and Saunders, J. H. ,1995. A model of structure optimization for a functionally graded material. *Mater. Letters*, 22, 103-7.

Nikishin, V. S. ,1966. *Thermal stresses in a composite cylinder with an arbitrary temperature distribution along its length.* Plenum Press, Data Division, New York.

Obata, Y. and Noda, N. ,1994. Steady thermal stresses in a hollow circular cylinder and a hollow sphere of a functionally gradient material. *J. Thermal Stresses*, 17, 471-87.

Rabin, B. H., Williamson, R. L., Bruck, H. A., Wang, X.-L. *et al.*, 1998. Residual strains in Al_2O_3 joint bonded with a composition interlayer: experimental measurements and FEM analysis. *J. Amer. Cer. Soc.*, 81, 1541-9.

Ravichandran, K. S. ,1995. Thermal residual stresses in a functionally graded material system. *Mater. Sci. Engng. A*, A201, 269-76.

Tanaka, K., Tanaka, Y., Enomoto, K. and Poterasu, V. F. , 1993. Design of thermoelastic materials using direct sensitivity and optimization methods. Reduction of thermal stresses in functionally gradient materials. *Comp. Methods. App. Mech. Engng.*, 106, 271-84.

Tanaka, K., Watanabe, H. and Sugano, Y. ,1996. A multicriterial material tailoring of a hollow cylinder in functionally gradient materials: scheme to global reduction of thermoelastic stresses. *Comput. Methods Appl. Mech. Engrg.*, 135, 369-80.

Tanigawa, Y., Akai, T., Kawamura, R. and Oka, N. , 1996. Transient heat conduction and thermal stress problems of a nonhomogeneous plate with temperature-dependent material properties. *J. Thermal Stresses*, 19, 77-102.

Touloukian, Y. S., ed. ,1975. Thermal expansion-metallic elements and alloys. *Thermophysical Properties of Matter*, New York, IFI/Plenum.

Touloukian, Y. S., ed. ,1977. Thermal expansion-nonmetallic solids. *Thermophysical Properties of Matter*, New York, IFI/Plenum.

Zienkiewicz, O. C. and Taylor, R. L. ,1987. *The Finite Element Method.* McGraw-Hill, New York, N.Y.

Zuiker, J. R. ,1995. Functionally graded materials: choice of micromechanical model and limitations in property variation. *Compos. Engng.*, 5, 807-19.

3.7 FIGURE CAPTIONS

Figure 3.1 (a) Motion of a homogeneous body with $E=E_o$ under thermal loading, $\alpha\Delta T(x)$, resulting in displacements $\boldsymbol{u}^o$ and stresses σ^o

(b) Motion of an inhomogeneous body with $E=E(x)$. The displacements, $\boldsymbol{u}$, are decomposed into the homogeneous solution displacements, $\boldsymbol{u}^o$, and the displacements due to the modulus gradient, $\boldsymbol{u}'$.

Figure 3.2 Variation of effective Young's modulus, E, with composition for Mo-SiO_2 and Ni-Al_2O_3 composites according to the self-consistent method (SCM).

Figure 3.3 FGM film on a rigid substrate undergoing temperature change ΔT. For this geometry the approximate solution coincides with the analytical.

Figure 3.4 FGM sphere undergoing free expansion. Note the order of the materials for this case: (a) Mo to SiO_2 and (b) Al_2O_3 to Ni (from stiffer to more compliant) is dictated by the restrictions on the analytical solution (Lutz and Zimmerman, 1996).

Figure 3.5 FGM beam allowed to bend due to nonlinear CTE variation through its thickness.

Figure 3.6 FGM film sandwiched between rigid platens undergoing temperature change ΔT. The redistribution of strain as a function of local modulus leads to a solution that is not amenable to this approximate method.

Figure 3.7 (a) Quadratic stress function, S_{ij}^2, along the centerline (r = 0) and surface (r = R_o) for stress components ij = $\theta\theta$, zz. (b) Cubic stress function, S_{ij}^3, along the centerline (r = 0) and surface (r = R_o) for stress components ij = $\theta\theta$, zz.

Figure 3.8 (a) Radial variation of S_{ij}^2 and (b) of S_{ij}^3 at $z = L/2$.

Figure 3.9 The axial residual stress component, σ_{zz}, resulting from the three quadratic gradients (insert), each with the same curvature (v_2 = -0.001 mm^{-2}). The approximation of Eq. 3.12 for each of the gradients (solid lines) closely matches the finite element results (closed symbols).

Figure 3.10 A series of gradients with varying curvatures. The symbol on each curve indicates the value of the curvature such that the symbols +, ▲, ●, ■, ♦ correspond respectively to v_2 =-0.002, -0.001, 0.0, 0.001, and 0.002 mm^{-2}.

Figure 3.11 Residual stresses along the centerline resulting from the gradients in Fig 3.10 for the (a) Mo-SiO_2 and the (b) Ni-Al_2O_3 system. FGM calculations (symbols) are accurately approximated by Eq. 12 (solid lines).

Figure 3.12 Residual stresses along the surface resulting from the gradients in Fig. 3.10 for the (a) Mo-SiO_2 and the (b) Ni-Al_2O_3 system. FGM calculations (symbols) are accurately approximated by Eq. 12 (solid lines).

Figure 3.13 The surface residual *zz*-stresses resulting from the series of sigmodial gradients (insert). The finite element results (symbols) are approximated by Eq. 3.12 (lines).

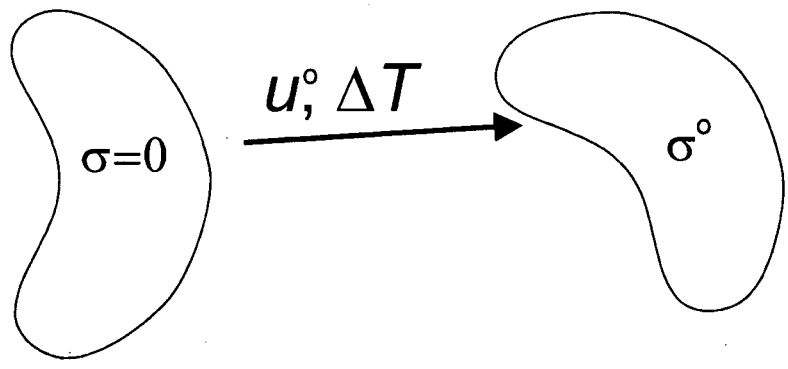

(a)

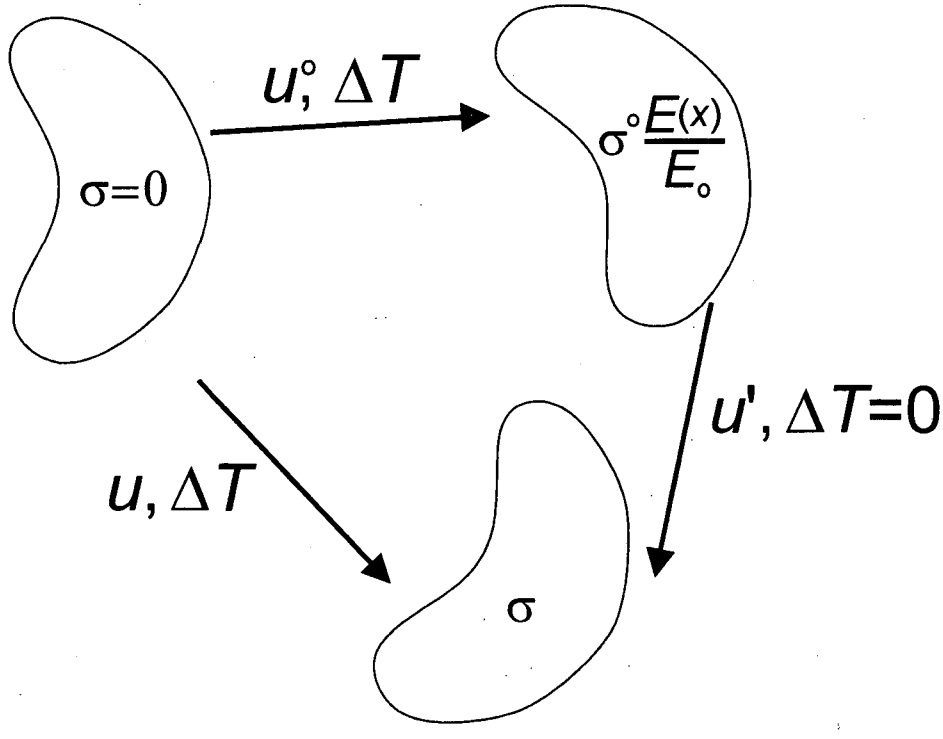

(b)

Figure 3.1 (a) Motion of a homogeneous body with $E=E_0$ under thermal loading, $\alpha\Delta T(x)$, resulting in displacements $\boldsymbol{u}^o$ and stresses σ^o

(b) Motion of an inhomogeneous body with $E=E(x)$. The displacements, $\boldsymbol{u}$, are decomposed into the homogeneous solution displacements, $\boldsymbol{u}^o$, and the displacements due to the modulus gradient, $\boldsymbol{u}'$.

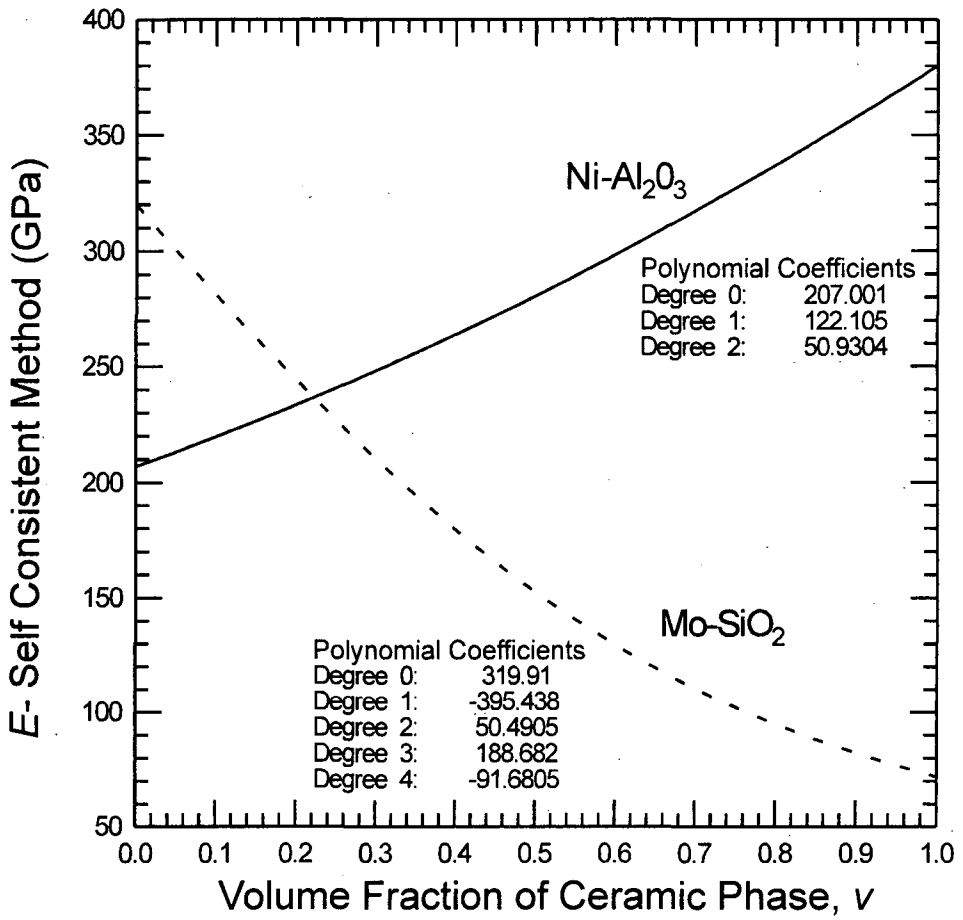

Figure 3.2 Variation of effective Young's modulus, E, with composition for Mo-SiO_2 and Ni-Al_2O_3 composites according to the self-consistent method (SCM).

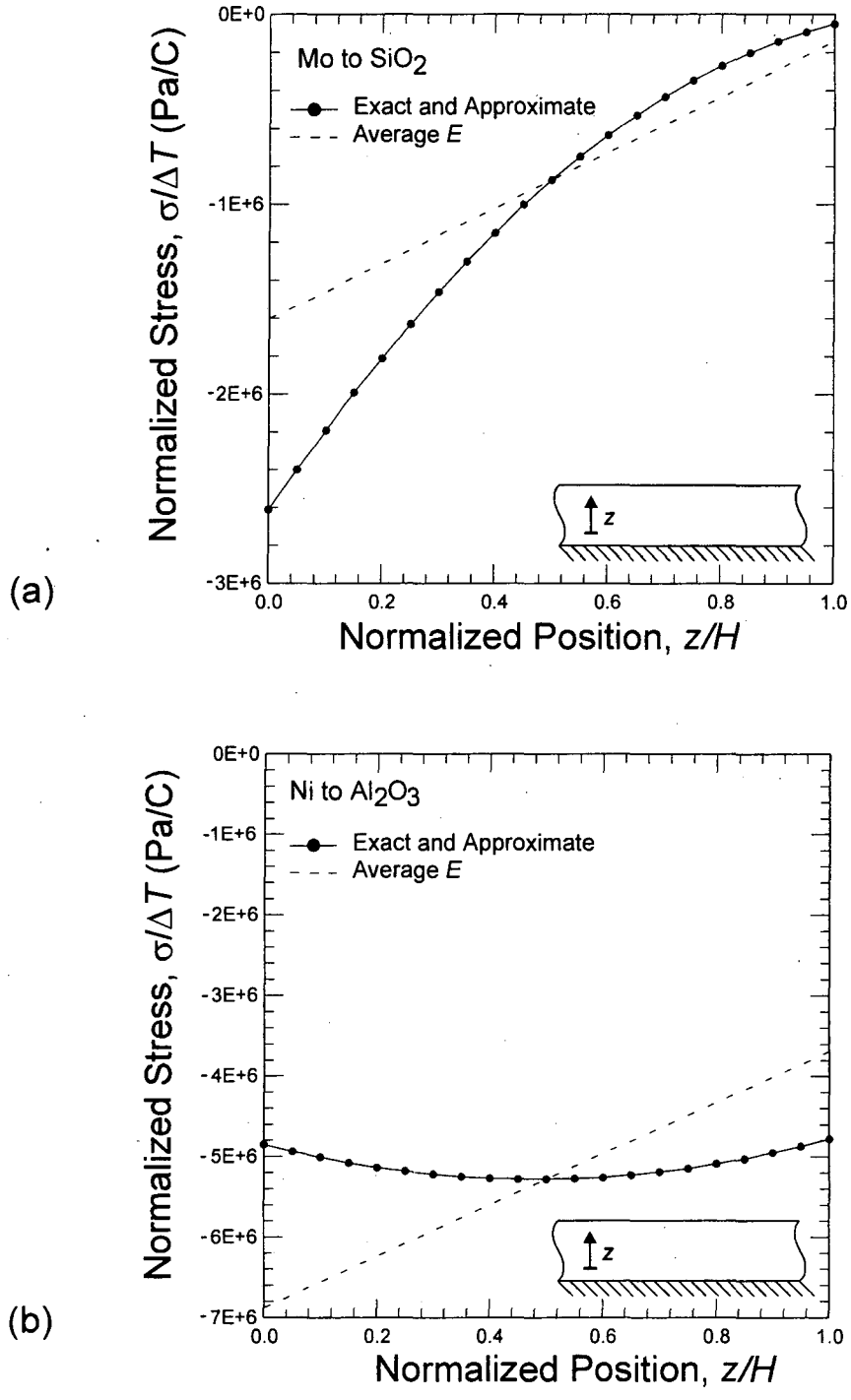

Figure 3.3 FGM film on a rigid substrate undergoing temperature change ΔT. For this geometry the approximate solution coincides with the analytical.

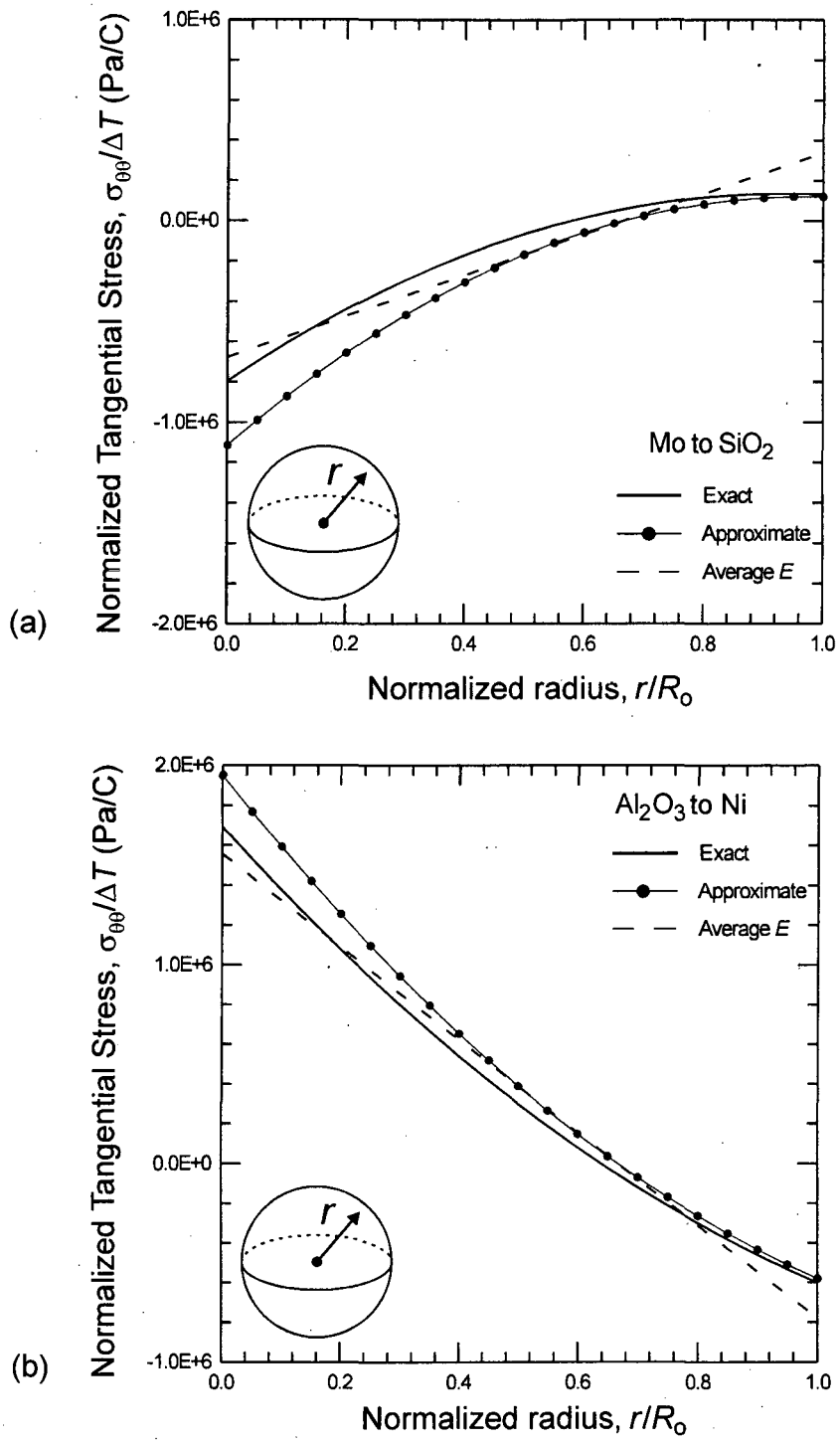

Figure 3.4 FGM sphere undergoing free expansion. Note the order of the materials for this case: (a) Mo to SiO_2 and (b) Al_2O_3 to Ni (from stiffer to more compliant) is dictated by the restrictions on the analytical solution (Lutz and Zimmerman, 1996).

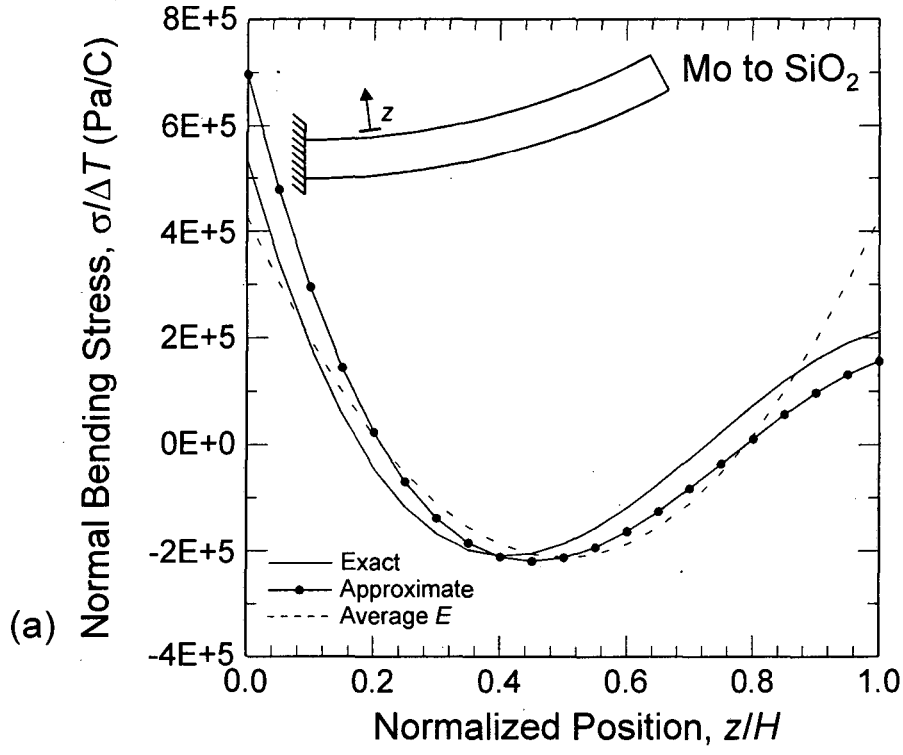

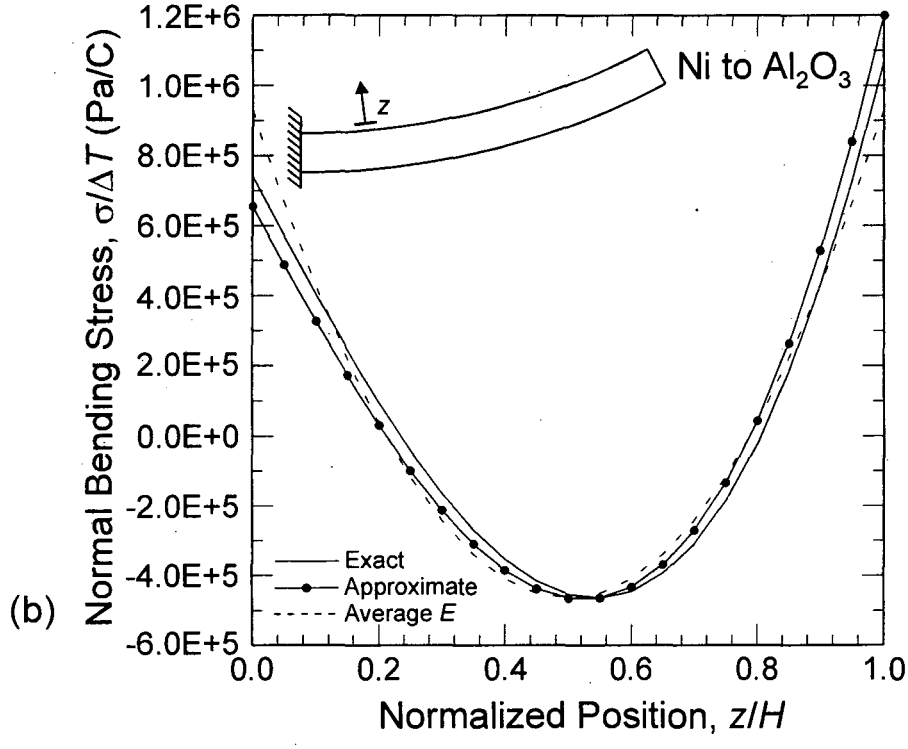

Figure 3.5 FGM beam allowed to bend due to nonlinear CTE variation through its thickness.

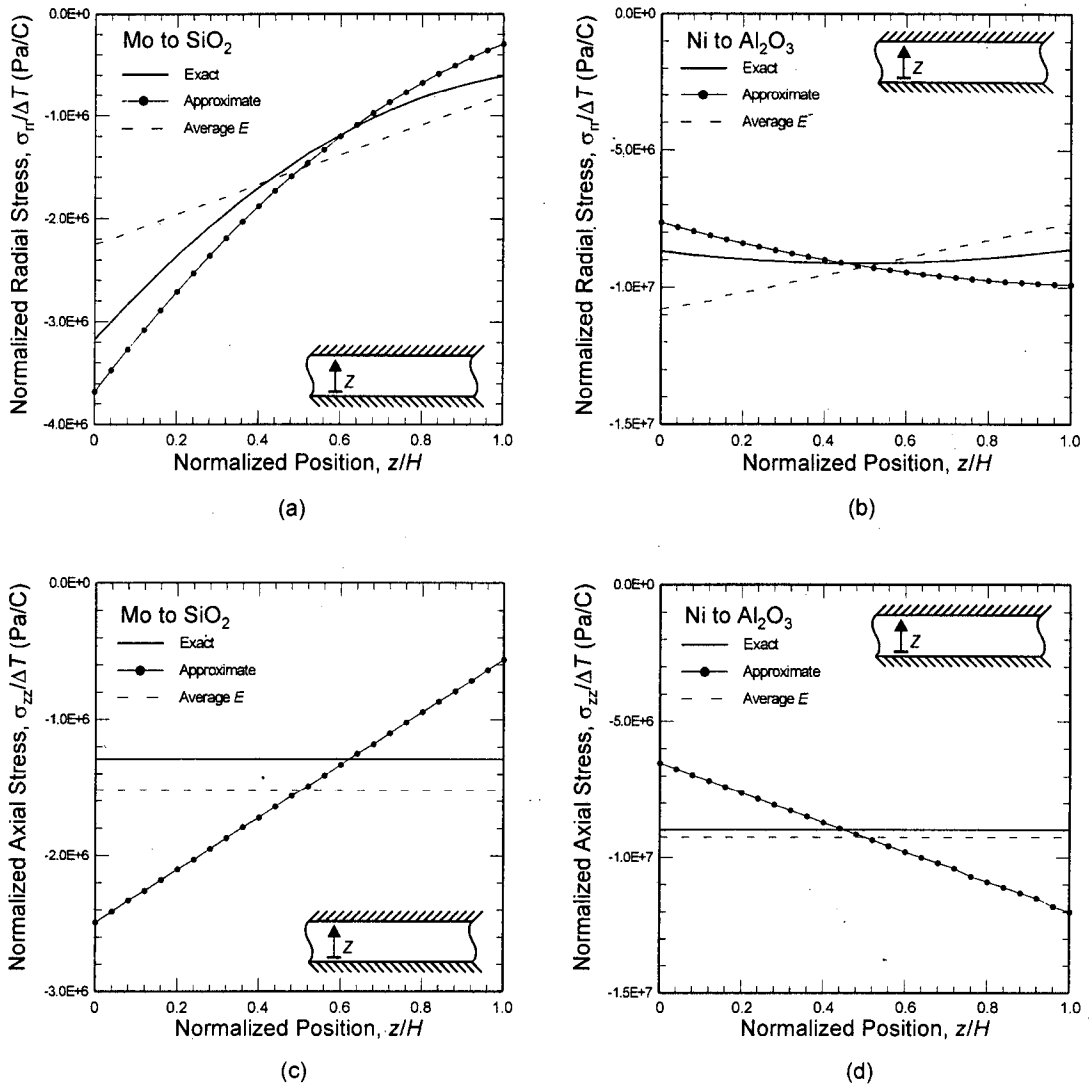

Figure 3.6 FGM film sandwiched between rigid platens undergoing temperature change ΔT. The redistribution of strain as a function of local modulus leads to a solution that is not amenable to this approximate method.

(a)

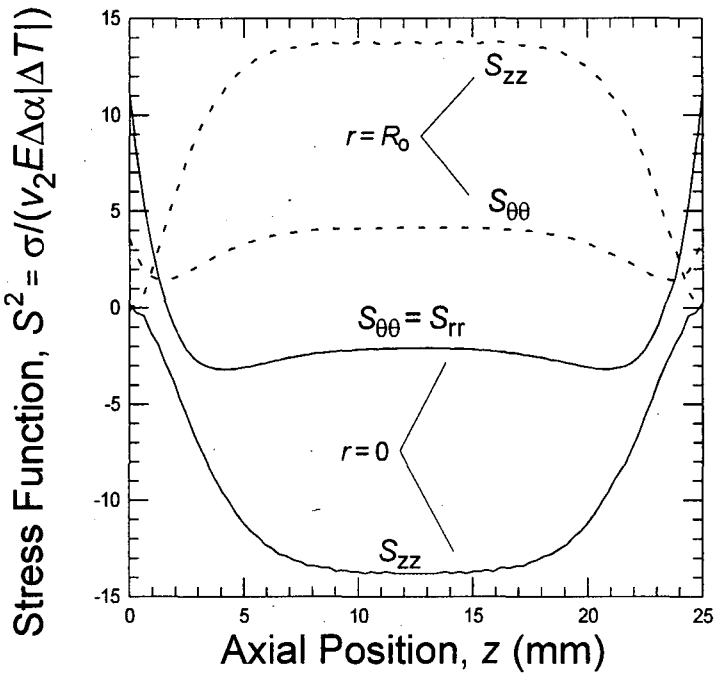

(b)

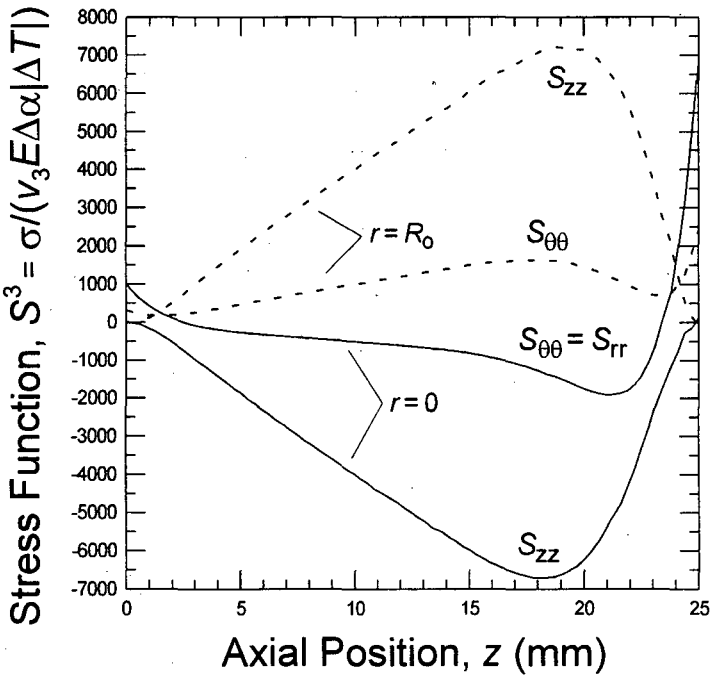

Figure 3.7 (a) Quadratic stress function, S_{ij}^2 , along the centerline ($r = 0$) and surface ($r = R_o$) for stress components $ij = \theta\theta$, zz.
(b) Cubic stress function, S_{ij}^3 , along the centerline ($r = 0$) and surface ($r = R_o$) for stress components $ij = \theta\theta$, zz.

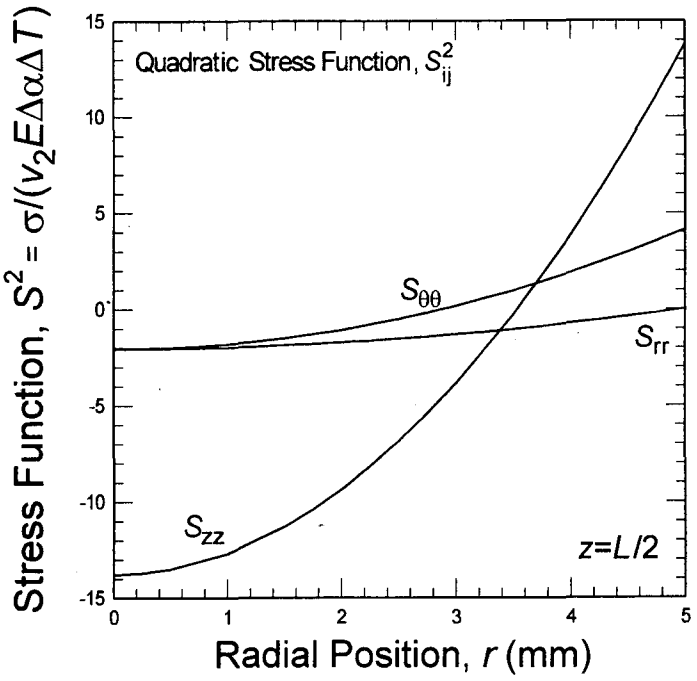

(a)

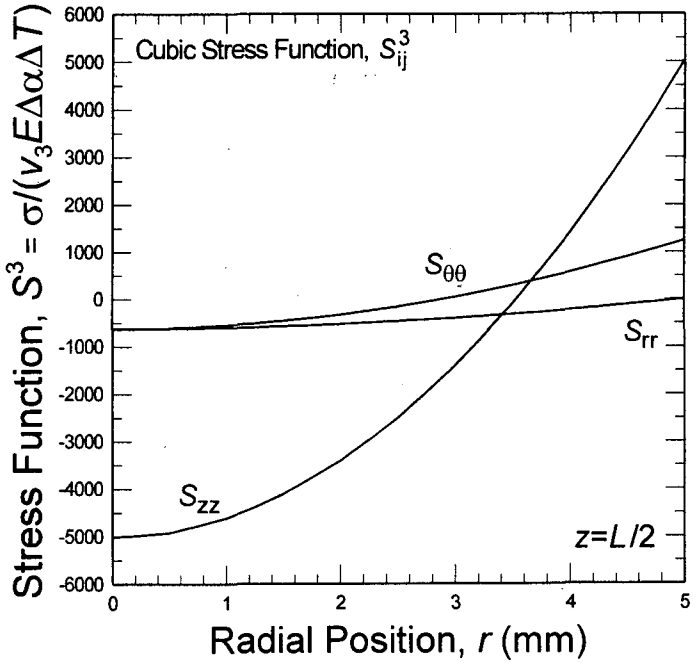

(b)

Figure 3.8 (a) Radial variation of S^2_{ij} and (b) of S^3_{ij} at $z = L/2$.

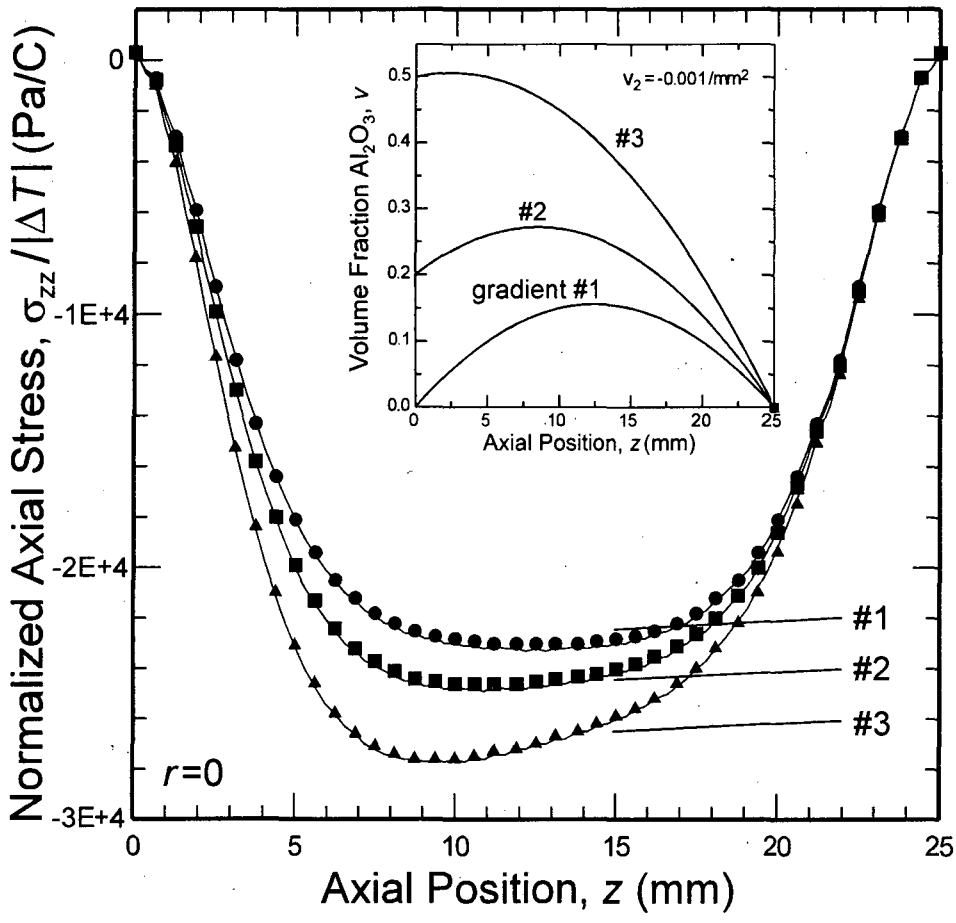

Figure 3.9 The axial residual stress component, σ_{zz}, resulting from the three quadratic gradients (insert), each with the same curvature (v_2 = -0.001 mm^{-2}). The approximation of Eq. 3.12 for each of the gradients (solid lines) closely matches the finite element results (closed symbols).

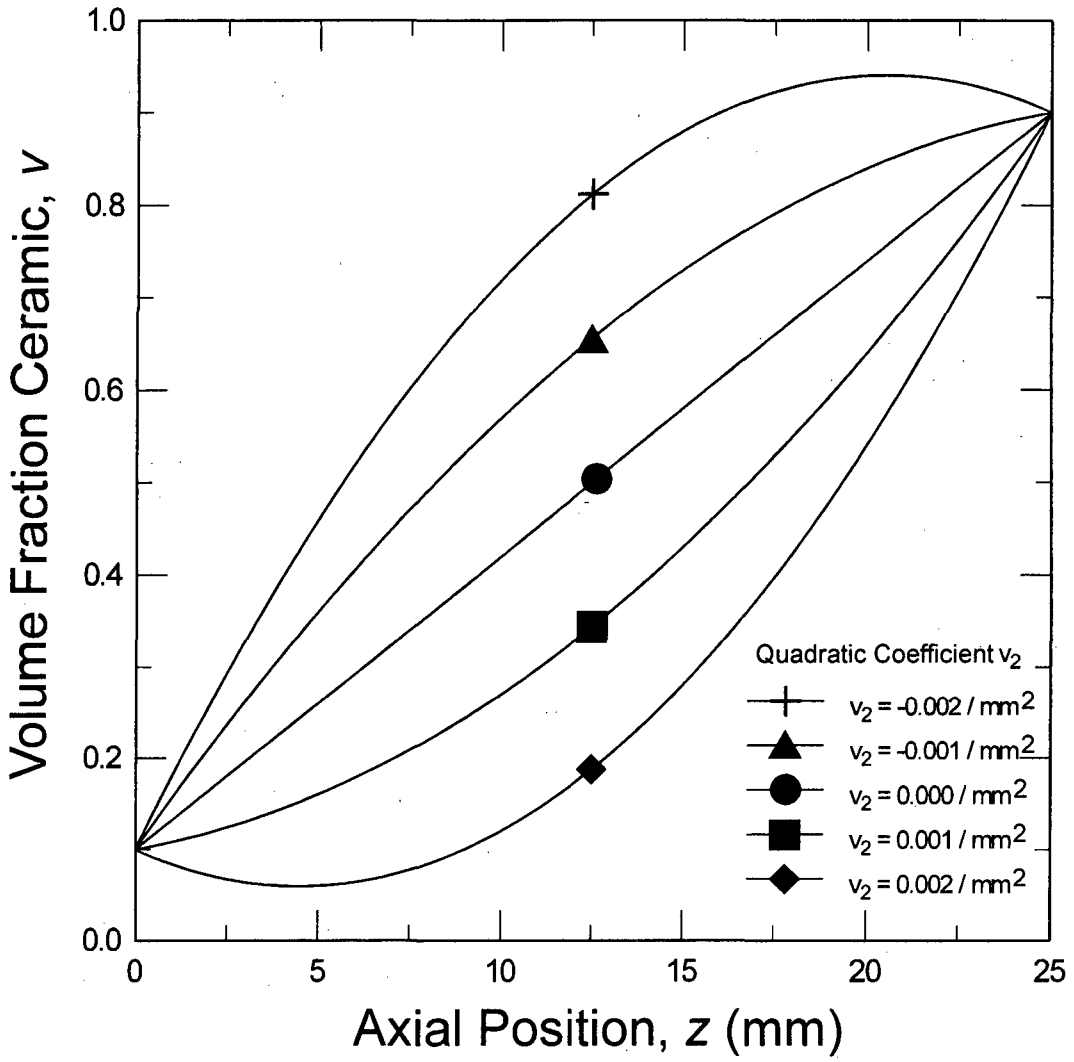

Figure 3.10 A series of gradients with varying curvatures. The symbol on each curve indicates the value of the curvature such that the symbols +, ▲, ●, ■, ♦ correspond respectively to v_2 =-0.002, -0.001, 0.0, 0.001, and 0.002 mm^{-2}.

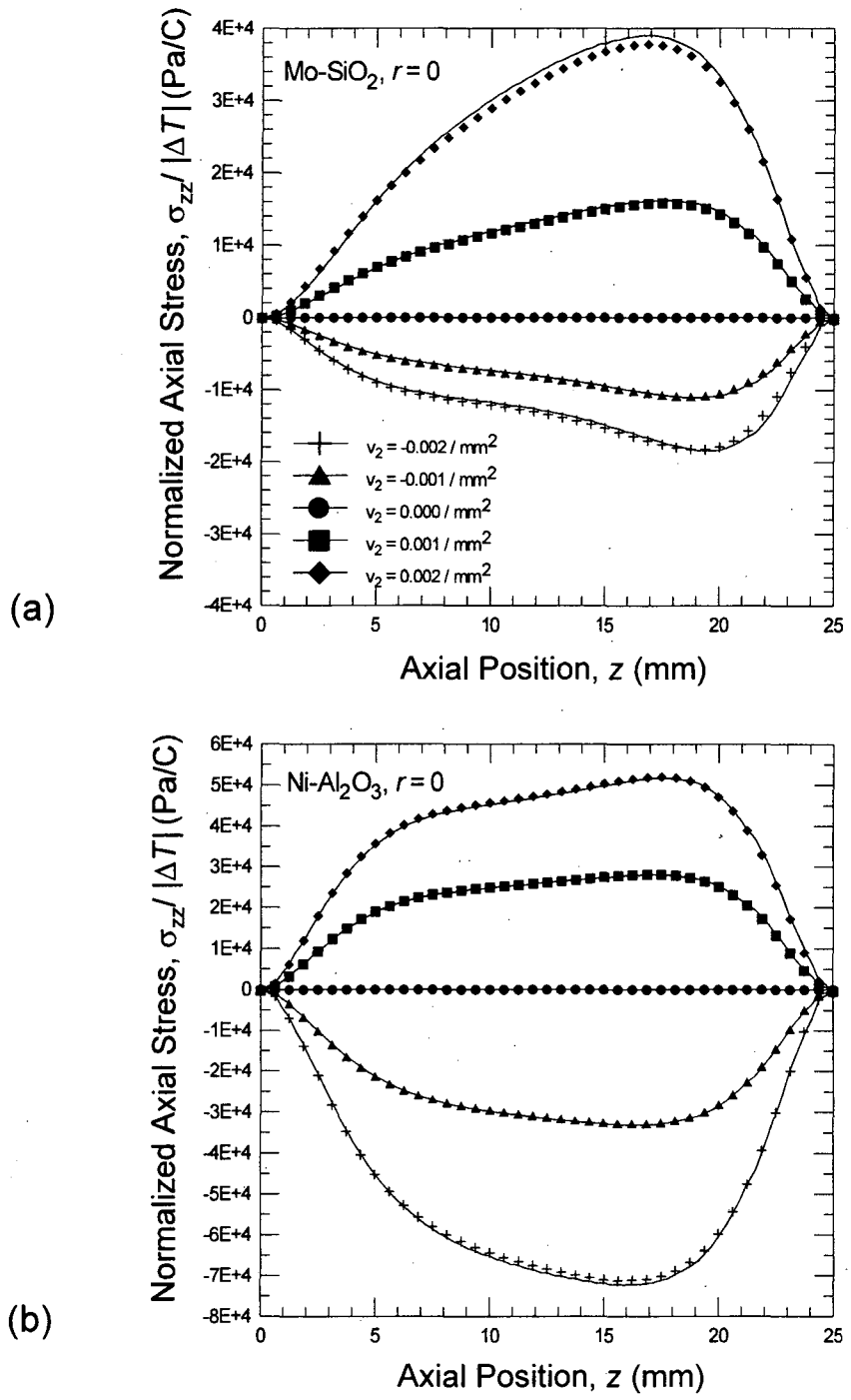

Figure 3.11 Residual stresses along the centerline resulting from the gradients in Fig 3.10 for the (a) Mo-SiO_2 and the (b) Ni-Al_2O_3 system. FGM calculations (symbols) are accurately approximated by Eq. 12 (solid lines).

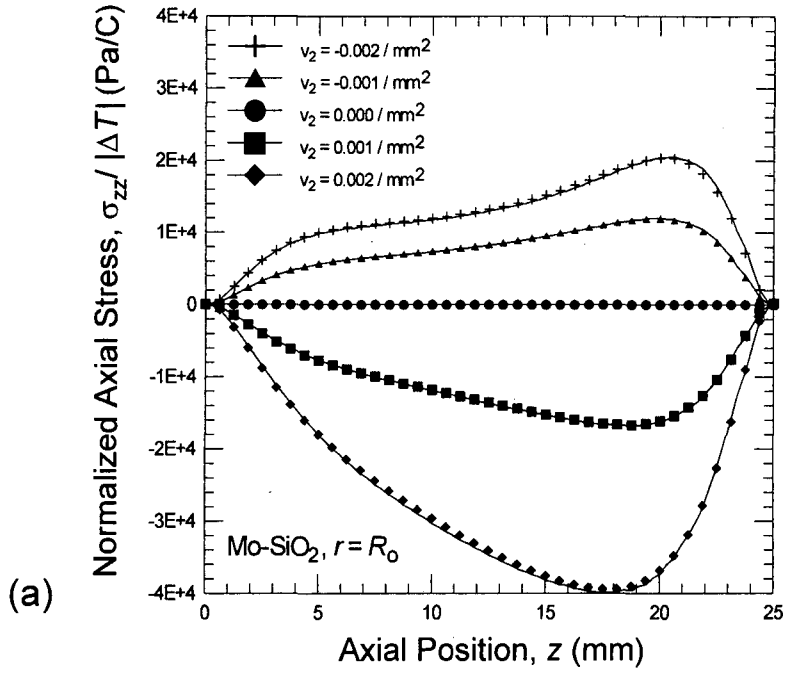

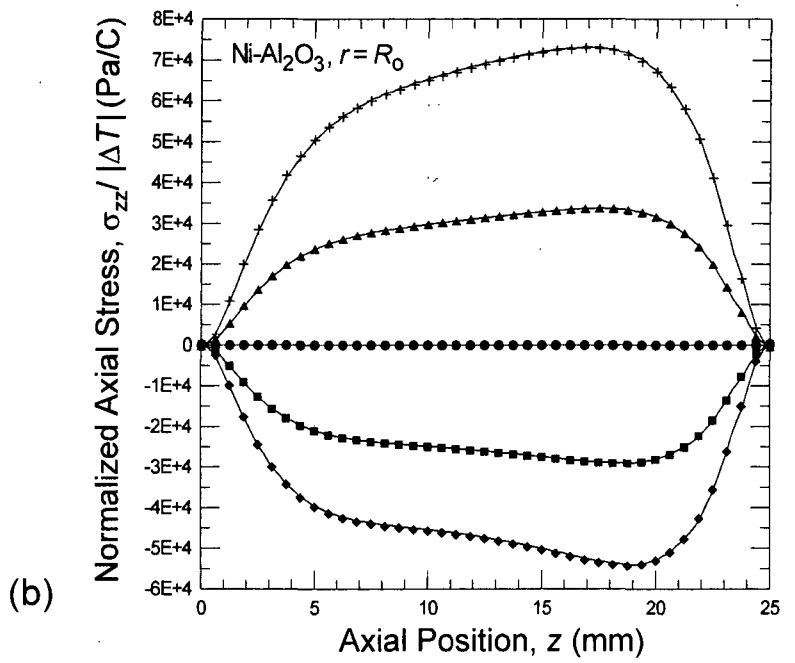

Figure 3.12 Residual stresses along the surface resulting from the gradients in Fig. 3.10 for the (a) Mo-SiO_2 and the (b) Ni-Al_2O_3 system. FGM calculations (symbols) are accurately approximated by Eq. 12 (solid lines).

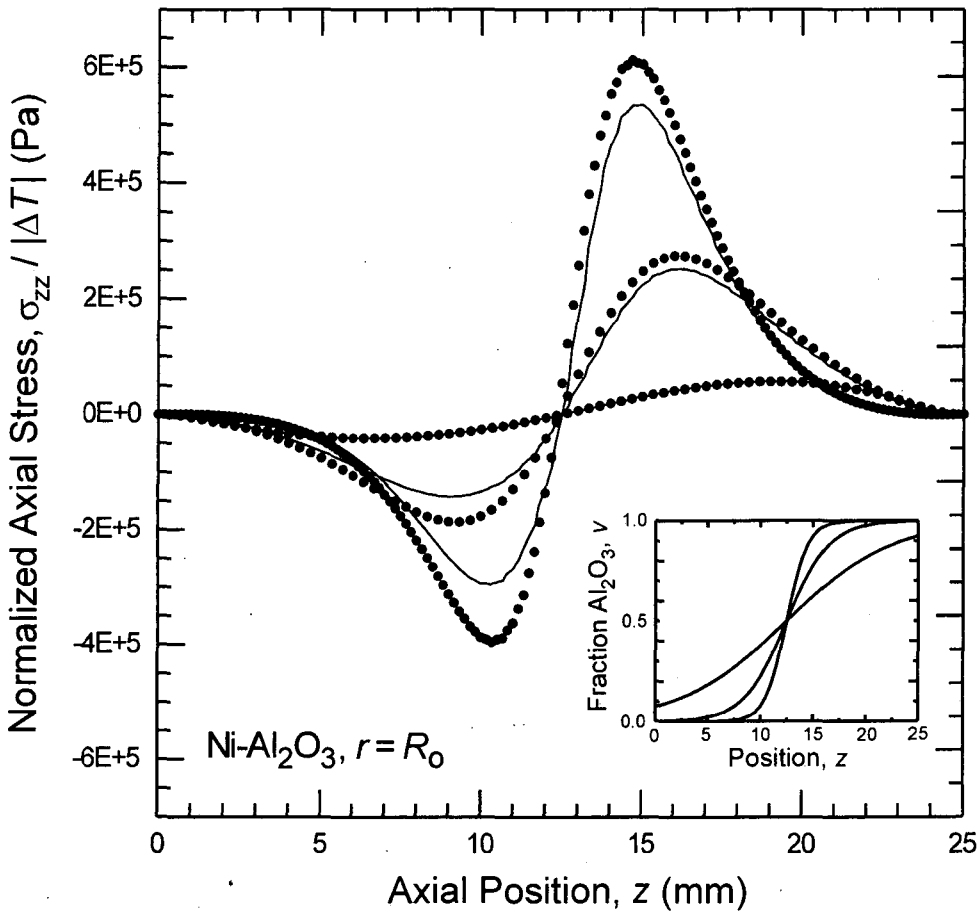

Figure 3.13 The surface residual *zz*-stresses resulting from the series of sigmodial gradients (insert). The finite element results (symbols) are approximated by Eq. 3.12 (lines).

Chapter 4

Statistical Fracture Modeling: Crack Path and Fracture Criteria with Application to Homogeneous and Functionally Graded Materials

NOMENCLATURE LIST

x, y	Cartesian coordinates. Crack lies along $y = 0$ in the x-direction.
r, θ	Polar coordinates
ξ	Dummy coordinate variable
$\sigma_{xx}, \sigma_{xy}, \sigma_{yy}$	Components of stress referenced to {x,y} coordinate system
$\sigma_1, \sigma_{\theta\theta}$	Maximum principal stress, hoop stress
a	Crack length
B	Characteristic thickness
K_I, K_{II}	Mode-I and mode-II stress intensity factors
G	Strain energy release rate
ψ	Phase angle of crack tip, $\psi = \tan^{-1}[K_{II}/K_I]$
f^I, f^{II}	Nondimensional functions of θ for elastic crack stresses
f_1^{ψ}	Nondimensional function of θ and ψ for elastic crack principal stresses
Φ	Global failure probability
K_Φ	Probable fracture toughness. K to achieve failure probability Φ.
$p(\sigma)$	Failure probability in the limit of small volume
p^*	Volume-weighted failure probability
m	Weibull modulus
σ_o , σ_u	Weibull scaling stress, cut-off stress
g	Function that describes property variation with location
b, c	Gradient parameter, value at the crack tip
E, ν	Young's Modulus, Poisson's ratio
$\bar{x}, \bar{y}$	Coordinates of average location of crack initiation site
ϕ	Angle of average crack initiation event, $\tan^{-1}(\bar{y}/\bar{x})$
f	Percentage of fracture initiations occurring between $-\pi$ and θ_f
θ_f	Angle defining the fth-percentile of fracture probability
$\bar{r}$	Average distance of crack initiation
r_x	Distance of maximum local failure probability
ρ	Cutoff radius near crack tip
R	Outer radius of integration for analysis of infinite bodies
F	Nondimensional mixed-mode toughness function
D	Diameter of penny shaped crack
C	Empirical fitting coefficient for the mixed-mode toughness envelope

4.1 Introduction

The earliest report on the relationship between the volume of a brittle material and its measured strength is credited to Leonardo Da Vinci, who observed that the strength of a wire in tension decreased as its length increased (Parsons, 1939). Since then, extreme-value Weibull statistics (Weibull, 1951) have been developed to model the dependence of probabilistic failure on both applied stress and affected volume of a bulk material. This dependence can explain phenomena such as the enhanced measured strength of brittle materials in bending tests versus those in tension. Similarly, the fracture toughness of material that undergoes a stress-controlled fracture initiated away from a crack tip can be predicted by applying Weibull statistical analysis to bodies containing cracks or notches.

One area where Weibull statistics can play a descriptive role is in the fracture of composites. Weibull statistical analysis provides a tool for describing the relationship between the probability of fracture and the distribution of stresses near a crack. Given that these stresses are affected by modulus gradients in FGMs, an FGM with a statistically variable fracture response will fracture at a stress intensity, K, different from that in a homogeneous material. This type of analysis also allows for a description of the crack path. Far-field tensile loading on materials with gradients in modulus can cause mixed-mode (tensile and shear) crack loading. Cracks in materials that grow continuously from the tip are known to kink when loaded in mixed-mode. Through the Weibull analysis, the effects on the crack path of the gradient-induced stresses can be assessed for materials that initiate fracture at locations away from the tip. Effects on toughness and crack trajectory from gradients in strength can also be explored though this framework.

To describe the mixed-mode crack extension of materials governed by Weibull statistics, relationships for the average distance and angle of fracture initiation near an elastic crack tip and probable toughness are developed in this work. These relationships are first applied to infinite, homogeneous bodies and results are compared with classical deterministic behavior for kinking and extension in response to the stresses exactly at the tip. The analysis is then applied to infinite FGMs. Although the analysis depends on failure at locations away from the crack tip, in both these applications, the effects of conventional higher order terms in the stress field, e.g., the *T*-stress, are not considered. Finally to test the dependence on geometry-specific stresses away from the crack tip, two fracture mechanics specimen geometries with various modulus and strength gradients are examined using the finite element method.

4.2 FGM Fracture Mechanics

The study of fracture mechanics for FGMs has generated linear-elastic crack-tip stress field solutions for various elastic gradients and boundary conditions. The fundamental result of fracture mechanics analyses is that for locations asymptotically close to the crack tip, the stress field for a homogeneous material and an FGM are identical (Erdogan, 1985; Jin and Noda, 1994). In this limit, the stresses near the crack tip are described by the classical Williams solution (Williams, 1957):

$$\sigma \approx K_I f^I(\theta)/\sqrt{2\pi r} + K_{II} f^{II}(\theta)/\sqrt{2\pi r} \qquad \text{with}$$

$$f^I(\theta) = \left[\cos\left(\frac{\theta}{2}\right)\left(1-\sqrt{\sin^2\left(\frac{\theta}{2}\right)}\right)\right] \quad \text{and}$$

$$f^{II}(\theta) = \left[-\sin\left(\frac{\theta}{2}\right)+\sqrt{1-\frac{3}{4}\sin^2\left(\frac{\theta}{2}\right)}\right] \tag{4.1}$$

for $\sigma = \sigma_1$, the maximum principal stress. Figure 4.1 compares the isostress contours for principal and hoop stresses for the sharp elastic crack with phase angles of $\psi = 0°$, 45° and 90° ($K_{II} = 0$, $K_I = K_{II}$, $K_I = 0$).

As in homogeneous materials, K_I and K_{II}, the mode-I and mode-II the stress intensity factors characterize the magnitude of the symmetric and antisymmetric stress fields in a neighborhood near the crack tip; however, their values for a given geometry and load will differ versus the homogeneous case in both magnitude, $|K| = \sqrt{K_I^{\,2} + K_{II}^{\,2}}$, and phase angle, $\psi = tan^{-1}(K_{II}/K_I)$ (Konda and Erdogan, 1994).

In an FGM with variable modulus $E(x,y)$, strains associated with the Williams crack-tip field do not satisfy the equations of compatibility. At finite distances away from the crack-tip (at locations with an elastic modulus different from that at the tip), the solution field must take on a different character. Therefore, the steeper the gradient in E, the smaller the region where Eq. 4.1 pertains. Outside of the K-dominant regions, the stresses depend on the variation in E.

The mixed-mode analysis of Konda and Erdogan (1995) satisfactorily describes the stress field near the crack by the pointwise multiplication of the Williams solution by the variation in Young's modulus, chosen as $E(x,y)/E(0,0) = e^{(\beta \cdot x + \gamma \cdot y)}$. Written in a more general form:

$$\sigma_{ij} \approx \frac{E(x,y)}{E(0,0)}\left[\frac{K_I}{\sqrt{2\pi r}} f_{ij}^{I}(\theta) + \frac{K_{II}}{\sqrt{2\pi r}} f_{ij}^{II}(\theta)\right], \tag{4.2}$$

for any $E(x,y)$ which is a continuous function of position (taking the Poisson's ratio, ν, as a constant). $E(0,0)$ is the value at the crack tip.

Eq. 4.2 approximates the effect of modulus variation, $E(x,y)$, on the stress. For locations asymptotically close to the tip, Eq. 4.2 and Eq. 4.1 agree. Moreover, Eq. 4.2 satisfies the equations of compatibility exactly, although it is not an exact solution, as it does not satisfy the conditions for equilibrium. It will therefore also be limited in its own region of dominance.

The issue of the direction of crack growth in homogeneous materials was first addressed by Erdogan and Sih (1963), who predicted that a crack loaded in mixed-mode would kink along an angle, θ, which corresponds to the maximum hoop stress, $\sigma_{\theta\theta}$, at the crack tip. Later analyses that explored the mode-mixity and strain energy release rate, G, of a kinked crack and gave more rigorous results. The analysis of crack kinking in FGMs has been limited to the application (Gu and Asaro, 1996) of the first-order homogeneous analysis of Cotterell and Rice (1980). Implicit in this analysis is the assumption that the gradient in Young's modulus only affects the crack tip through mode-mixity, ψ. This is true for crack kinks of infinitesimal length growing continuously from the crack tip, but these assumptions cannot be sustained if material inhomogeneity leads to longer kinks or for fracture events that are initiated ahead of the crack tip or in materials with variable strength.

4.3 RKR Fracture Modeling

4.3.1 Weibull statistics

The effects of variability in strength of brittle materials were analyzed by Weibull (1951) and described in terms of extreme value statistics. For a body experiencing stress σ, the probability of failure Φ, is

$$\Phi = 1 - \exp\left[\int_{Vol} -\frac{p(\sigma)}{V_o} dV\right], \tag{4.3}$$

where V_0 is a reference volume and $p(\sigma)$ is the strength distribution, *i.e.*, the cumulative failure probability of the material in the small-volume limit. The three-parameter Weibull strength distribution has the form:

$$p(\sigma) = \begin{cases} \left(\dfrac{\sigma_1 - \sigma_u}{\sigma_o}\right)^m & \text{for } \sigma - \sigma_u > 0 \\ 0 & \text{for } \sigma - \sigma_u \le 0 \end{cases} \tag{4.4}$$

where σ_1 is maximum principal stress and σ_u, σ_0 and m are material constants to be determined by experiment. The lower bound cutoff strength, σ_u, is often set to zero for ceramics and glasses, thus defining the two-parameter Weibull distribution. σ_0 is the scaling strength such that in pure tension when $\sigma_1 = \sigma_0$, and $V = V_0$, $\Phi = 1 - e \sim 0.62$.

The Weibull function expresses the probability of failure in terms of both the level of stress and the volume over which the stress is distributed. The relative severity of this volume dependence is in large part determined by the Weibull modulus, m.[1] In the limit of a purely deterministic material, as $m \rightarrow \infty$, failure would be determined by the maximum stress at one point. For a high-quality engineering ceramic, m is in the range of 20-50. However, for brittle/brittle composites, the introduction of internal interfaces, residual stresses, and increased microstructural variability often result in greater scatter in strength and a lower Weibull modulus. Indeed, bend strength tests of a SiO_2/Mo FGM have indicated a Weibull modulus of 4 pertains (Tomsia *et al.*, 1997).

[1]The cutoff stress σ_u also can mitigate the effect of volume. When a two-parameter distribution is applied to an infinite body, any non-zero far-field stress leads to a failure probability of unity. The invocation of a cutoff stress allows for the modeling of failure in an infinite body.

To demonstrate fracture initiation behavior near a crack in a homogeneous material with strength described by Weibull statistics based on the maximum principal stress, Fig. 4.2 displays the results of Monte Carlo simulations. (Details are given in Appendix A.) Each point indicates the location of a fracture initiation for mode-I (square symbols) and mixed-mode, $\psi = 45°$, (circles) loading. A number of features are evident. First, for the mode-I case, these data are scattered away from the x-axis, but are roughly symmetric about $y = 0$, giving a bimodal distribution with an average angle of 4°. For the mixed-mode case, the data are strongly skewed toward the negative y-direction, at an average angle of –81°. This indicates that, averaging of a number of events, there is the tendency for straight-ahead crack extension under mode-I loading and downward growth under positive phase-angle mixed-mode loading. In addition, for the same number of trials, the number of fracture initiations under mixed-mode loading is greater than for mode-I loading at the same $|K|$ (764 sites vs. 111). This indicates a lower resistance to fracture initiation pertains at a given magnitude of the stress intensity. This would result in a lower measured fracture toughness. This simulation indicates the trends that would be expected; a framework for quantification for such results is needed.

4.3.2 Statistical fracture modeling

Originally the scatter in fracture toughness data motivated the application of Weibull statistics to crack problems. The near-tip region of a crack is an extreme example of the competition between stress and volume. At the tip of a sharp elastic crack, stress is infinite; however, such stress is experienced over exactly zero volume. Away from the crack tip, stresses decrease; however, an increasing volume is exposed to stress. The Ritchie-Knott-Rice (RKR) fracture model (1973) in part used this

competition to motivate the description of fracture in low-toughness steels in terms of the stresses a "characteristic distance" ahead from the tip of the crack, where fracture of a brittle inclusion triggers catastrophic crack growth.

The direct substitution of singular fracture mechanics stress fields into Eq. 4.3 is problematic, as it yields an integral that is not finite for most values of the Weibull modulus.[2] This means that for any applied load, the global failure probability would be unity and the fracture toughness would be zero. A number different arguments have been invoked by investigators have to avoid this non-physical result.

For brittle materials, the explicit modeling of a notch rather than a sharp crack tip allows for the integration of the stress field over the entire material region, with the results being a function of the size of the notch (Lei *et al.*, 1997; Becker, 1999). For materials with sufficient ductility, crack tip blunting truncates the stresses near the tip and renders the integral (Eq. 4.3) finite. Numerical calculation (Lei *et al.*, 1997) of the blunted stress field has been performed as well as the pseudo-analytic application (Lin *et al.*, 1986b) of a simplified plastic notch field within the HRR singularity (Hutchinson, 1968; Rice and Rosengren, 1968).

For elastic sharp cracks, special attention must be paid to the physical implications of applying Eq. 4.3 near the crack tip. Most early work on statistical fracture was strongly rooted in the dominant fracture mechanism of the material being studied (e.g. carbide fracture in low-toughness steels). Regardless of the mechanism

[2] For the linear elastic solution, the integral is not defined for ($m > 4$). In nonlinear materials, there is a similar result which depends on m and the strain-hardening coefficient (Lin *et al.*, 1986a).

underlying the statistical fracture process, the characterizing statistical parameters of the strength distribution will be determined by the volume of material tested to obtain them.

When a volume of material is smaller than can be expected to possess any of the dominant fracture elements (carbide, grain boundary, etc), the subsequent failure will no longer be characterized by the same parameters as is the bulk material even if it is statistical in nature. Such small volumes are likely to be stronger than implied and thus may contribute little incremental probability of failure. The implications of applying the Weibull distribution to the region of small volume and high stress gradient near the crack tip led Beremin (1983) to invoke a cutoff radius around the crack tip, which was excluded from the region of integration. Evans (1983) ruled out the classical Weibull equation for $p(\sigma)$ on these and related physical grounds. This allowed for the analysis of a sharp crack tip with a substitute $p(\sigma)$.

4.3.3 Crack Trajectory

Previous authors (Evans, 1983; Lin *et al.*, 1986a,b) have investigated the incremental failure probability ahead of a crack tip. The distance at which the incremental failure probability was a maximum was deemed to be a characterizing parameter. These analyses were performed on an infinite body and utilized the first term of the elastic stress field expansion (either Williams or HRR).

Mixed-mode fracture does not lend itself to the analysis of Lin *et al.* (1986a). Considering the single distance of the maximum failure probability is of insufficient utility compared to analyzing the full planar stress field. Although previous analyses of continuous crack kinking used the hoop stress $\sigma_{\theta\theta}$ as the criteria for determining the kink

angle and critical load, for initiation in material at a distance away from the crack tip, the orientation of flaws need not be along lines of constant-θ. Therefore the principal stress σ_1 is used to determine flaw activation. The symmetric Mode-I elastic stress field possesses maxima in principal stress σ_1 at $\theta = \pm 60°$; symmetry dictates that Mode-I crack advance must occur along $\theta = 0°$, but only statistically.

To describe the expected location of these activated flaws, a spatial average of the failure probability is invoked. For a body with spatially varying stress, the average, or expected value, of a coordinate ξ is obtained via a weighted integration:

$$\bar{\xi} \equiv \frac{\int_{Vol} \xi \frac{p(\sigma)}{V_o} dV}{\int_{Vol} \frac{p(\sigma)}{V_o} dV}. \tag{4.5}$$

When $\xi = x$, $\xi = y$ the mean Cartesian coordinates, $\bar{x}$ and $\bar{y}$, of fracture initiation are obtained. From these, the angle from $y = 0$ plane of the average location, can be determined as $\phi \equiv \tan^{-1}(\bar{y}/\bar{x})$. Eq. 4.5 yields the mean distance $\bar{r}$ for $\xi = r$. (This is, in general, distinct from the radial coordinate of the average location, $\sqrt{\bar{x}^2 + \bar{y}^2}$, which will be, for the problems examined, less than $\bar{r}$.)

It is possible to describe the relative contribution of stress fields at different angles to the total failure probability. The median angle which bisects the distribution of failure probability, θ_{50}, is defined through

$$\frac{\int_{-\pi}^{\theta_f} p(\sigma)d\theta}{\int_{-\pi}^{\pi} p(\sigma)d\theta} = f\,\Phi \tag{4.6}$$

with f = 50%. Furthermore, bands of probability can similarly be defined, so that the proportion of the failure probability between two angles are determined, i.e., 90% of failures will be initiated between θ_5 and θ_{95} .

4.4 Procedures

Calculations for infinite bodies were performed with stresses derived from Eq. 4.2. Eqs. 4.5 and 4.6 were evaluated with the numerical integration package in Mathematica 3.0 (Wolfram Research, Champaign, IL, USA). For finite geometries, the single edge-crack tension (SE(T)) and middle-crack tension (M(T)) fracture mechanics specimens were modeled by a plane-strain linear-elastic finite element code for FGMs, FEAP 4.2 (Zienkiewicz and Taylor, 1989).

The crack length, a, was kept constant in the analyses, being equal to half the total width of the sample in the x-direction, W. The mesh for the M(T) sample was the same as for the SE(T), (Fig. 4.3) except it contained an additional row of displacement boundary conditions along $x = -a$, preventing displacements in the x-direction. The mesh consists of 2300 total elements, 9233 nodes, with extensive refinement in the near-tip region, with the smallest element size on the order of $a/10^6$. The fracture mechanics element of Stern and Becker (1989) was used in both meshes to model the first row of elements surrounding the crack tip. A second mesh with 4096 elements was also used to

estimate the error via refinement. The difference between the results from the two meshes was negligible, with average initiation angles differing by less than 0.1°.

Stress intensity factor calibrations were performed for each geometry and gradient. Pointwise evaluation of the stress intensity factors can be obtained through:

$$\begin{Bmatrix} K_I \\ K_{II} \end{Bmatrix} = \sqrt{2\pi r} \begin{pmatrix} f_{xy}^{I}(\theta) & f_{xy}^{II}(\theta) \\ f_{yy}^{I}(\theta) & f_{yy}^{II}(\theta) \end{pmatrix}^{-1} \begin{Bmatrix} \sigma_{xy}(r,\theta) \\ \sigma_{yy}(r,\theta) \end{Bmatrix}. \tag{4.7}$$

Excluding the crack flanks and the first four elements at the crack tip, these values were averaged over Gauss points within the next five rows of elements (360 elements total, those for $-160° < \theta < 160°$ and $1/10^5 < r/a < 1/10^4$). High-precision results were obtained and found to vary weakly with variance of this fitting region.

The modeling of the fracture mechanics samples used the results from each finite element calculation in the probability integral as the sum over the finite elements, viz.

$$\int_{vol} \xi \left(\frac{\sigma}{\sigma_o} \right)^m \frac{dV}{V_o} \approx \frac{B}{\sigma_o{}^m V_o} \sum_j^{elems} \xi_i \left[\sum_i^{Gauss\,pts} \left(\sigma_I^m \right)_i J w_i \right]_j \tag{4.8}$$

where J is the Jacobian of the mapped element (calculated at the Gauss points), w_i's are the weights for Gauss-Legendre quadrature, and B is an out-of-plane thickness. For a physical sample with a large thickness, multiple fracture events are sometimes expected to occur along the crack front, with implications discussed in Section 4.5.1.5.

Sigmoidal variation in modulus or strength was employed via a gradient function $g(x)$ or $g(y)$:

$$g\begin{pmatrix} x \\ y \end{pmatrix} = (c-1)\tanh\left(b\begin{pmatrix} x \\ y \end{pmatrix} \right) + c\ . \tag{4.9}$$

At the origin (the crack tip), $g(0) = c$. The slope of the function, $b(c\text{-}1)$, is controlled by b for fixed crack-tip value, c. A value of $c = 10.5$ was chosen for the analyses, allowing for a twenty-fold change in properties across the sample. As such, b is a measure of the steepness of the gradient and $\frac{\nabla g}{g(0)} = \frac{b(c-1)}{c} \approx b$. In the limit of $b \rightarrow \infty$, a sharp interface is formed, with $g(\infty)/g(-\infty) = 2c - 1$. Fig. 4.4 displays the shapes of the gradient for a range of b.

4.5 Results and Discussion

4.5.1 Homogeneous body analyses

The application of the Weibull crack initiation model to the geometry with a mode-I crack permits the determination of fracture toughness from statistical parameters (σ_u, σ_o and m) and perhaps other material parameters (flaw density, strain-hardening coefficient). The extension of the Weibull analysis to mixed-mode situations allows for predictions about homogeneous material response without reference to geometry effects.

4.5.1.1 Mixed-mode fracture toughness

Combining Eqs. 4.1, 4.3 and 4.4 and inverting gives an expression for the stress intensity to produce a given failure probability, K_Φ

$$K_\Phi = \frac{\sigma_o (V_o / B)^{1/m} \sqrt{2\pi} (-\ln(1-\Phi))^{1/m}}{\left[\int_{-\pi}^{\pi} f_1(\theta,\psi)^m \, d\theta \right]^{1/m} F(m,R,\rho)} \qquad (4.10\text{ a})$$

$$F = \begin{cases} \left[\dfrac{R^{2-\frac{m}{2}} - \rho^{2-\frac{m}{2}}}{2-\frac{m}{2}} \right]^{\frac{1}{m}} & \text{for } m \neq 4 \\ \left(\ln\left(\dfrac{R}{\rho}\right) \right)^{\frac{1}{4}} & \text{for } m = 4 \end{cases} \qquad (4.10\text{ b})$$

where $f_1(\theta,\psi) = \sigma_1\sqrt{2\pi r}/|K|$ and can be inferred from Eq. 4.1. The integration is conducted over an annulus between the inner cutoff radius, ρ, and the outer radius, $R \gg \rho$, which is still within the K-field (Eq. 4.1). Explicit values of K_Φ scale primarily with $\sigma_o(V_o/B)^{1/m}\rho^{(m-4)/2m}$ for large m and $\sigma_o(V_o/B)^{1/m}/R^{(4-m)/2m}$ for small m. That is, for materials with large scatter in strength, toughness is dictated by the large volume of low-stress material as $r \to R$ and for those with little scatter, toughness is determined by the small volume of highly stressed material near the crack tip.

From these, geometry-independent predictions of the relative fracture toughness for mixed-mode loading can be made (Fig. 4.5a). These toughnesses are normalized to the mode-I toughness (therefore are independent of the choice of Φ) and predict (for a stress-controlled failure mechanism) a reduction in the fracture toughness under mixed mode loading. Comparing the isostress contours for $\psi = 0°$ and 45° in Fig. 4.1 provides an explanation of this behavior. The area contained within the 45° contour is plainly larger than that of the 0° contour. This can be interpreted as a larger volume being exposed to a given level of stress at a given G, or an elevation of stress at a fixed distance, r, from the crack tip. For a material described by initiation at a distance, this results in a lessening of the fracture toughness.

This reduction in toughness under mixed-mode conditions at a moderate phase angle is stronger than that for a deterministic analysis based on the maximum hoop stress $\sigma_{\theta\theta}$ (Erdogan and Shih, 1957) (dashed line in Figure 5.4a) or the maximum energy release rate criteria applied to the tip of a kink. The mixed mode fracture envelope is displayed in Fig. 4.5b. An alternative theory of Palaniswamiy and Knuass (1978) predicts a failure envelope defined by $K_I/K_{Ic} + (1/C \cdot K_{II}/K_{Ic})^2 = 1$, where C is an experimental fit parameter. A value of $C = 0.82$ closely fits the maximum energy release rate criteria for a kink, where $C = 0.87$ more closely fits the maximum hoop-stress law (Singh and Shetty, 1989). The continuous kink analysis is consistent with experimental data for the mixed-mode fracture of Al_2O_3 (O'Dowd *et al.*, 1992).

4.5.1.2 Mixed-mode initiation angle

Under mixed-mode conditions, a crack will not, in general, grow in a self-similar manner, rather it will kink off of the $y = 0$ plane. The average initiation angle ϕ is calculated via Eq. 4.5 as $\tan^{-1}(\bar{y}/\bar{x})$ under mixed-mode conditions for a crack in an infinite homogeneous body (Fig. 4.6). For comparison, the results of deterministic finite angle kink analyses are included (dot-dashed lines). The predicted average crack angles of the statistical formulations based on principal stresses are much larger than those developed by analyzing the continuous growth of the crack tip along the path of maximum hoop stress (Erdogan and Sih, 1963) or maximum strain energy release rate (after He and Hutchinson, 1989). At higher m, these average crack angles increasingly reflect the trend, also plotted, for the angle of maximum principal stress. However, the

behavior would only replicate this for very large m. Median angles, θ_{50}, above which half of the fracture initiations occur, exhibit similar trends (Fig. 4.7) as does ϕ.

This behavior is also easily related to the mixed-mode stress fields plotted in Fig. 4.1. In the case of pure mode-II loading ($\psi = 90°$), the angle of maximum principal stress is along $\theta = 180°$. Therefore, locations of average fracture will tend toward this extreme angle. The boundary conditions dictate that this must be the σ_{xx} component of stress. Deterministic, continuous-growth analyses are restricted to the $\sigma_{\theta\theta}$ component, which is zero at the crack flank, and predict opening along radial lines. This difference requires careful physical interpretation, which will be discussed in Section 4.5.1.5.

4.5.1.3 Contours of failure probability

In addition to measuring the angle of the average fracture event, it is important to consider the distribution of first fracture probabilities. Fig. 4.7 displays the θ_f for f = {5,25,50,75,95} and m = {3,11}. The trends for θ_{50} (the median angle for fractures) are very similar to those for ϕ, described in the previous Section.

The 90% and 50% bands of probability are also indicated. Within these bands 50% and 90% of failures, respectively, will be initiated. For mode-I loading, there is little effect of Weibull modulus. The 50% band spans 120° symmetrically about 0°. There is a much greater effect for the pure mode-II case, spanning 73° for m = 3 and 21° for m = 11. This difference is due to the bimodal, (symmetrical about $\theta = 0$) stress field in the mode-I case and the highly skewed, but uni-modal stress field with a maximum at $\theta = -\pi$ for the mode-II case. In the limit as $m \rightarrow \infty$ for the mode-II case, the band will

infinitely narrow near $\theta = -\pi$. The band of failures in the mode-I case will be clustered at $\theta = \pm 60°$.

4.5.1.4 Mean fracture initiation distance

The mean distances of fracture initiation $\bar{r}$ for an infinite body for a range of Weibull modulus, m, are displayed in Fig. 4.8. Two inner limits of integration in the r-direction were used for Eq. 4.3, with root radii of $\rho = R/10^3$ and $\rho = R/10^5$. For small values of m (m = 2-4), $\bar{r}$ is on the order of the outer limit of integration R, $\bar{r} \sim R/2$ to $R/10$. For larger values of m ($m > 7$), $\bar{r}$ is on the order of the inner cutoff limit of integration ρ, $\bar{r} \sim \rho$ to 3ρ. Results are independent of mode-mixity.

For small m, the volume is a determinant and for $m = 2$, the failure probability in a thin annulus at a given r is uniform from the crack tip to infinity. Therefore, the mean distance is the average of the limits of integration $(R + \rho)/2 \approx R/2$. Taking the limit of large m, fracture is dictated simply by the largest stress, that at $\{r,\theta\} = \{\rho, \pm 60°\}$. The results of Fig. 4.8 are asymptotic to that limit, but even for $m > 11$, $\bar{r}$ is measurably larger than ρ. Thus, the first principal stress σ_1, not the hoop stress, is still the pertinent measure of stress for the failure criteria, as $\sigma_1 \geq \sigma_{\theta\theta}$, and flaws are expected to be oriented randomly, not along θ.

4.5.1.5 Physical Implications

The present material model is formally limited to calculating the behavior of the first activated flaw, but this "first failure" may or may not lead to catastrophic crack growth. For flaw-intolerant materials such as glasses and fine-grained ceramics, initial

flaw growth and catastrophic failure generally are synonymous. However, there is experimental experience with brittle, polycrystalline or composite materials with low Weibull modulus that near-tip microcracked regions develop (Rühle *et al.*, 1986, 1987) or especially that cracks bifurcate extensively (Wu *et al.*, 1978; Mecholsky, *et al.*, 1976). Evidently, there are flaws that are activated by the near-tip stress field, but do not yet possess the driving force necessary to overcome the next-higher length scale fracture resistance (e.g., after cracking across a weak or residually stressed grain boundary). The statistical initiation analysis (Fig. 4.7) shows that this flaw is unlikely to be located on the path followed by a crack under the same loading conditions but that is continuously moving according to the maximum-$\sigma_{\theta\theta}$ condition. Even in the mode-I case where the statistical and continuous-growth analyses agree on the average angle, most of the microcracks will be initiated at large angles to the crack plane.

When failure ensues from growth of a flaw ahead of the main crack, then further extension will eventually involve connection of this flaw and the main crack. It may be expected that the intervening ligament between the main crack and the microcrack will be fractured or torn under mixed-mode loading requiring much greater dissipation (McClintock, 1997). Moreover, if various flaws along the crack front are triggered prior to criticality, which is more likely with larger B and smaller m, they will each likely be at different angles to the crack plane. Thus the main crack and the microcracks may not immediately link, but rather a microcrack next grows forward, then the uncracked ligaments will act as bridges and further enhance the fracture toughness (Mai and Lawn, 1986). By such interactions, microcracking can be a toughening mechanism in ceramics (Evans, 1989) or more likely serve as a trigger to more potent bridging mechanisms

(Becher, 1991; Rödel, 1992). The resulting bifurcated cracks, rougher crack surface and associated tearing of the trailing ligaments will all lead to significant toughening of the material. Analogous local roughness has also been seen in simulations at the atomic scale of glass fracture (Garofalini, 1999; Blonski and Garofalini, 1997) and may account for the toughness of glass exceeding the thermodynamic Griffith value by a factor of about three (Gumbsch and Cannon, 2000).

The calculated average initiation angle ϕ and more importantly the dispersion in angles, Fig. 4.7, will be descriptive of these microcracks and their potential for toughening, but not necessarily the path of crack advance past the point of criticality nor the actual extent of microcracking prior to criticality. The complicated problem of treating subsequent failure after first fracture requires an entirely different statistical formulation and detailed simulation of a non-continuum microstructure (McClinktock and Zaveral, 1978), which is beyond the scope of the present work. However, the dispersion in angles, which is largest for $\psi = 0$, and the difference in angles for first cracking versus for stable extension (Fig. 4.6) which is larger for $\psi > 0$ and large m, may be indicatory of the potential for toughening involving rising R-curves.

Thus, very low-m materials may be relatively notch-insensitive, with large volumes of low-stress material dominating the probability analysis. For finite geometries, failure would be influenced by stresses outside the K-field, so trends illustrated here are semi-quantitative and their application would be geometry dependent. This effect can be somewhat mitigated by the invocation of a cutoff stress σ_u in the Weibull strength distribution (Eq. 4.4). Indeed the size of flaws implied by the absence of a cutoff stress becomes unrealistic. This would offset some of the pathological

behavior when analyzing cracks in infinite bodies (Eq. 4.10) and may lead to instances where the important behavior occurs within the K-field and reflects trends predicted here, that is the pertinent cutoff radius should vary as $R \propto 1/\sigma_u^{\ m}$.

For sufficiently large m, the bulk material response is much less volume-sensitive and as the scatter in strength decreases, one would expect the material to behave in a deterministic manner. Nonetheless, the transition of the fracture mechanism from dictation by σ_I to $\sigma_{\theta\theta}$ does not follow simply by taking the limit of large m for the present formalism. The behavior of this limiting analysis may be implausible regarding the strength characteristics implied for small volumes under high stress, e.g., near the crack tip. Elementary calculations show that the typical Weibull volume-dependence on strength underestimates the strength of pristine glass fibers, for instance. Similarly for structural ceramics, the strength implied for small volumes using the normal Weibull parameters underestimates the theoretical strength. Therefore, careful consideration must be paid before attempting to apply a statistical model to very near-tip mechanisms.

In particular, the relevance of behavior that implies failure near an arbitrary cutoff radius may be of concern. Clearly, however, for semi-brittle materials wherein crack tip blunting leads to diminished stresses in a region within $r \sim 2 \cdot K^2/(\sigma_{yield}\, E)$ (Rice and Johnson, 1970), the present type of approximation (perhaps using an HRR stress field) may be robust. For more brittle composites, the pertinence may be appreciated by considering a penny-shaped flaw of diameter D centered a distance D ahead of a cutoff radius ρ. The nominal K at the tip of the flaw is related to the applied load K^{∞} as,

$K^{flaw} = \frac{K^{\infty}}{\pi}\left(\frac{D}{2(\rho + D)}\right)^{\frac{1}{2}}$.[3] For $D/\rho = 1.1$, $K^{flaw}/K^{\infty} \sim 1/20$. Recent atomistic simulations have shown that the theoretical strength of impure ceramic/metal interfaces (5-10 GPa) (Hong *et al.*, 1995) can be an order of magnitude below that of flaw-free ceramics ($\geq E/10$). Thus, in composites, impure interfaces experiencing some further mismatch stresses, which can easily exceed ±1 GPa locally, could well fail in preference to the tip of the main crack. Then it may be possible to conceive ρ as being related to the volume within which Eq. (4.3) fails.

4.5.2 FGM infinite body analyses

In the prior Section, discussion was limited to all cracking initiating within the classical *K*-field for homogeneous materials. For cracks in functionally graded materials, the stress and/or strength field at a distance away from the crack will vary with the severity of the gradient. The fracture of an FGM can therefore be modeled, with the parameters describing the gradient included in the analysis, but only addressing failure probabilities within the context of adjustments to a region lying within a homogeneous *K*-field.

The exact size of the domain of integration in Eq. 4.3 need not be specified to assess the initiation angle and relative mixed-mode toughness for the homogeneous problem, as the results of the integration over the classical *K*-field are independent of the choice of radii. However, determining the effects of a strength or modulus gradient on

[3] The expression is obtained by combining the solution for a penny-shaped crack in an infinite body (Tada and Paris, 1985) and the Williams *K*-field, Eq. 4.1.

fracture behavior requires specification of these dimensions, as it is precisely the gradient-induced variations away from the crack tip that will alter the fracture characteristics. Only for sufficiently shallow gradients (low b), or for fracture processes dominated by the very near-tip fields (high m), will the near-tip character of the crack fields be the same as in the homogeneous case. Several examples with sigmoidal variations in σ_0 or E are examined with two sets of integration limits in the r-direction, $\rho = R/10^3$ and $R/10^5$, before generalizing the results.

4.5.2.1 Parallel strength gradient $\sigma_0(x)$

For a functionally graded material with a variation in strength $\sigma_0(x)$ and nominal Mode-I loading, the symmetry of the problem dictates a solution with no kinking on average, $\phi = 0$. However, the initiation fracture toughness K_Φ, i.e., the stress intensity factor that will result in a stated first failure probability (say 50% or 90%), will be affected by the strength of the gradient.

Results for the normalized toughnesses, which do not depend on Φ, are displayed in Fig. 4.9 for two sets of integration and for m from 2 to 11 and $b\cdot(2R) = \{-20,20\}$. For gradients in strength with $b < 0$, which correspond to the cases of cracks growing into weaker material, there is, as expected, a reduction in the predicted initiation toughness. The effect is very strong for lower m, as the failure behavior is increasingly volume-dependent, and farther ahead of the crack tip, larger volumes of weak material can be sampled. However, for cracks growing into stronger material ($b > 0$), a similar, but smaller degradation of initiation toughness trend is also evident. This is a result of the sampling of all material in the neighborhood of the crack tip, not just that in front, $x > 0$.

The material located outside $-\pi/2 < \theta < \pi/2$ is weaker than that just ahead of the crack tip and the steeper the gradient, the weaker that material. Given that the maximum principal stress at $\theta = \pm 114.1°$ is the same as it is at 0° (see Fig. 4.1), this weakness greatly affects the probability integral, although not as much as for a negative gradient.

As for homogeneous mixed-mode fracture (Section 4.5.1.2), these results must be carefully interpreted. Although material fracture is expected at a lower applied K than in the homogeneous case, a cracking event behind the main crack tip is unlikely to trigger total failure of the body, but rather would lead to a zone of distributed damage, or to a discontinuous jump that would later lead to a bridged crack.

4.5.2.2 Infinite body with parallel stiffness gradient, E(x)

Fig. 4.10 shows the range of predicted K_Φ toughness for $E(x)$ gradients, again normalizing to $K_\Phi(b=0)$, Eq. 4.10. The strength, σ_0 is taken to be constant. The stress field used is the FGM modification of the classical stress field (Eq. 4.2).[4] Results displayed for two sets of integration limits show a toughening for $b < 0$ and low values of m. That is, for a given crack-tip K, the probability of failure is lower for cracks growing into more compliant material. In contrast, large reduction in the toughness is seen for $b > 0$, but again only for relatively low m.

The effect is clearly a result of the form of the modified K-field. For cases with elevated stresses ahead of the crack, $b > 0$, the failure probability is increased, and thereby the toughness is decreased. The opposite is true of the $b < 0$ case at modest level of $-b$, where stresses ahead of the crack are lower for a given K.

[4] Commentary on the accuracy of this approximation can be found in Section 4.5.3.3

4.5.2.3 Infinite body with perpendicular strength gradient, $\sigma_o(y)$

The classical formulae for crack kinking indicate the preferred direction for extension to be along 0° for Mode-I loading, but for an FGM with a normal gradient in the Weibull strength, $\sigma_0(y)$, the spatial variation in strength results, on average, in a preferred non-zero initiation angle, ϕ. Fig. 4.11 shows the range of predicted ϕ, and as these results are an odd function of the gradient strength ($\phi(b) = -\phi(-b)$), only for a positive range of $b \cdot (2R) = \{0,5\}$. A strong dependence on $\sigma_0(y)$ is observed, with the average initiation angle approaching 80° for very low Weibull modulus materials ($m < 5$). Even for higher m, there is a transition to cracking at 80° although the critical gradient increases sharply with m.

Note that toughness results for $\sigma_0(y)$ show similar trends as for the case of $\sigma_0(x)$, with a degradation of toughness exhibited. The actual curves are more similar to the $b < 0$ region of Fig. 4.9. Therefore, not only will the crack tend to grow into the weaker material with a variation in strength present, $\sigma_0(y)$, but fracture initiation will occur at a lower applied K than in the homogeneous case

4.5.2.4 Infinite body with normal stiffness gradient, E(y)

Crack initiation was studied for infinite bodies with $E(y)$. The stress field is approximated by Eq. 4.2 and the strength, σ_0 is again taken to be constant. First, the effects of the gradient-induced terms in the stress field are examined by analyzing a pure mode-I field near the tip with the $E(y)$ modification. Fig. 4.12 displays the effect of the gradient on the fracture toughness for $b \cdot 2R = \{0,20\}$. A degradation of over 25%

compared to the homogeneous case is evident for the low-m (m = 2,3) cases, purely due to the elevated stress in the regions of material with increased modulus.

For the majority of situations, the existence of a stiffness gradient normal to the crack plane causes mixed-mode loading at the crack tip (Erdogan, 1995). The FGM stress field depends on the geometry-specific relationship between the modulus gradient and the phase angle. The average initiation angles for an infinite sample with a range of Weibull moduli from $m = 2$ to 11 are displayed in Fig. 4.13 for a range of $b \cdot (2R) = \{0,20\}$ (as ϕ is an odd function of gradient strength). However, to facilitate comparison with the subsequent analysis of the SE(T) specimen, the phase angles used are increased with b to match the $\psi(b)$ data of the subsequent Fig. 4.14.

The results for the FGM field compare reasonably well with the cracking angles for homogeneous field for high m. For instance, for $b = 10$, $\psi = 18.1°$, and for $m = 9 - 15$, $\phi_{FGM} = -50°$ to $-60°$, which is similar to that for homogeneous materials at the same ψ. At low m, the agreement is poor, with cracking angles being near to zero for graded materials. This difference arises because the high-m, small ρ case is dominated by the stresses of the very near-tip field, which, being essentially those of the classical Williams singularity, are affected by the gradient primarily through the phase angle, ψ, unless b is very large. As the gradient is made steeper (from $b \sim 10$-20), the phase angle nearly plateaus, as seen by the dashed line in Fig. 4.14. However, the assumed multiplicative effect of the modulus field on the stress field, Eq. 4.2, does not change in form as the gradient steepness increases. Thus, from Eq. 4.2, for a fixed phase angle, an increase in modulus will increase the stresses at $y > 0$ (as compared to the homogeneous case with the same ψ). The resulting sampling of the whole body will recognize this elevated stress

level; for sufficiently low m, it will dominate, as implied by the insensitivity to ρ. Thus, near-tip stresses for $\psi > 0$ drive the crack in the negative y-direction while the gradient-induced stresses drive the crack in the positive y-direction. This leads to the average initiation angle being substantially decreased (less negative) in the FGM computed with larger ρ, compared to the homogeneous case and the same ψ; furthermore, this effect is strongest at lower m, such that the results are more dependent on the next-order terms in the stress singularity solution (here, because of the modulus gradient).

4.5.2.5 Implications

Gradients in material properties affect the toughness in two distinct ways, the initiation toughness and the crack angle including its dispersion. Both have implications for the final fracture.

The trends depicted, as well as behavior for other conditions, can be understood in terms of the most probable radial distance from the crack tip for cracking to initiate. The local cumulative cracking probability is $p(\sigma)\mathrm{d}V/V_0$, and so the fracture probability in an annulus at a given radial distance from the tip increases with $\int_{-\pi}^{\pi} p(\sigma) r\, d\theta$. Thus, key trends are revealed by the behavior of the weighted probability function $p^*(K,r) \equiv p(\sigma(r))r$ where $p(\sigma)$ is given in Eq. 4.4 (with a possible gradient in σ_0) and $\sigma(r)$ is given by Eq. 4.2 with $\theta = 0$.

In a homogeneous materials, cracking frequencies decrease with increasing r for all $m > 2$ in a linear elastic stress field. However, for a sigmodal gradient in either σ_0 or E, under certain conditions a local minimum and maximum in p^* exist at radial positions

r_n and r_x, respectively, as depicted in Fig. 4.14. From conditions based on $dp^*/dr = 0$, it can be ascertained that these occur at $0 < r_n < r_x$, and that they scale with $1/b$.

The key issue concerns the strength of the maxima, in particular the relative values of σ/σ_o and especially of p^* at r_x versus at the cut-off distance ρ. The cases of $\sigma_o(x)$ with $b{\cdot}2R = -20$ and $E(x)$ with $b{\cdot}2R = 20$ for $m = 3$ and 11 provide an illustrative range of examples. Values for $r_x b$ are listed in Table 4.1 as are ratios of σ/σ_o and of p^* (at r_x and ρ) taking $b\rho = 10^{-4}$ and 0.01, the limiting conditions for the plots in Figs. 4.9 – 4.13. For most of these cases, maxima exist for the weighted probability p^*, but they span a range from the local peak σ/σ_o being low but relevant versus that at ρ to $\sigma/\sigma_o(r_x)$ being too small to influence the cracking probability.

Table 4.1. Parameters for local maxima in cracking probability

	$m = 3$		$m = 11$	
$\sigma_o(x)$, $c = 10$	$\rho b = 0.01$	$\rho b = 0.0001$	$\rho b = 0.01$	$\rho b = 0.0001$
$r_x b$	3.26	3.26	2.69	2.69
$\sigma/\sigma_o\|_{rx}/\sigma/\sigma_o\|_\rho$	0.55	0.055	0.61	0.061
$p^*(r_x)/p^*(\rho)$	$(3.79)^3$	$(1.76)^3$	$(1.01)^{11}$	$(0.15)^{11}$
$E(x)$, $c = \infty$	$\rho b = 0.01$	$\rho b = 0.0001$	$\rho b = 0.01$	$\rho b = 0.0001$
$r_x b$	1.7	1.7	0.6 [5]	0.6 [5]
$\sigma/\sigma_o\|_{rx}/\sigma/\sigma_o\|_\rho$	0.14	0.014	0.19	0.019
$p^*(r_x)/p^*(\rho)$	$(0.78)^3$	$(0.36)^3$	$(0.27)^{11}$	$(0.041)^{11}$

[5] Inflection only for this condition

Thus, if a gradient is oriented so that the direction of increasing E/σ_o is aligned with the region of high $f_I(\theta,\psi)$, a reduced toughness results with even modest gradient

intensities, and the damage will be much more focused for both degradation regimes (low and intermediate m). This is shown in Table 4.2, which lists the median cracking angles θ_{50} and the dispersion in cracking angles, as $\theta_{75} - \theta_{25}$, for several situations involving gradients in σ_o with $b{\cdot}2R = \{-20,0,20\}$. In particular θ_{75}-θ_{25} is smaller if $b<0$.

In contrast, if the alignment is opposite, the toughness may rise with moderate gradient levels in low-m materials, but diminish for more intense gradients even with higher m values. This is clear in Fig. 4.9 for variations in $\sigma_o(x)$ and implied by extrapolating the curves for gradients in $E(x)$ in Fig. 4.10 to higher $-b$. In essence, material beyond the crack by $r > 1/b$ ($\theta > 0$) becomes relatively stronger than without a gradient, and so the total failure probabilities can be reduced for m low enough that cracking at large r is relevant. However, the degradation in K_Φ with a steeper gradient entails fracture at the crack flanks, as shown in Table 4.2 for $\sigma_o(x)$ at $b > 0$ for which $\theta_{75} - \theta_{25}$ becomes very large.

Table 4.2. Effect of gradient on angular dispersion of first fracture

$\psi = 0°$ ($\theta_{\sigma\theta\theta|max} = 0°$)

$\sigma_o(x)$	$m = 3$		$m = 11$		$\sigma_o(y)$	$m = 3$		$m = 11$	
b	θ_{50}	θ_{75}-θ_{25}	θ_{50}	θ_{75}-θ_{25}	b	θ_{50}	θ_{75}-θ_{25}	θ_{50}	θ_{75}-θ_{25}
-20	0°	70°	0°	64°	-20°	73°	42°	72°	24°
0	0°	124°	0°	118°	0°	0°	124°	0°	118°
20	0°	244°	0°	124°	20°	-73°	42°	-72°	24°

$\psi = 45°$ ($\theta_{\sigma\theta\theta|max} = 52°$)

$\sigma_o(x)$	$m = 3$		$m = 11$		$\sigma_o(y)$	$m = 3$		$m = 11$	
b	θ_{50}	θ_{75}-θ_{25}	θ_{50}	θ_{75}-θ_{25}	b	θ_{50}	θ_{75}-θ_{25}	θ_{50}	θ_{75}-θ_{25}
-20	-19°	51°	-27°	28°	-20°	+46°	39°	-83°	80°
0	-74°	100°	-88°	72°	0°	-74°	100°	-88°	72°
20	-146°	32°	-150°	25°	20°	-90°	57°	-90°	38°

Obviously from inspection of Fig. 4.1, it can be seen that if a cracking condition depending upon the hoop stress, $\sigma_{\theta\theta}$, were pertinent, the tendency of weakening effects to outweigh local strengthening would be lessened owing to the narrower angular range of singular crack-tip stresses.

The probable angle of crack initiation can also be shifted by the presence of a gradient. It should be noted that the angular location of cracking that occurs near ρ can be changed at relatively small levels of b, that is at levels at having only minimal affects on K_Φ. This emerges from comparing the levels of b that markedly change the crack angle with a gradient in $\sigma_o(y)$, Fig 4.11, with the much larger levels of $-b$ needed to alter the toughness with $\sigma_o(x)$, Fig. 4.10. This follows because the angular dependence of the crack-tip stresses, especially σ_1, is rather weak over a wide interval, Fig. 4.1a, and so the angle of the maximum stress can be appreciably perturbed even by a shallow material gradient.

An equally important issue concerns whether the range in probable crack initiation angles or the difference in initiation angle and stable extension angle is made larger or narrower by the presence of a gradient. Expected trends are again illustrated in Table 4.2. For situations in which the range of initiation angles is raised with increasing gradient, a microcrack or bifurcation zone would be wide, or more diffuse, especially for low m. This should raise the difference between the loads for first cracking and final failure, i.e., affect the strength of the R-curve. Where the zone of probable cracking is narrower, i.e., focused, the fracture surface will be less rough and the R-curve relatively flatter.

For mixed-mode loading, the expected microcrack zone tends to be less wide, Table 4.2. However, the average location depends strongly on m and is unlikely to be on the path of the eventual main crack. It is assumed that subsequent cracking would statistically tend to be along the path of maximum G, approximately that of maximum $\sigma_{\theta\theta}$. When these angles differ, rising R-curve effects could also be significant.

Thus, the presence of a strength gradient would almost invariably lower the toughness for first cracking, but unless the weak material were largely ahead of the crack, the corollary effect would be to markedly widen the damage zone perhaps even enough to induce a net increase in final toughness when there is a substantial trend toward first cracking occurring near the crack flanks. For modest modulus gradients, the effects on first cracking and final cracking would tend to be the same rather than offsetting unless the gradient were nearly normal to the crack. Thus, situations with some toughening both for first cracking and from a rising R-curve can exist.

4.5.3 FEA of finite-sized specimens

Although dependencies of the toughness and initiation angle on the modulus gradient emerge for the infinite body FGM (Section 4.5.2) due to the gradient induced modification of the stress field, at finite r, deviations from the classical K-field can also be expected even in homogeneous materials. For cracks in finite bodies, boundary condition-induced higher-order terms in the Williams expansion will dictate the stress field at increasing distance from the crack tip. Thus, it should be appreciated that fracture toughness for a very low Weibull modulus material could depend in detail upon the actual specimen size and geometry under consideration. By comparing the results of an

infinite body (sections 4.5.2) and those derived from finite element results (containing the full stress field solution) for a specific specimen geometry, it can be determined which effect, geometry or gradient, is likely to dominate a problem. After describing the calibration of the single-edge crack tension SE(T) sample, several examples will be given in which the failure probabilities are computed based on stresses in the entire sample excluding a zone within $\rho = a/10^5$ and $a/10^3$.

4.5.3.1 Specimen Calibration

A modulus gradient parallel to the direction of the crack, $E(x)$, retains the symmetry of the homogeneous problem so that $K_{II} = 0$. For homogeneous materials with load boundary conditions, the stress intensity factor is not influenced by the Young's modulus; however, for an FGM, the magnitude of the mode-I stress intensity factor K_I is increased for $b < 0$ and decreased for $b > 0$ as shown in Fig. 4.15 for the SE(T) geometry with $a = W/2$ (Fig. 4.3). This behavior is consistent with other observations relating the far-field load and K_I for an FGM with $E(x)$ (Erdogan, 1995).

Deterministic failure comparisons based on loads can be directly inferred from the results of Fig. 4.15. This indicates that cracks growing into positive b gradients are expected to carry higher loads than homogeneous or negative b materials when fracture is determined by a critical K_{Ic} or near tip $\sigma_{\theta\theta}$.

The effect of a modulus gradient normal to the direction of the crack, $E(y)$, is to take a nominally mode-I geometry and load the crack tip in both tension and shear. The mixed-mode calibration for the stress intensity factors, K_I and K_{II}, is also shown in Fig. 4.15. K_I is an even function of b, $K_I(b) = K_I(-b)$ and K_{II} is odd. An amplification of both stress intensity factors is observed with increasing $|b|$, but with a resulting monotonic

growth in the tip phase angle, $\psi = tan^{-1}(K_{II}/K_I)$ (dashed line). This trend seems to plateau for $b{\cdot}2a > 10$, as ψ shifts from 0 to 18° as $b{\cdot}2a$ goes from 0 to 10 but only an additional 2° from $b{\cdot}2a = 10$ to 20.

The subsequent results depend on calculation of the stress field of the entire sample, not only those pertinent to the asymptotic crack tip, Eq. 4.1. The deviations of these stresses for a homogeneous modulus from those of Eq. 4.1 are displayed in Fig. 4.16 (curve labeled $b = 0$). These stresses deviate weakly from those of Eq. 4.1 compared to those with a $E(x)$ gradient present, also shown for $b{\cdot}2a = \{20,-20\}$.

4.5.3.2 SE(T) with parallel strength gradient, $\sigma_o(x)$

A SE(T) sample with strength gradients $\sigma_o(x)$ but homogeneous modulus, E, was first modeled using finite element analysis. The variation in the fracture toughness, K_Φ as a function of strength gradient is shown in Fig. 4.17. Results for a range of gradients with $b{\cdot}2a = \{-20,20\}$ are plotted, with the integration of the failure probability integral excluding a zone of size ρ. Fig. 4.17a displays a reduction in toughness for all gradients when $m < 7$. For the case of the larger cutoff region (Fig. 4.17b), the degradation in toughness occurs for $m \leq 11$. The $\rho = a/10^5$ case biases the results toward the homogeneous situation, which lessens the effects on toughness as seen in Fig. 4.17a. It is worth noting the general agreement between the results in Figs. 4.17 and 4.9, the latter which only utilize the Williams expansion near the crack tip (but have a cutoff R). However, there are discernable differences even for intermediate m values for which most cracking occurs between ρ and r_x.

4.5.3.3 SE(T) with parallel modulus gradient, E(x)

The calculated statistical fracture toughness, K_Φ, for a range of modulus gradients $E(x)$ are plotted in Fig 4.18. These toughnesses are normalized to the toughness of a homogeneous body and are, therefore, insensitive to the failure probability, Φ, chosen as a basis for comparison. It is clear that for a crack growing into a stiffer material, there is a decrease in the toughness of the structure for material with low m. Conversely, there is a toughening effect for cracks growing into a more compliant material. Again the effect of a gradient is stronger for the case with the larger ρ (Fig. 4.18b).

These results, which are obtained from the finite element analysis of the SE(T) fracture mechanics sample, utilize the stress field of the entire sample, and effects are due to both the modulus gradient and the finite geometry. Prior calculations with a linear $E(x)$, rather than a sigmoidal variation, exhibited similar trends, but which differed in detail (Becker, *et al.*, 1999).

The trends of a large influence of the gradient with low m correspond to the most probable location of fracture initiation moving away from the crack tip, where the form of the stress solution deviates from the classical form, as was seen in Fig. 4.16. These results indicate that although K is a valid scaling parameter for the stress field very near the crack tip for an FGM, the dependence of the stress field ahead of the crack on the gradient in E renders K_Φ to be an inaccurate predictor of failure if the fracture initiation occurs away from the tip. These effects arise because the stresses ahead of the crack tip, and hence the failure probability, are higher with a positive gradient than would exist for a homogeneous material at the same K.

The trends agree in Figs. 4.18 and 4.10; however, the infinite body analysis only utilizes the first two terms in the asymptotic expansion near the crack tip and

underestimates the magnitude of the effect of the gradient. The reason can again be see in Fig. 4.16. Here the maximum principal stress σ_1 ahead of the crack tip (along $y = 0$) is plotted for the $b = \{-20,0,20\}$ cases; also plotted are the variations in the modulus for the same gradient cases $b = \{-20,20\}$. The homogeneous stress solution is found to deviate slowly from the classical K-field, with exact agreement as $x \rightarrow 0$ (by nature of the fitting routine for K) and 20% error at $x/(2a) = 0.1$. Eq. 4.2 describes the stress field in the FGM as that of the homogeneous field multiplied by the pointwise variation in modulus. Fig. 4.16 demonstrates that although this methodology results in a better estimate of the stress field than the Williams field, it underestimates the true change in stress for FGMs as calculated by the finite element analysis, even at $x|b| << 1$. Therefore, the infinite body analysis of Section 4.5.2.2 apparently uses a stress field which varies too weakly with b and, especially for $b < 0$, the overall effect on the fracture behavior is underestimated. For example, for $m = 4$ and $b = -10$ in the infinite body with the larger cutoff region, $K_\Phi(b)/ K_\Phi(0) = 1.1$, and for the SE(T) geometry, $K_\Phi(b)/ K_\Phi(0) = 1.6$.

4.5.3.4 SE(T) specimen with perpendicular strength gradient, $\sigma_o(y)$

For the SE(T) specimen with gradients in strength $\sigma_o(y)$ varying over $b = \{0,5\}$, the average angle of initiation is displayed in Fig. 4.19. The results are in good agreement with those in Fig. 4.11, with a large negative initiation angle predicted for positive gradient, $\phi \cdot b < 0$. The lower the value of m, the larger the average initiation angle will result, until $\phi = 90°$ at sufficient b. As increasing distances from the crack tip participate in the fracture event at low m, the lower strength material will dominate the problem. For high m, (> 9 for $\rho = a/10^5$, >15 for $\rho = a/10^3$), the very near-tip region

dominates the calculation for the b levels explored, where the strength variation is limited and the symmetry of the stress field dictates a $\phi = 0°$ solution. Overall the results compare favorably to those in Fig. 4.11; however, the sensitivity to increasing m is notably greater for the finite sample.

4.5.3.5 SE(T) specimen with perpendicular modulus gradient, E(y)

The average initiation angles for the SE(T) specimen and a modulus gradient $E(y)$ for a range of m from 2 to 15 are shown in Fig. 4.20(a). As ϕ is an odd function of gradient strength, only a range of $b = \{0,20\}$ is plotted. The dramatic effect of m is evident. First, for high m ($m > 10$), positive gradients lead to negative initiation angles, i.e., $\phi \cdot b < 0$. The high-stress near-tip region of the sample, which experiences a shift in phase angle, dominates these results. As seen for the infinite body analysis for both homogeneous material and FGMs, positive phase angles lead to crack initiation angling downward, $\phi < 0$ for $\psi > 0$.

In contrast, for the very low values of m, the average direction of initiation is positive for positive gradients, $\phi \cdot b > 0$. This is in response to higher stresses associated with the increasing modulus in the positive y-direction, which is only important when cracking is widely distributed. In comparison with the results in Fig. 4.13, this effect of a gradient for low m is even more drastic. This is again due to the fact that Eq. 4.2 underestimates the effect of $E(y)$ on stress at finite distances away from the crack tip. Although the modulus adjusted K-field analysis does not exactly mimic the extent of the low-m behavior, the mitigation of the near-tip tendency to initiate downward cracking for positive $\psi(b)$ is evident.

4.5.3.6 M(T) specimen with perpendicular modulus gradient, E(y)

To further illustrate the effect of geometry in the presence of a modulus gradient, a middle cracked tension (MC(T)) fracture mechanics specimen was also analyzed with a variation $E(y)$. This geometry is known to develop a markedly different stress distribution for homogeneous materials outside of the K-dominant region. The nonsingular compressive T-stress in the M(T) sample is twice the magnitude of that in the SE(T) sample (Sherry *et al.*, 1995). Also, there is a change in sign in the deviation of the σ_{yy} stress from the K-field due to higher-order geometry terms (Knott, 1973).

The two salient trends, namely tip-dominated, negative angles for $m > 7$, and positive average initiation angles for $m = 2,3$ are evident for both sample geometries. However, the initiation angles for large b are shifted to about 20° lower values for all m for the M(T) sample. The other differences are mainly expressed for the intermediate m where neither tip nor far-field stresses dominate. It is interesting to note that the phase angle-gradient relationship for these two samples was shown to be very similar, thus indicating that the differences in Fig. 4.20 arise on the basis of b and not $\psi(b)$. At low m the crack initiation trends in Figs. 4.20(a) and (b) for the two samples are more similar compared to the infinite case, Fig. 4.13, but differences are notable.

4.5.3.7 Implications for fracture experiments and application to FGMs

Effects with far-field mode-I loading and variable $\sigma_o(x)$, $\sigma_o(y)$, $E(x)$ and $E(y)$ have been explored. For more general cases with far-field mixed-mode loading and an FGM with arbitrary $\sigma_o(x,y)$ and $E(x,y)$, the space of possible combinations is prohibitively large to completely survey. The results thus far presented for $m > 6$ indicated that behavior is

somewhat similar between the finite and infinite bodies. Therefore, Eq. 4.2 for analysis of infinite bodies can be used in conjunction with Eq. 4.11 to anticipate the results of cases not explored here; however, the geometry induced shifts in phase angle with elastic modulus gradient must be known. Using this, it can be observed that as a plausible approximation for real materials, $\sigma_0 \propto E$, some of the gradient effects could tend to compensate; nonetheless, large effects of low m and induced ψ, Figs. 4.5 and 4.6, still pertain.

For lower and intermediate m, the fracture behavior may not be adequately determined by the stresses within the K-field of a finite geometry. Even when failure occurs near the crack tip, gradient induced perturbations influence crack angles. For these cases, the combined effects at near crack-tip, gradient-induced and geometry determined stresses must be taken into account. This must be done though numerical determination of the stress field, e.g., through finite element analyses. This is, by comparison, a more expensive procedure than the semi-analytic modeling of infinite bodies.

The nonlinear fracture mechanics of ductile materials is most simply characterized using a single parameter, J; however, this still leads to an appreciable geometry-to-geometry variability in measured crack-growth resistance for many materials. The T-stress (or, nearly equivalently, the constraint factor, Q) has been evoked to account for the next term in the nonlinear stress field expansion about the crack tip (Du and Hancock, 1991). This two-parameter characterization allows the description of the material not only at the crack tip, but also at finite distances, and thereby is more successful in determining critical conditions for crack initiation and growth.

The characterization of the stress field in an FGM by the single parameter K has similar limitations. The approximate formulation (Eq. 4.2) alludes to the form of the next higher-order term in the expansion. Although in the asymptotic near-tip limit one could also assume the existence of a parallel T-stress, this suffers from the same incompatibility discussed in Section 4.2. It seems likely that the addition of a single parameter, a "b-stress", can be used to more accurately describe the stress field in an FGM and, therefore also provide a powerful two-parameter scheme to predict crack behavior in different geometries and gradients, at lease for the intermediate and high-m material. Indeed, analysis in Chapter 5 explicitly shows the existence of a large gradient-induced T-stress for a crack with $E(y)$. However, the present results indicate that either such a second parameter must be geometry dependent, or perhaps a three-parameter treatment would be superior

4.6 Summary and Conclusions

The application of two-parameter Weibull statistics to near-crack fracture problems has been elaborated and extended to the case of mixed-mode loading, with predictions made for both the toughness and average initiation angle of a crack in a brittle material. This fracture model allows for the statistical correlation between near-tip stresses and first fracture for heterogeneous materials. This is especially interesting for problems in functionally graded materials (FGMs), where the stress and strength fields are known to vary from the homogeneous form away from the crack tip. Infinite-body and finite element analyses reveal that:

- For statistically homogeneous materials, the mixed-mode loading of an elastic crack subject to a stress-controlled failure criteria results in a reduction

of the fracture toughness by up to 30%, depending on the phase angle ψ and Weibull modulus m. This is roughly 150% of the effect predicted by mechanisms triggered by $\sigma_{\theta\theta}$, usually invoked for continuous kinking.

- The angle of microcracks initiated by the main crack stress field do not coincide with that determined by maximum energy criteria. Thus, crack bridging or the tearing of ligaments must occur for crack advance, thereby expectedly leading to toughening for materials that fail by cracking ahead of the main crack.
- Gradients in Weibull scaling stress $\sigma_0(x)$ lead to a dramatic decrease in fracture toughness for crack growing into either weaker, $b < 0$, or stronger, $b > 0$, materials. Gradients normal to the crack $\sigma_0(y)$ lead to weakening for first fracture and also to crack growth initiating at non-zero angles that may offset this effect for final failure.
- Gradients in modulus $E(x)$ for a single-edge notched fracture mechanics specimen lead to an increased stress intensity factor for cracks growing into more compliant materials, and crack-tip shielding when growing into a stiffer material.
- When comparing FGMs with gradients in the Young's modulus, E, and the same crack tip stress intensity, the crack growing into the steeper negative gradient, $b < 0$, will be tougher for moderate gradients.
- Gradients in modulus $E(y)$ for a single edge-cracked tension SE(T) sample lead to initiation behavior similar to that in homogeneous materials with the same phase angle for $m > 5$, with the average angle $\phi < 0$ for $b > 0$; for lower

Weibull modulus, though, the effects of the modulus gradient on the stress field cause the average fracture initiation site to be skewed toward the higher modulus region, $\phi > 0$ for $b > 0$.

- Infinite-body analyses predict many of the gradient–induced features seen in a finite geometry. When comparing two fracture-mechanics specimen geometries, additional effects of gradient on crack initiation angle were found to be important. There is scope for further analysis which incorporates higher-order terms in the stress field.
- The evolution of damage near a crack tip will vary strongly with the Weibull modulus, m, of the material. For low m materials, a distribution of damage is expected before catastrophic crack advance. The effects of considering "action-at-a-distance" are many-fold. Most importantly, the first flaws to be activated in a mixed-mode loading are most likely not in line with what is considered to be the energetically most favorable path. Therefore, it is expected that materials with wide distributions of strength will develop diffuse microcracking damage zones around the crack tip. At elevated loads, one expects that these microcracks will link up, or the main crack will jump beyond this damage zone. Under either scenario, the tearing or bridging that results will be act as an R-curve mechanism.

4.7 References

Amada, S., Ichikawa, Y., Munekata, T., Nagase, Y. and Shimizu, H., 1997. Fiber texture and mechanical graded structure of bamboo. *Composites*, Part B 28B, 13-20.

Becher, P.F., 1991. Microstructural design of toughened ceramics, *J. Am. Ceram. Soc.* 74, 255-69.

Becker, T. L., Cannon, R. M. and Ritchie, R. O., 1999. A statistical RKR fracture model for the brittle fracture of functionally graded materials. *Mater. Sci. Forum* 308-311, 957-62.

Becker, T. L., Cannon, R. M. and Ritchie, R. O., 2000. An approximate method for residual stress calculation in functionally graded materials. *Mech. Mater.* 32, 85-97.

Beremin, F. M., 1983. A local criterion for cleavage fracture of a nuclear pressure vessel steel. *Metall. Trans. A*, 14A, 2277-87.

Blonski, S. and Garofalini, H., 1997. *J. Am. Ceram. Soc.*, 80 1997-2004.

Cotterell, B., 1965. On brittle fracture paths. *Int. J. Fract. Mech.* 1, 96-103.

Cotterell, B., 1966. Notes on the paths and stability of cracks. *Int. J. Fract.* 2, 526-33.

Cotterell, B. and Rice, J. R., 1980. Slightly curved or kinked cracks. *Int. J. Fract.* 16, 155-69.

Curry, D. and Knott, J. F., 1979. Effect of microstructure on cleavage fracture toughness of quenched and tempered steels. *Metal Science* 13, 341-45.

Curry, D. A. and Knottt, J. F., 1976. The relationship between fracture toughness and microstructure in the cleavage fracture of mild steel. *Metal Science* 10, 1-6.

Delale, F. and Erdogan, F., 1983. Interface crack in a nonhomogeneous elastic medium. *Int. J. Engng. Sci.* 26, 559-68.

Du, Z. Z. and Hancock, J. W., 1991, The effect of non-singular stresses on crack-tip constraint. *J. Mech. Phys. Solids*, 39, 555-67.

Erdogan, F., 1985. The crack problem for bonded nonhomogeneous materials under antiplane shear loading. *J. Appl. Mech.* 52, 823-28.

Erdogan, F., 1995. Fracture mechanics of functionally graded materials. *Compos. Engng.* 5, 753-70.

Erdogan, F. and Sih, G. C., 1963. On the crack extension in plates under plane loading and transverse shear. *J. Basic Engng., Trans. ASME*, 85, 519-27.

Evans, A. G., 1978. A general approach for the statistical analysis of multiaxial fracture. *J. Am. Ceram. Soc.* 61, 302-08.

Evans, A. G., 1983. Statistical aspects of cleavage fracture in steel. *Metall. Trans. A* 14A, 1349-455.

Evans, A. G., 1989. High toughness ceramics. *Mater. Sci. Engng.* A105/106, 65-75.

Geubelle, P. H. and Knauss, W. G., 1995. Crack propagation in homogeneous and bimaterial sheets under general in-plane loading: Nonlinear analysis. *J. Appl. Mech.* 62, 601-06.

S. H. Garofalini, private communication (1999)

Gopal, M. (1997). Joining of silicon nitride ceramics to itself and to the other materials using chemically compatible interlayers. *Ph.D. thesis*, Dept. Mater. Sci. Miner. Engng., Berkeley, University of California.

Gu, P. and Asaro, R. J., 1997. Crack deflection in functionally graded materials. *Int. J. Solids Struct.* 34, 3085-98.

Gumbsch, P. and Cannon, R. M., 2000. Atomistic aspects of brittle fracture, *MRS Bulletin*, in press

He, M.-H. and Hutchinson, J. W. , 1989. Kinking of a crack out of an interface. *J. Appl. Mech.* 56, 270-8.

He, M.-Y., Bartlett, A., Evans, A. G. and Hutchinson, J. W. , 1991. Kinking of a crack out of an interface: role of in-plane stress. *J. Am. Ceram.* Soc. 74, 767-71.

Hong, T., Smith, J. R. and Srolovitz, D. J., 1995. Theory of metal-ceramic adhesion. *Acta Metall. Mater.* 43, 2721-30.

Hutchinson, J.W., 1987. Crack tip shielding by micro-cracking in brittle solids. *Acta Metall.,* 35, 1605-19.

Hutchinson, J. W., 1968. Singular behavior at the end of a tensile crack in a hardening material. *J. Mech. Phys. Solids* 16, 13-31.

Ishibashi, H., Saiz, E. and Tomsia, A. P. , 1997. Mo/SiO2 FGMs fabricated by slip casting. Am. Ceram. Soc. Bull., 76, 231.

Jin, Z.-H. and N. Noda, N., 1994. Crack-tip singular fields in nonhomogeneous materials. *J. Appl. Mech.* 61, 738-40.

Jin, Z.-H. and Batra, R. C. , 1996. Some basic fracture mechanics concepts in functionally graded materials. *J. Mech. Phys. Solids* 44, 1221-35.

Knott, J. F., 1973. *Fundamentals of Fracture Mechanics*. Butterworth, London.

Konda, N. and Erdogan, F., 1994. The mixed mode crack problem in a nonhomogeneous elastic medium. *Engng. Fract. Mech.* 47, 533-45.

Krell, T., Schulz, U., Peters, M., Kayseer, W.A., 1999. Grade EB-PVD alumina-zirconia thermal barrier coatings-an experimetnal approach. *Mater. Sci. Forum* 308-311, 396-401.

Lei, Y., O'Down, N. P., Busso, E. P. and Webster, G. A., 1998. Weibull stress solutions for 2-D cracks in elastic and elastic-plastic materials. *Int. J. Fract.* 89, 245-68.

Lin, T., Evans, A. G. and Ritchie, R. O., 1986a. A statistical model of brittle fracture by transgranular cleavage. *J. Mech. Phys. Solids* 34, 477-97.

Lin, T., Evans, A. G. and Ritchie, R. O., 1986b. Statistical analysis of cleavage fracture ahead of sharp cracks and rounded notches. *Acta Metall.* 34, 2205-16.

Mai, Y.-W. and Lawn, B. R., 1986. Crack stability and toughness characteristics in brittle materials, *Ann. Rev. Mater. Sci.*, 16, 415-39.

McClintock, F. A., and Zaveral, F., 1978. An analysis of the mechanics and statistics of brittle crack initiation. *Int. J. Fract.*, 25, 107-18.

McClintock, F. A., 1997. A three-dimensional model for polycrystalline cleavage ang problems in cleavage after extended plastic flow or cracking. in: Chan, K.S., (ed.), *Cleavage Fracture. George R. Irwin Symp.* TMS, Warrendale, PA, pp. 81-94.

Mecholsky, J. J., Jun, S. W., Freiman, R. W. and Rice, R. W.,1976. Fracture surface analysis of ceramics, *J. Mater. Sci.,* 11, 1310-19.

O'Dowd, N. P., Stout, M. G. and Shih, C. F., 1992. Fracture toughness of alumina-niobium interfaces: Experiments and analyses. *Philos. Mag.* A66, 1037-64.

Palaniswamy, K. and Knauss, W.G., 1978. On the problem of crack extension in brittle solids under general loading. in: S. Namat-Nassar (ed.) *Mechanics Today*, Vol. 4. Pergamon Press, New York, 1978.

Parsons, W. B., 1939. *Engineers and Engineering in the Renaissance*. Williams and Wilkers, Baltimore, MD.

Rice, J. R. and Johnson, M. A., 1970. The role of large crack tip geometry changes in plane strain fracture. in: M. Kanninen, W. Adler, A. R. Rosenfield, R. Jaffee, (eds.) *Inelastic Behavior of Solids*. McGraw-Hill, N.Y., pp. 641-72.

Rice, J. R. and Rosengren, G. F., 1968. Plane strain deformation near a crack tip in a power law hardening material, *J. Mech. Phys. Solids*, 16, 1-12.

Rödel, J., 1992. Interaction between crack deflection and crack bridging, *J. Eur. Ceram. Soc.*, 10, 143-50.

Ritchie, R. O., Knott, J. F. and Rice, J. R., 1973. On the relationship between critical tensile stress and fracture toughness in mild steel. *J. Mech. Phys. Solids* 21, 395-410.

Ruggieri, C. and R.H. Dodds, J., 1996. A transferability model for brittle fracture including constraint and ductile tearing effects: a probabilistic approach. *Int. J. Fract.* 79, 309-40.

Rühle, M., Evans, A. G., McMeeking, R. M. , Charalambides, P. G. and Hutchinson, J. W. 1987. Microcrack toughening in zirconia toughened alumina, *Acta Metall.* 35, 2701-10.

Rühle, M., Claussen, N., and Heuer, A. H., 1986. Transformation and microcrack toughening as complementary processes in ZrO_2-toughened Al_2O_3. *J. Am. Ceram. Soc.* 69, 195-99.

Sand, Ch., Adler, J., Lenk, R., 1999. A new conceprt for manufacturing sintered materials with a threee dimensional composition gradient using a silicon carbide-titanium carbide composite. *Mater. Sci. Forum* 308-311, 65-70.

Singh, D. and Shetty, K.S., 1989. Fracture toughness of polycrystalline ceramics in combined mode I and mode II loading. *J. Am. Ceram. Soc.*, 72, 78-84.

Sherry, A. H., France, C.C. and Goldthorpe, M. R., 1995. Compendium of T-stress solutions for two and three dimensional cracked geometries. *Fatigue Fract. Engng. Mater. Struct.* 18, 141-55.

Tada, H., Paris, P. C. and Irwin, G. R., 1985. *The Stress Analysis of Cracks Handbook.* Del Corp./Paris Productions, Inc., St. Louis, Mo.

Ishibashi, H., Saiz, E., Tomsia, A.P., 1997. Powder processing of Mo/SiO_2 FGMs fabricated by slip casting. *Am. Ceram. Soc. Bull.* 76 (4), 231.

Wallin, K., Saario, T. and Törrönen, K., 1984. Statistical model for carbide induced brittle fracture in steel. *Metal Science* 18, 13-16.

Weibull, W., 1951. A statistical distribution function of wide applicability. *J. Appl. Mech.* 18, 293.

Wu, C.Cm., Freiman, S.W., Rice, R.W., Mecholsky, J.J., 1978. Microstructural aspects of crack propagation in ceramics, *J. Mater. Sci.*, 13, 2659-70.

Williams, M. L. , 1957. On the stress distribution at the base of a stationary crack. *J. Appl. Mech* 79, 109-14.

Xia, L. and Shih, C.F., 1996. Ductile crack growth - III. Transistion to cleavage fracture incorporating statistics. *J. Mech. Phys. Solids* 44, 603-39.

Zienkiewicz, O.C. and Taylor, R.L., 1989. The Finite Element Method. McGraw-Hill, New York, N.Y.

APPENDIX A: MONTE CARLO SIMULATIONS

To illustrate the effects of the elastic near-tip stress field on a material with strength described by Weibull statistics, a Monte Carlo simulation was performed. A domain, 100 units square, was considered with a crack tip at the center {0,0}. For the reasons discussed in Section 4.3.2, a region (with radius 1 unit) was excluded surrounding the crack tip. For each loop in the simulation algorithm:

- Select random location within the domain (outside of the region of exclusion).
- For element with size $\Delta V = r\delta r\delta\theta$, centered at $\{x, y\}$, compute $\Phi^{\Delta V}$ from Eq. 4.1 and Williams stress field. $\delta r = 0.1$ unit and $\delta\theta = 10°$.
- Select random $\{ \Phi_{test}^{\Delta x} \}$ (between 0 and 1)

  $\Phi_{test}^{\Delta x} < \Phi^{\Delta x} \rightarrow$ "hit" ; the value of $\{x,y\}$ is stored as $\{x, y\}_i^{hit}$; $N^{\text{hits}} = N^{\text{hits}}+1$

  $\Phi_{test}^{\Delta x} > \Phi^{\Delta x} \rightarrow$ "miss" ; the value of $\{x,y\}$ is discarded

Fig. 4.1 displays the results of 5 x 10^6 runs. From these results, averages can be calculated from the location of the "hits".

$$x^{ave} = \frac{1}{N^{hits}} \sum_{i=1}^{N^{hits}} x_i^{hit} \qquad y^{ave} = \frac{1}{N^{hits}} \sum_{i=1}^{N^{hits}} y_i^{hit}$$

For this average location, the angle is $\tan^{-1}(y^{ave} / x^{ave})$. For the mode-I case, this is 4.3°. For a phase angle of $\psi = 45°$ case, the angle of the average location is 80.7°. The different mode loading also resulted in a greater number of "hits" (fracture initiations), with 111 hits for the mode-case and 764 for the mixed-mode case.

4.8 Figure Captions

Figure 4.1: Isostress contours of for (a) maximum principal stress σ_I and (b) hoop stress $\sigma_{\theta\theta}$ for loading phase angles ψ=0°, 45°, 90°. Shapes of contours indicate relative levels of stress, with larger r corresponding to higher larger stress at that θ.

Figure 4.2: Results of Monte Carlo simulations for a brittle material in the neighborhood of a sharp elastic crack. Mode-I, (ψ=0°) and mixed-mode (ψ=45°) cases are displayed for Weibull modulus, m=7. Points around the crack tip at (0,0) indicate the location of a simulated fracture initiation. Strong skewing toward in the negative y-direction is evident for the mixed-mode case, which indicates that the crack will tend to grow downward. The increased number of fracture initiations in the mixed-mode case loaded to the same $|K|$ indicate a decreased fracture toughness.

Figure 4.3: Finite element mesh used in study of SE(T) fracture mechanics specimen. A high degree of refinement was used, with a focused ring of element surrounding the crack tip. A similar mesh with different boundary conditions was used to study the MC(T) sample.

Figure 4.4: Sigmoidal gradient modeled. This shape allowed for an arbitrarily steep gradient at the crack tip, determined by the parameter b. The total range of variation within the sample is held constant, with $g(\infty)/g(-\infty) = 20$.

Figure 4.5: (a) Prediction for the mixed-mode fracture toughness for an infinite body of a homogeneous material based on statistical fracture model for various values of Weibull modulus (solid lines) compared to the deterministic prediction based on critical hoop stress (dashed line). (b) Prediction for the mixed-mode fracture toughness envelope for the statistical model compared to the toughness envelope of Palaniswamy and Knauss (1978) for fitting parameter C=0.82 and 0.87.

Figure 4.6: Average initiation angle for mixed-mode fracture loading for an infinite body of a homogeneous material based on statistical fracture model. Included for comparison are the angles of maximum hoop stress and maximum energy release rate (dashed lines).

Figure 4.7: Contours of cumulative probability for homogeneous material with mixed-mode loading for (a) m=3 and (b) m=11. The median angle, θ_{50}, bisects the total failure probability for the material between $-\pi$ and π. The bands about the median indicate the angles where 50% and 90% of the fractures will initiate. For mode-I (ψ = 0°) the bands are

relatively insensitive to m owing to the bimodal stress distribution; however, for mode-II (ψ = 90°) the failure are more tightly grouped for large m.

Figure 4.8: Average distance of fracture initiation for statistical fracture model for mode-I, (ψ=0°) and mixed-mode (ψ=45°) case. Average fracture initiation distances are close to the cutoff dimension, ρ, for high m and are weakly affected by R. For low m, $\bar{r}$ is weakly affected by ρ can be as large as $R/2$.

Figure 4.9: Mode-I fracture toughness for an infinite body FGM with $\sigma_0(x)$ based on statistical fracture model. Results are displayed for two sets of limits of integration, ρ and R, with (a) $\rho = R/10^5$ and (b) $\rho = R/10^3$ and m from 2 to 13.

Figure 4.10: Mode-I fracture toughness for an infinite body FGM with E(x) based on statistical fracture model. Stress field is a one-term modification of the homogeneous stress field (Eq. 4.2). Results are displayed for two sets of limits of integration, ρ and R, with (a) $\rho = R/10^5$ and (b) $\rho = R/10^3$ and m from 2 to 8.

Figure 4.11: Average initiation angle ϕ, for an infinite body FGM with $\sigma_0(y)$ based on statistical fracture model. Results are displayed for two sets of limits of integration, ρ and R, with (a) $\rho = R/10^5$ and (b) $\rho = R/10^3$ and m from 2 to 15.

Figure 4.12: K_Φ for infinite body with the modified K-field (Eq. 4.2) and a gradient in Young's modulus perpendicular to the crack plane, E(y). The near-tip was in pure mode-I loading, but the modulus gradient induces an asymmetry in stresses. The elevated stresses in a region y>0 for b>0 cause the failure probability to be increased for a given K.

Figure 4.13: Average initiation angle ϕ, for an infinite body FGM with $E(y)$ based on statistical fracture model. Stress field is a one-term modification of the homogeneous stress field (Eq. 4.2). Results are displayed for two sets of limits of integration, ρ and R, with $\rho = R/10^5$ (solid lines) and $\rho = R/10^3$ (dashed lines) and m from 2 to 15.

Figure 4.14: Variation of the weighted local failure probability $p^*(\sigma)$ for an infinite body with $\sigma_0(x)$ for m=3 and m=11. Gradient parameters of $b{\cdot}2a$={0,5,10,20} are displayed. The tendency for fracture to initiate away from the crack tip is apparent as $p^*(\sigma)$ can reach a local maximum greater than the value of p^* at ρ.

Figure 4.15: Stress intensity factors, K_I and K_{II} for the SE(T) fracture mechanics sample for modulus gradients $E(x)$ and $E(y)$ (solid lines). The gradient

in the y-direction results in a shearing of the crack tip, such that that the tensile geometry results in a mixed-mode loading with the phase angle increasing in magnitude for increasing gradient (dashed line).

Figure 4.16: Deviation of yy-stresses ahead of the crack tip from classical K-field for a single-edge notched tension, SE(T), specimen with $E(x)$ gradient for cases with b(2a)=-20,0,20. Normalized moduli $E(x)$ are also plotted for comparison. Comparing these shows the approximation in Eq. 4.2 would appear to improve the description of the near-tip stresses, but underestimates their magnitude.

Figure 4.17: Effect of variable strength $\sigma_0(x)$ on the fracture toughness of a single-edge notched tension, SE(T), specimen. Two near-tip cutoff regions are utilized, $\rho = a/10^5$ (a) and $a/10^3$ (b).

Figure 4.18: Effect of variable modulus $E(x)$ on the normalized fracture toughness of a single-edge notched tension, SE(T), specimen. Two near-tip cutoff regions are utilized, $\rho=a/10^5$ (a) and $a/10^3$ (b).

Figure 4.19: Average initiation angle for the case of pure Mode-I loading and $\sigma_0(y)$ in a single-edge notched tension, SE(T), specimen. Strength gradient skews average location of fracture such that non-zero initiation angle is preferred Two near-tip cutoff regions are utilized, $\rho=a/10^5$ (a) and $a/10^3$ (b).

Figure 4.20: Average initiation angle for a material with modulus gradient $E(y)$ in a (a) single-edge notched tension, SE(T), and (b) middle-cracked tension, M(T), specimen geometry. Results using for near-tip cutoff radius $\rho=a/10^5$ (solid lines) and $a/10^3$(dashed lines) and for Weibull moduli m={2-7,9,11,13,15} are displayed. The gradient induces a positive phase angle as seen in Fig. 4.15, but the gradient-induced stresses cause a positive initiation angle for very low m. The substantial gradient-induced trends are seen in both the SE(T) and M(T) sample geometries.

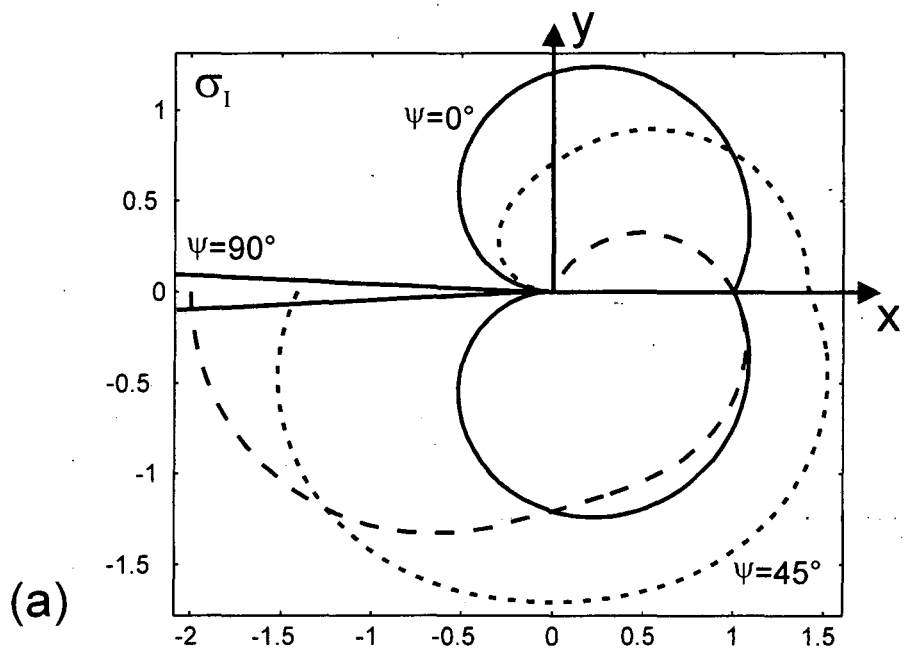

(a)

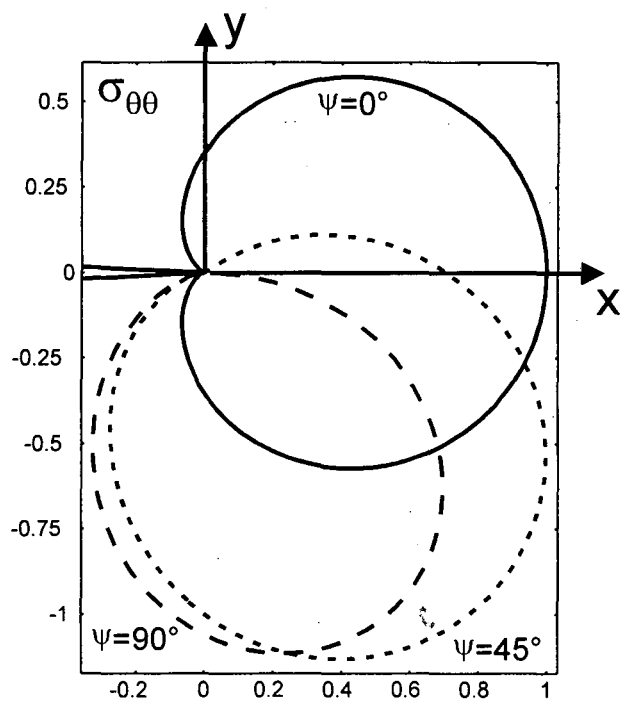

(b)

Figure 4.1: Isostress contours of for (a) maximum principal stress σ_I and (b) hoop stress $\sigma_{\theta\theta}$ for loading phase angles ψ=0°, 45°, 90°. Shapes of contours indicate relative levels of stress, with larger r corresponding to higher larger stress at that θ.

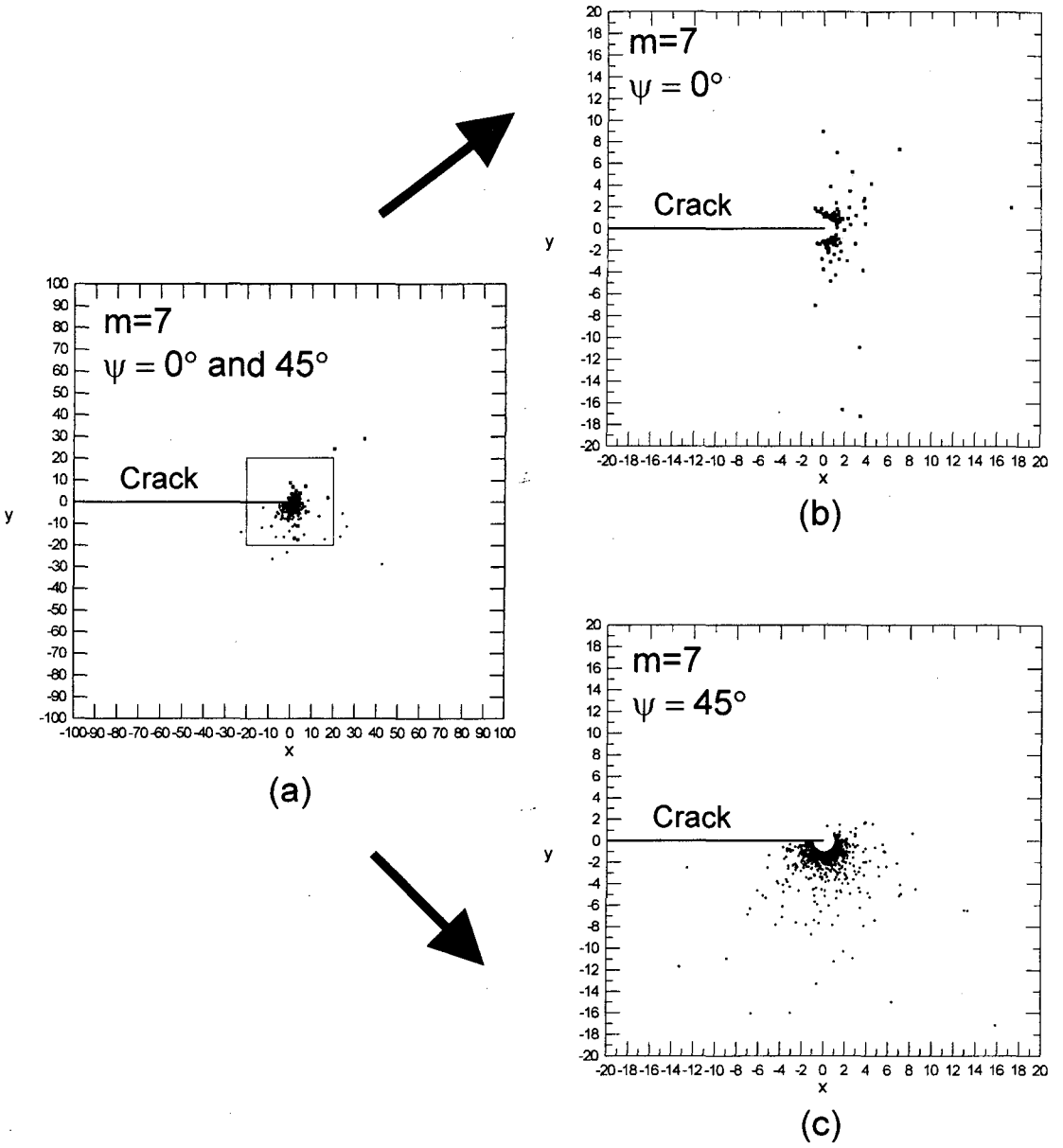

Figure 4.2: Results of Monte Carlo simulations for a brittle material in the neighborhood of a sharp elastic crack. Mode-I, (ψ=0°) and mixed-mode (ψ=45°) cases are displayed for Weibull modulus, m=7. Points around the crack tip at (0,0) indicate the location of a simulated fracture initiation. Strong skewing toward in the negative y-direction is evident for the mixed-mode case, which indicates that the crack will tend to grow downward. The increased number of fracture initiations in the mixed-mode case loaded to the same $|K|$ indicate a decreased fracture toughness.

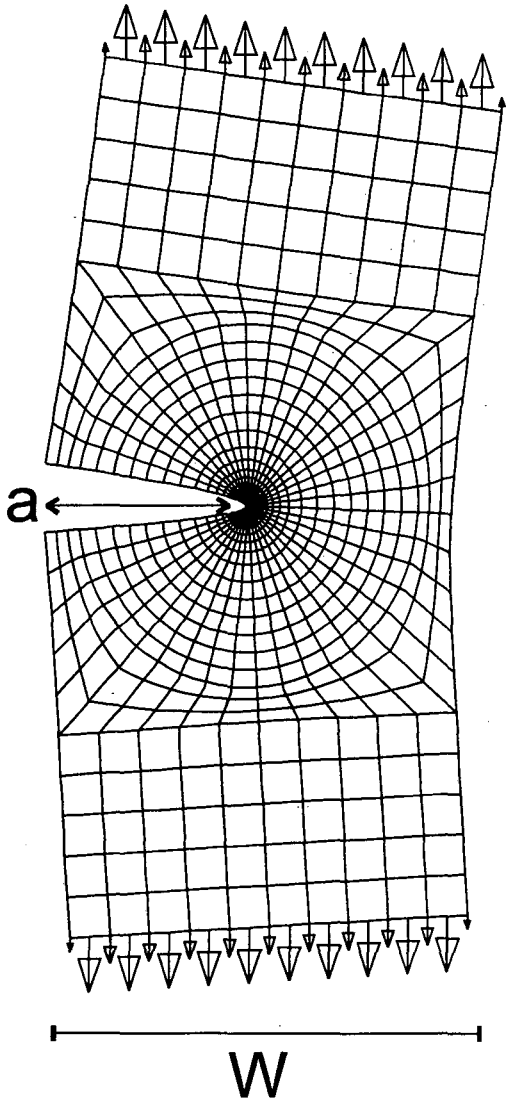

Figure 4.3: Finite element mesh used in study of SE(T) fracture mechanics specimen. A high degree of refinement was used, with a focused ring of element surrounding the crack tip. A similar mesh with different boundary conditions was used to study the MC(T) sample.

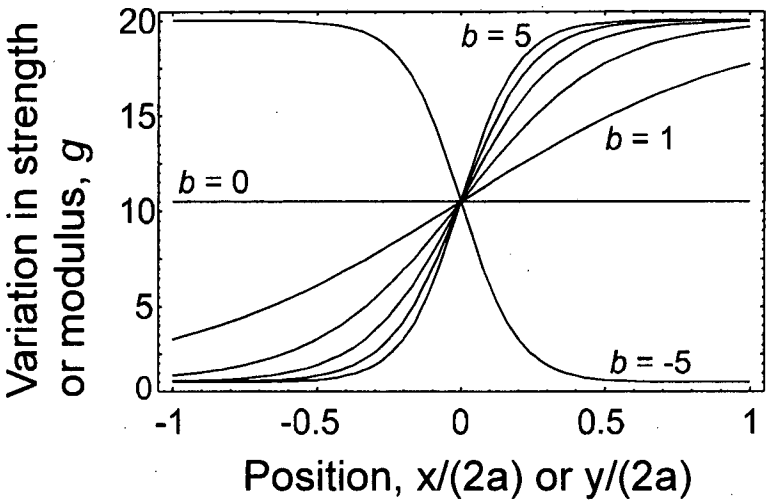

Figure 4.4: Sigmoidal gradient modeled. This shape allowed for an arbitrarily steep gradient at the crack tip, determined by the parameter b. The total range of variation within the sample being is constant, with $g(\infty)/g(-\infty) = 20$.

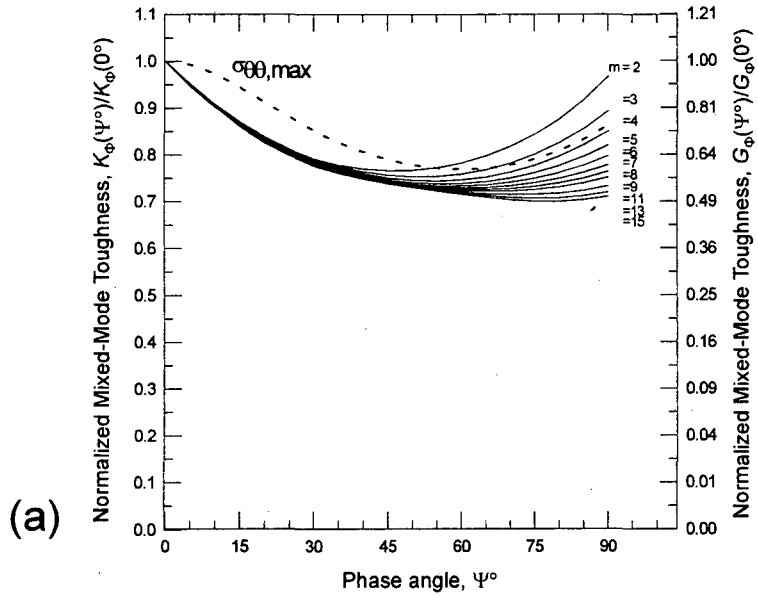

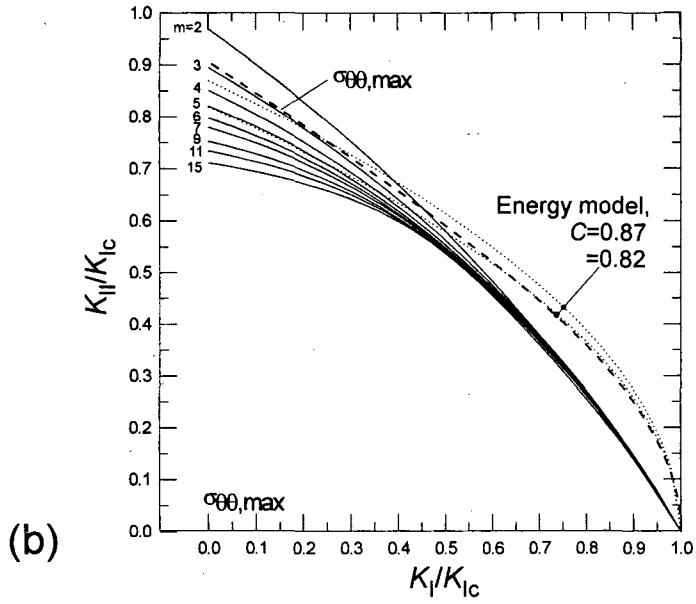

Figure 4.5: (a) Prediction for the mixed-mode fracture toughness for an infinite body of a homogeneous material based on statistical fracture model for various values of Weibull modulus (solid lines) compared to the deterministic prediction based on critical hoop stress (dashed line). (b) Prediction for the mixed-mode fracture toughness envelope for the statistical model compared to the empirical envelope of Palaniswamy and Knauss (1978) for fitting parameter C=0.82 and 0.87.

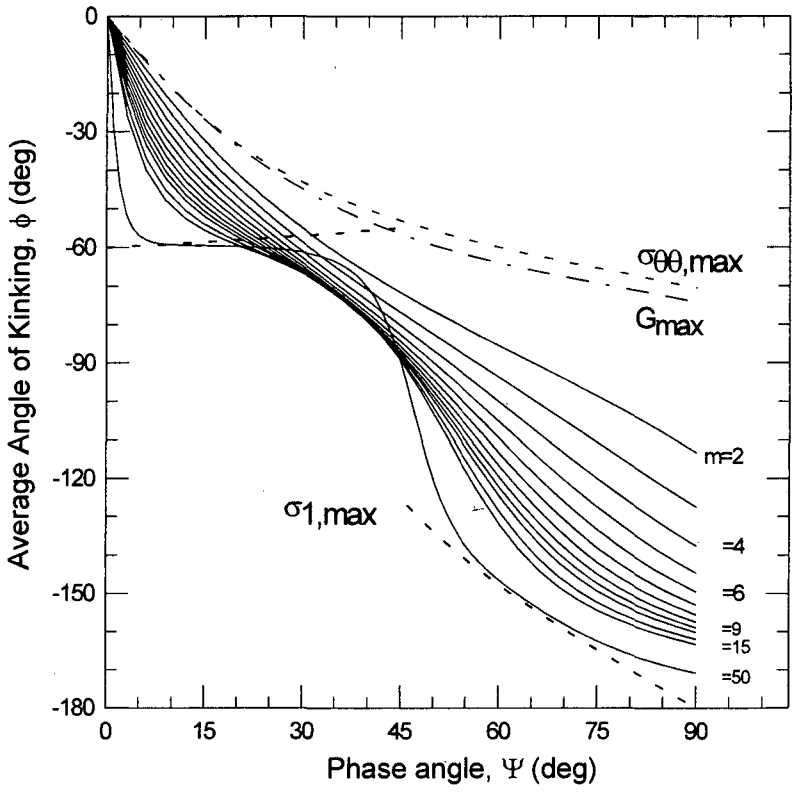

Figure 4.6: Average initiation angle for mixed-mode fracture loading for an infinite body of a homogeneous material based on statistical fracture model. Included for comparison are the angles of maximum hoop stress and maximum energy release rate (dashed lines).

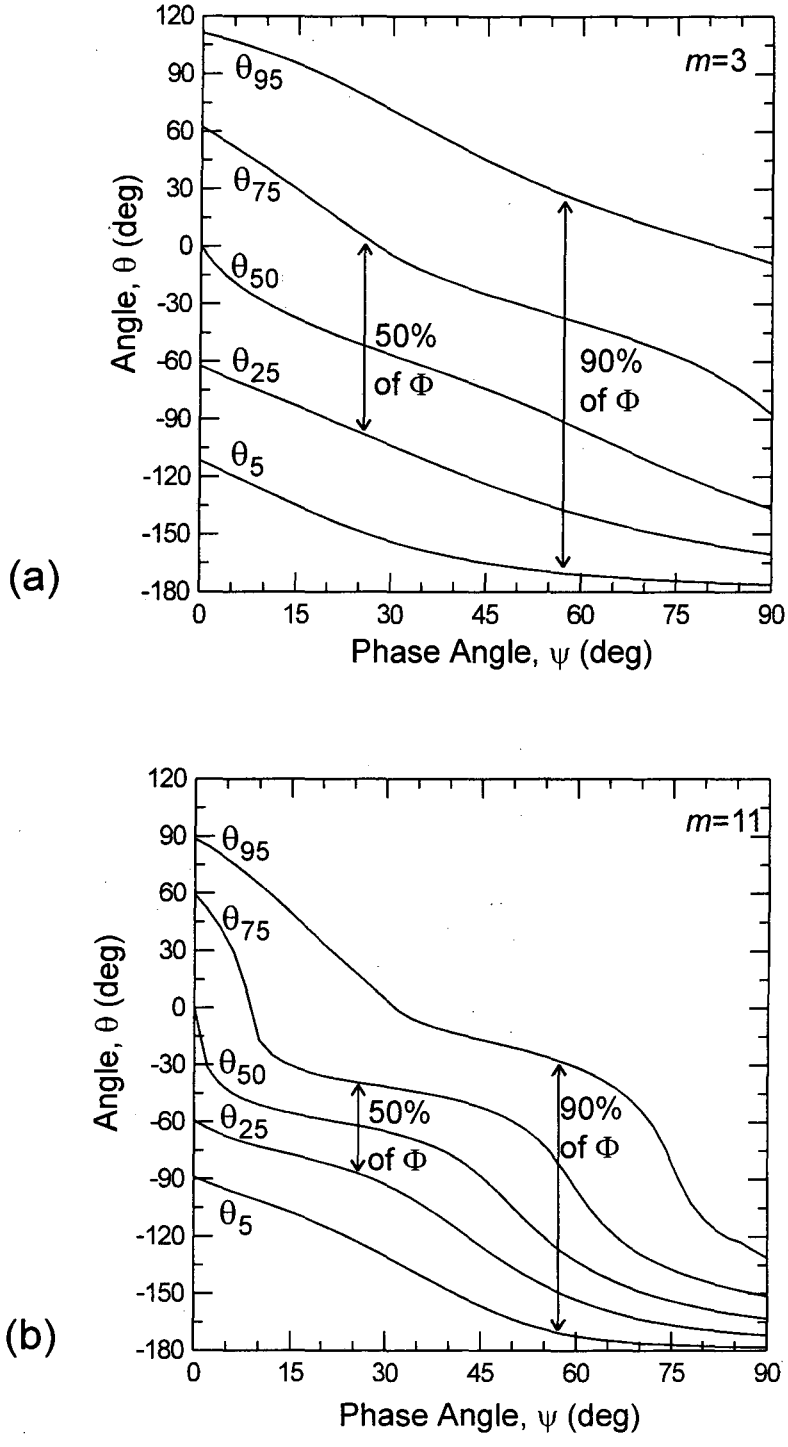

Figure 4.7: Contours of cumulative probability for homogenous material with mixed-mode loading for (a) m=3 and (b) m=11. The median angle, θ_{50}, bisects the total failure probability for the material between $-\pi$ and π. The bands about the median indicate the angles where 50% and 90% of the fractures will initiate. For mode-I ($\psi = 0°$) the bands are relatively insensitive to m owing to the bimodal stress distribution; however, for mode-II ($\psi = 90°$) the failure are more tightly grouped for large m.

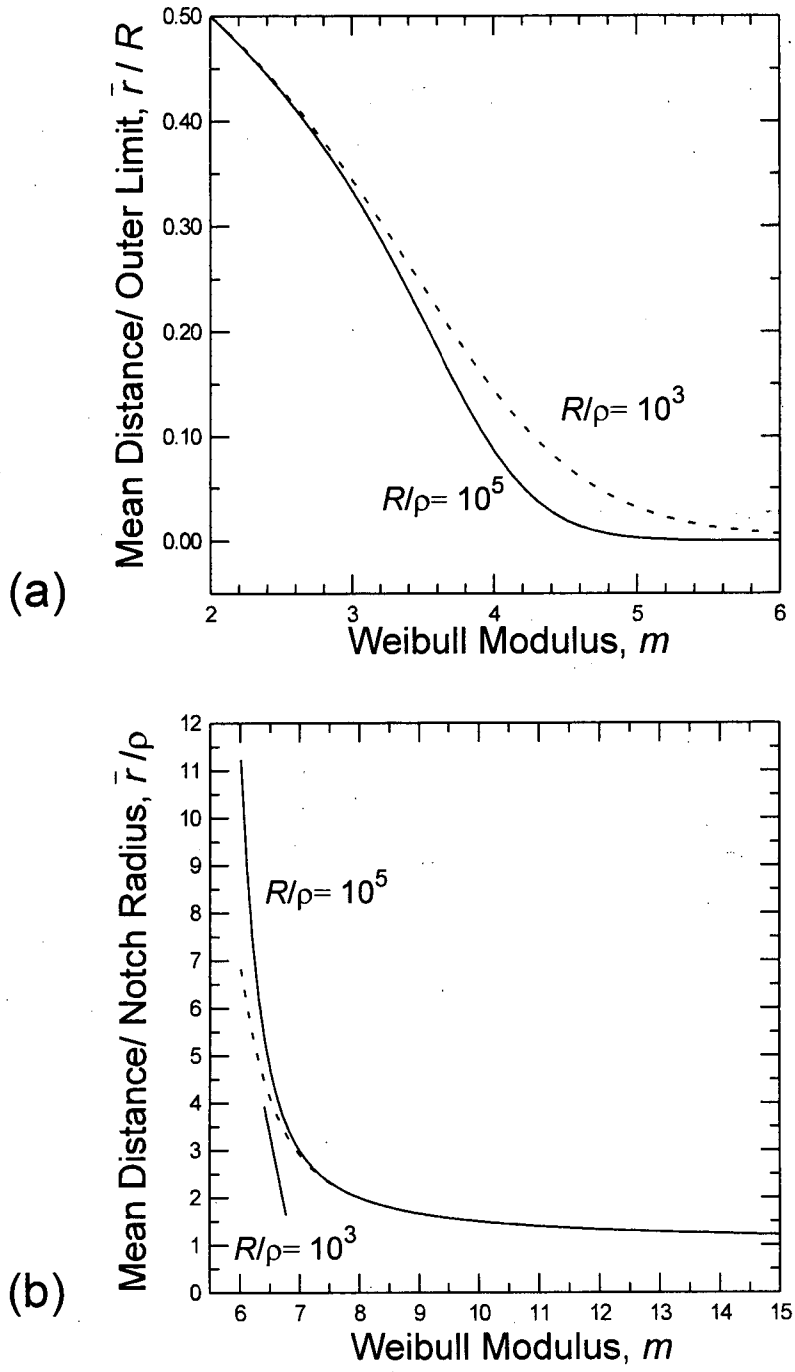

Figure 4.8: Average distance of fracture initiation for statistical fracture model for mode-I, (ψ=0°) and mixed-mode (ψ=45°) case. Average fracture initiation distances are close to the cutoff dimension, ρ, for high m and are weakly affected by R. For low m, $\bar{r}$ is weakly affected by ρ can be as large as $R/2$.

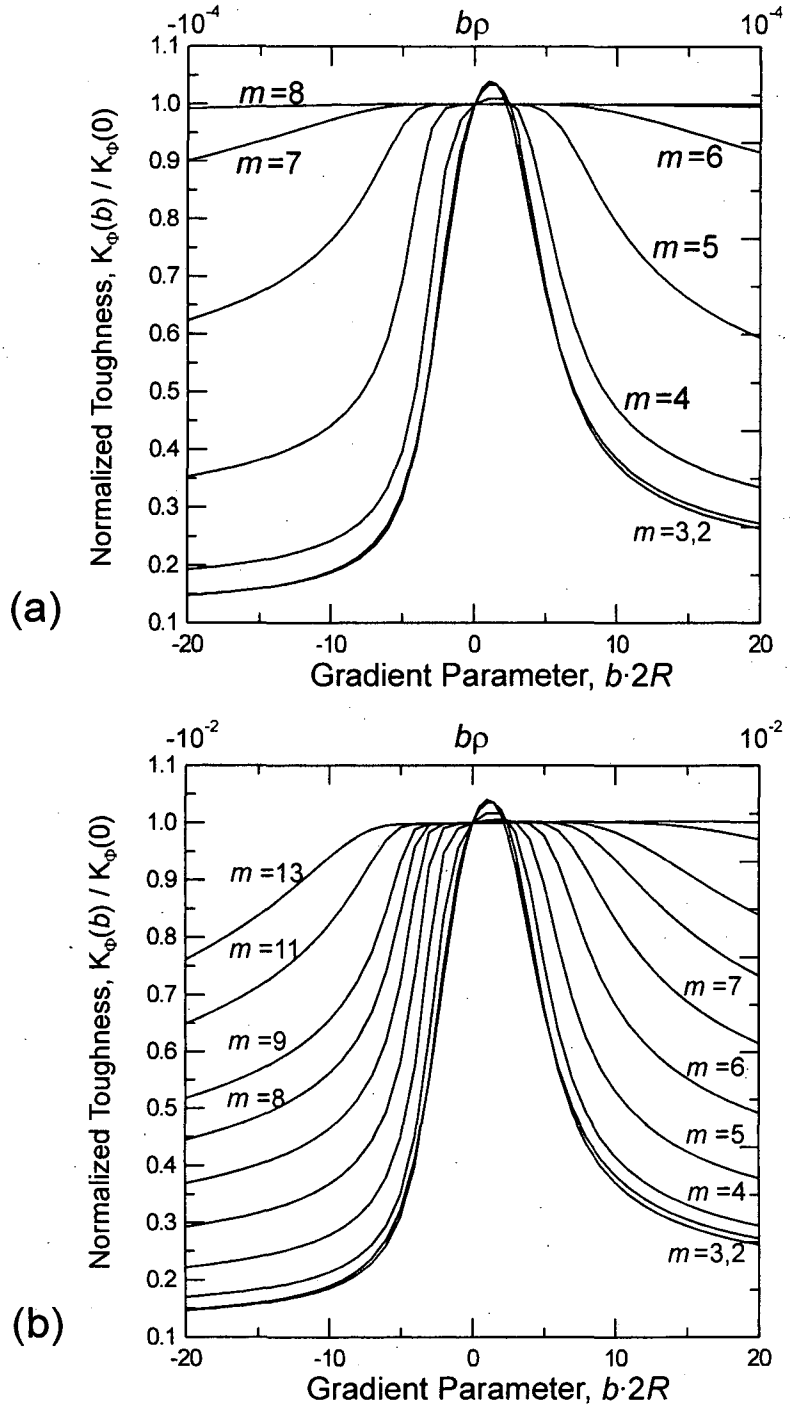

Figure 4.9: Mode-I fracture toughness for an infinite body FGM with $\sigma_0(x)$ based on statistical fracture model. Results are displayed for two sets of limits of integration, ρ and R, with (a) $\rho = R/10^5$ and (b) $\rho = R/10^3$ and m from 2 to 13.

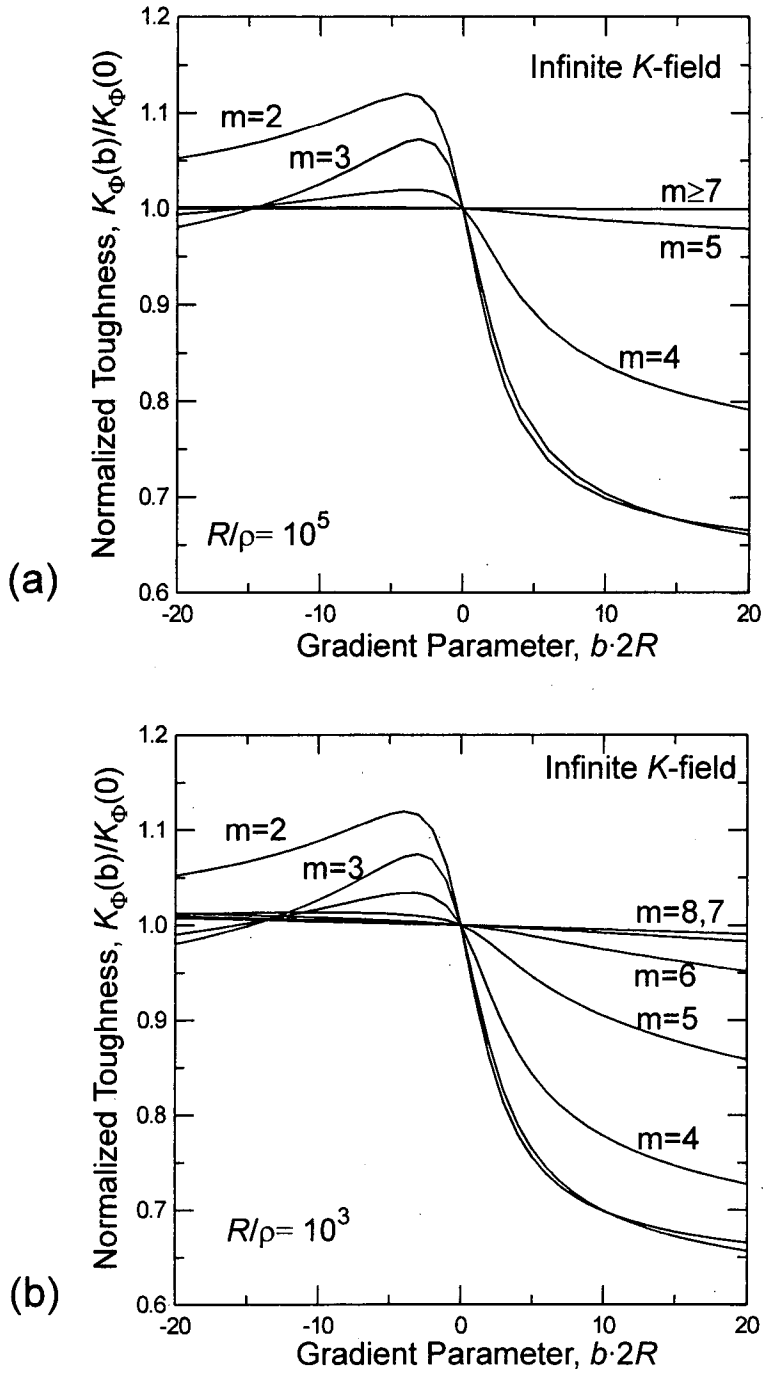

Figure 4.10: Mode-I fracture toughness for an infinite body FGM with $E(x)$ based on statistical fracture model. Stress field is a one-term modification of the homogeneous stress field (Eq. 2). Results are displayed for two sets of limits of integration, ρ and R, with (a) $\rho = R/10^5$ and (b) $\rho = R/10^3$ and m from 2 to 8.

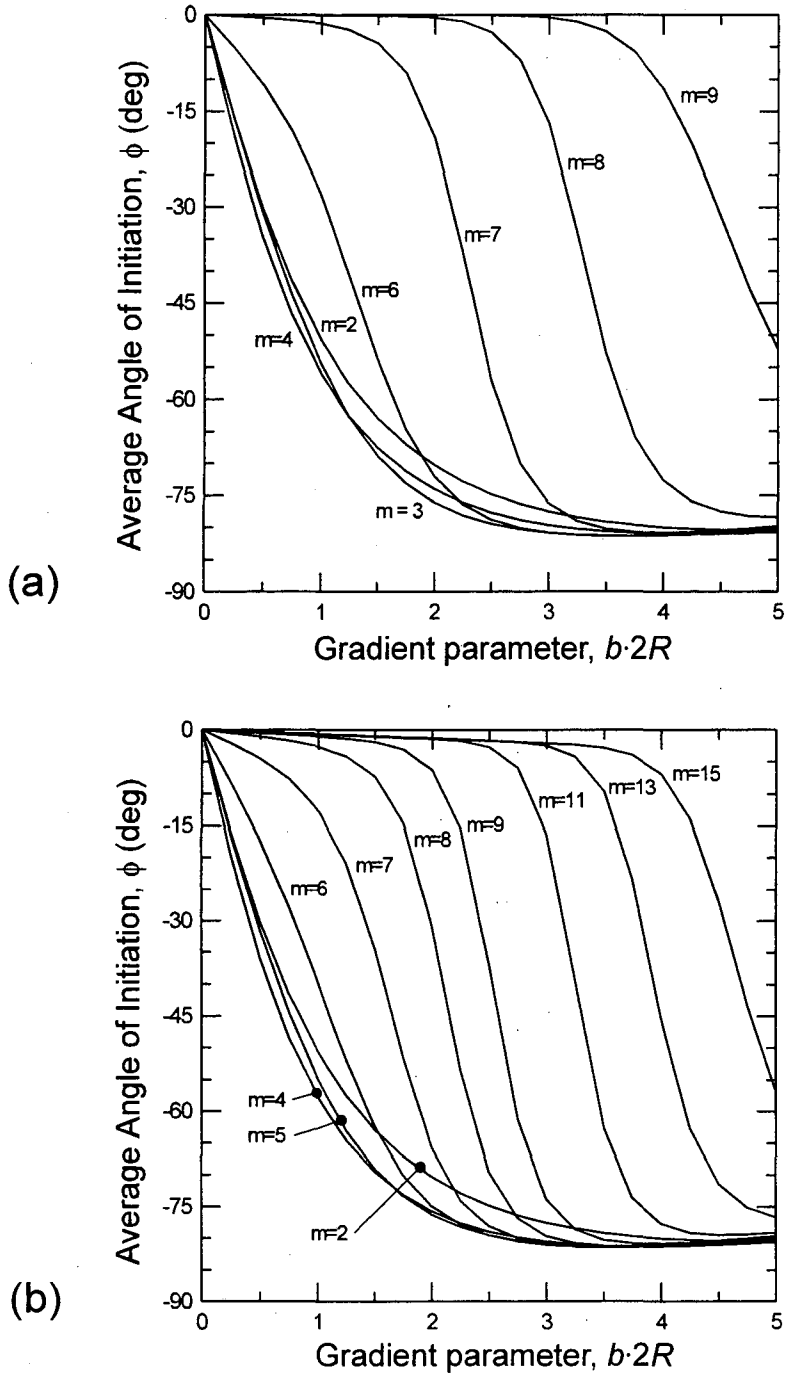

Figure 4.11: Average initiation angle ϕ, for an infinite body FGM with $\sigma_o(y)$ based on statistical fracture model. Results are displayed for two sets of limits of integration, ρ and R, with (a) $\rho = R/10^5$ and (b) $\rho = R/10^3$ and m from 2 to 15.

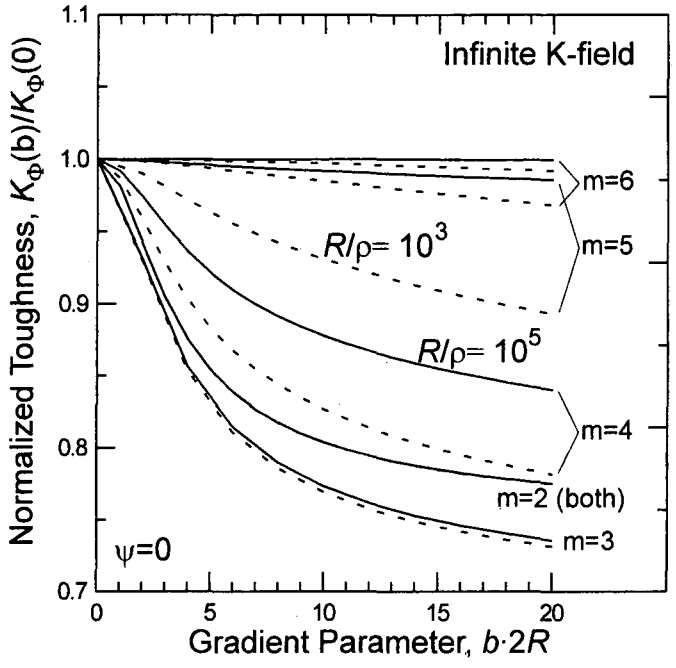

Figure 4.12: K_Φ for infinite body with the modified K-field (Eq. 2) and a gradient in Young's modulus perpendicular to the crack plane, E(y). The near-tip was in pure mode-I loading, but the modulus gradient induces an asymmetry in stresses. The elevated stresses in a region $y>0$ for $b>0$ cause the failure probability to be increased for a given K.

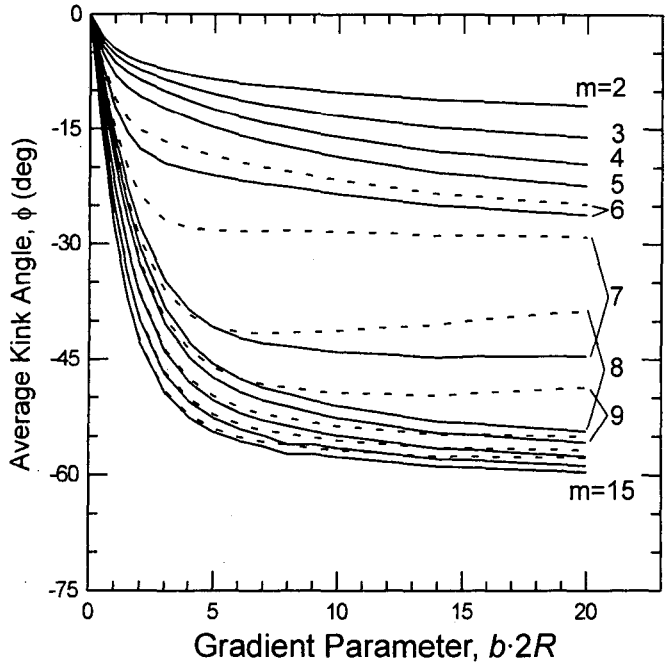

Figure 4.13: Average initiation angle ϕ, for an infinite body FGM with $E(y)$ based on statistical fracture model. Stress field is a one-term modification of the homogeneous stress field (Eq. 2). Results are displayed for two sets of limits of integration, ρ and R, with $\rho = R/10^5$ (solid lines) and $\rho = R/10^3$ (dashed lines) and m from 2 to 15.

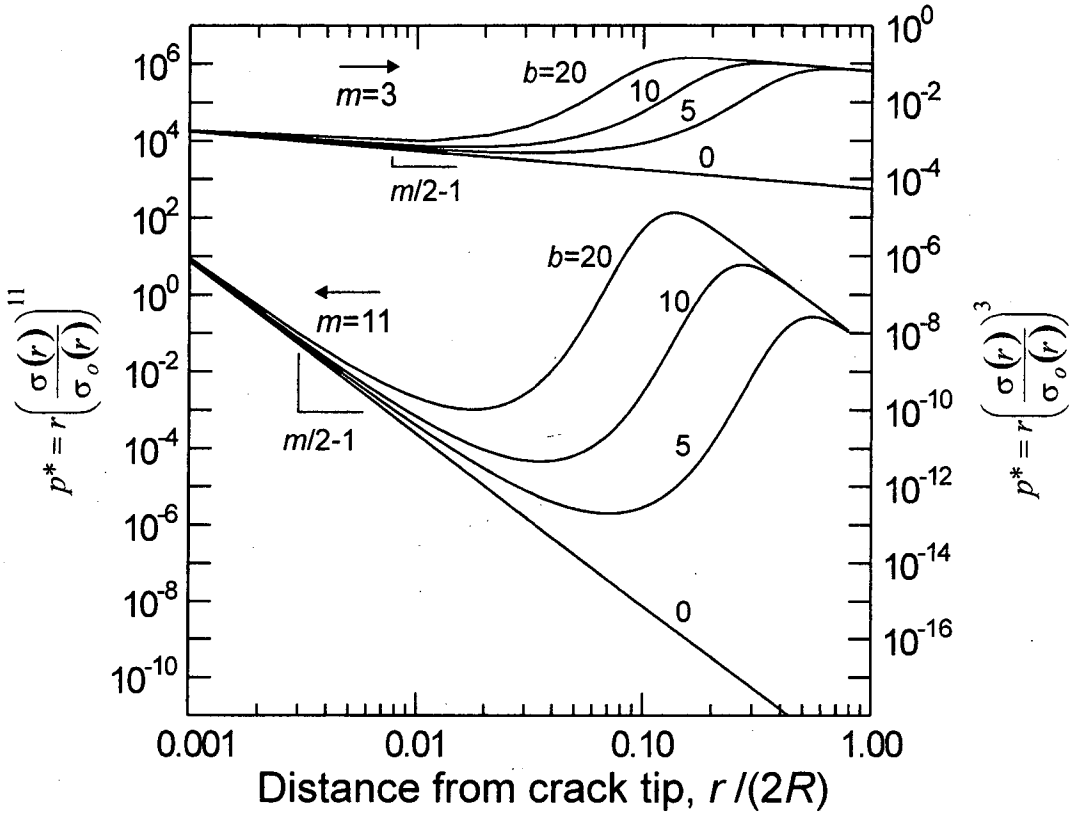

Figure 4.14: Variation of the weighted local failure probability $p^*(\sigma)$ for an infinite body with $\sigma_o(x)$ for m=3 and m=11. Gradient parameters of $b{\cdot}2a$={0,5,10,20} are displayed. The tendency for fracture to initiate away from the crack tip is apparent as $p^*(\sigma)$ can reach a local maximum greater than the value of p^* at ρ.

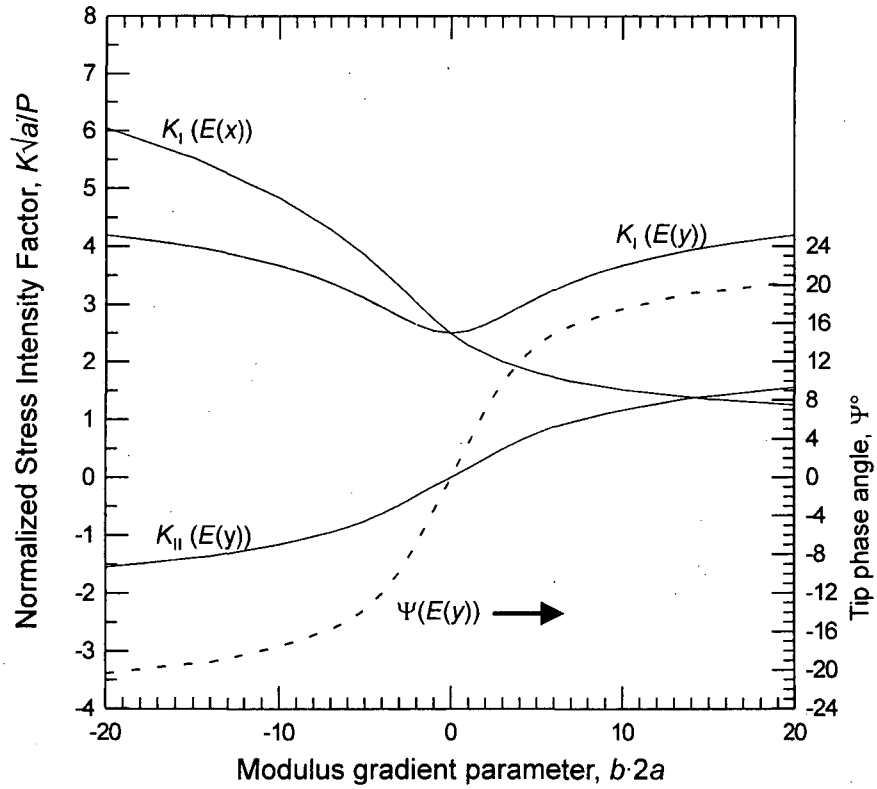

Figure 4.15: Stress intensity factors, K_I and K_{II} for the SE(T) fracture mechanics sample for modulus gradients $E(x)$ and $E(y)$ (solid lines). The gradient in the y-direction results in a shearing of the crack tip, such that that the tensile geometry results in a mixed-mode loading with the phase angle increasing in magnitude for increasing gradient (dashed line).

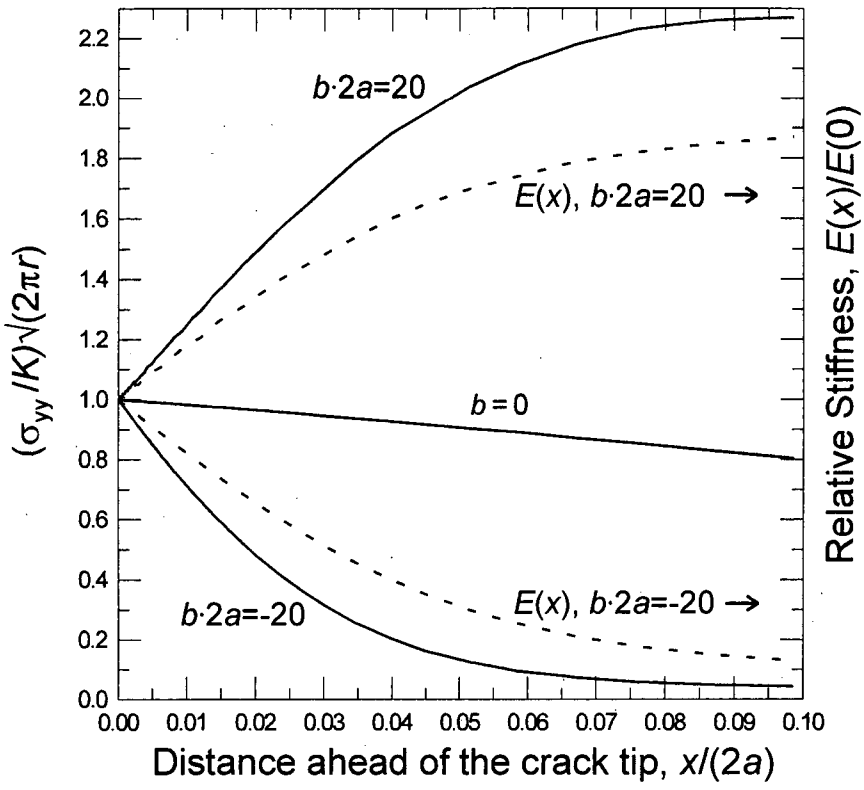

Figure 4.16: Deviation of *yy*-stresses ahead of the crack tip from classical *K*-field for a single-edge notched tension, SE(T), specimen with $E(x)$ gradient for cases with b(2a)=-20,0,20. Normalized moduli $E(x)$ are also plotted for comparison. Comparing these shows the approximation in Eq. 4.2 would appear to improve the description of the near-tip stresses, but underestimates their magnitude.

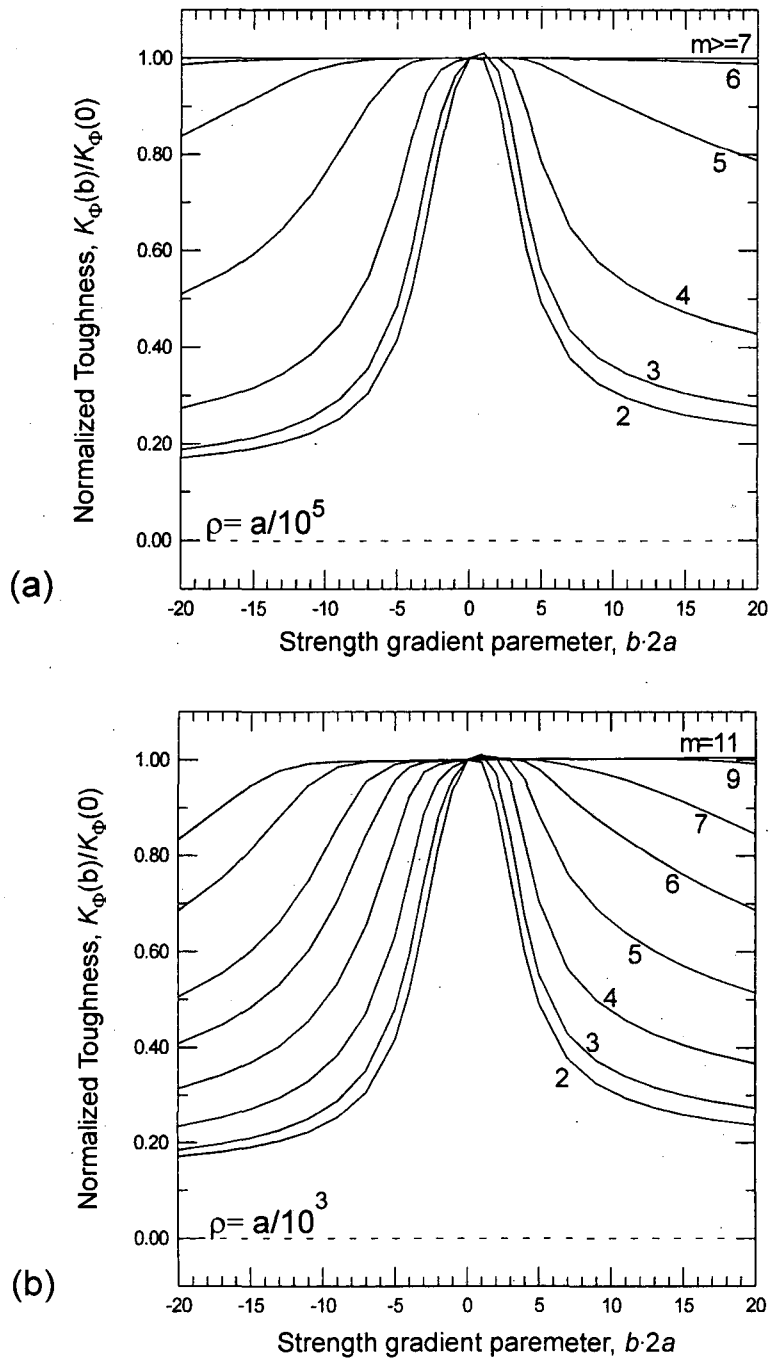

Figure 4.17: Effect of variable strength $\sigma_o(x)$ on the fracture toughness of a single-edge notched tension, SE(T), specimen. Two near-tip cutoff regions are utilized, $\rho = a/10^5$ (a) and $a/10^3$ (b).

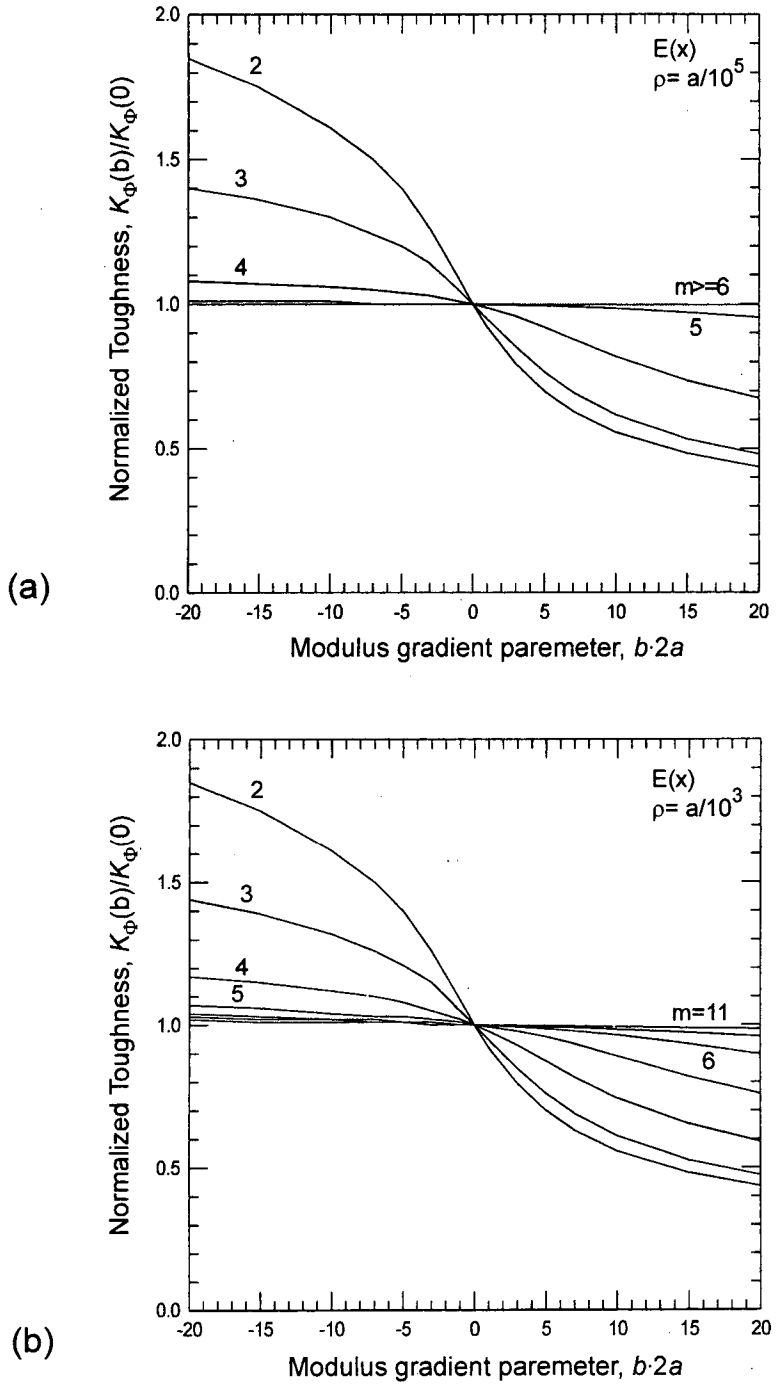

Figure 4.18: Effect of variable modulus $E(x)$ on the normalized fracture toughness of a single-edge notched tension, SE(T), specimen. Two near-tip cutoff regions are utilized, $\rho=a/10^5$ (a) and $a/10^3$ (b).

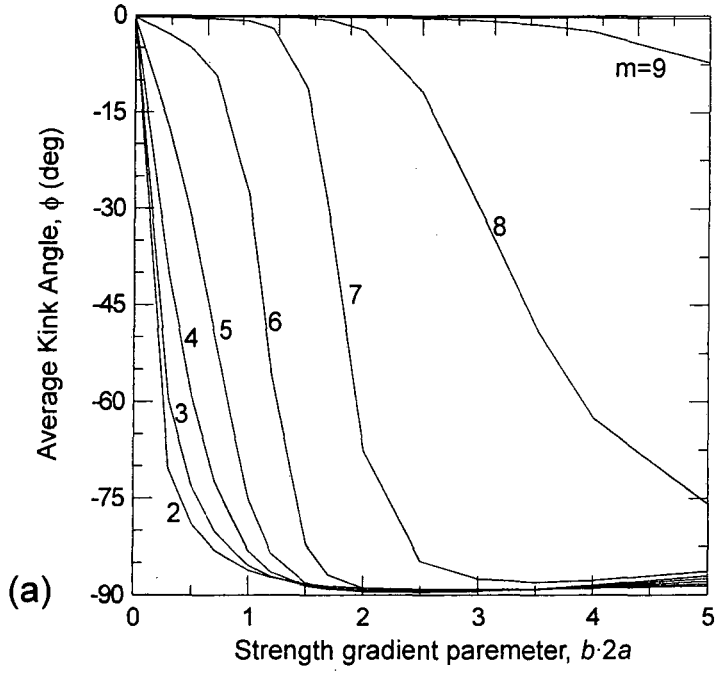

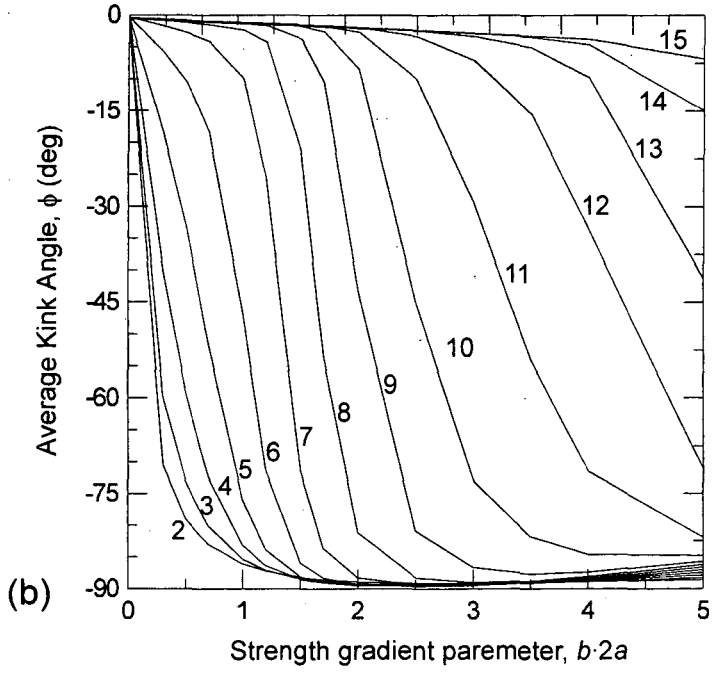

Figure 4.19: Average initiation angle for the case of pure Mode-I loading and $\sigma_o(y)$ in a single-edge notched tension, SE(T), specimen. Strength gradient skews average location of fracture such that non-zero initiation angle is preferred Two near-tip cutoff regions are utilized, $\rho=a/10^5$ (a) and $a/10^3$ (b).

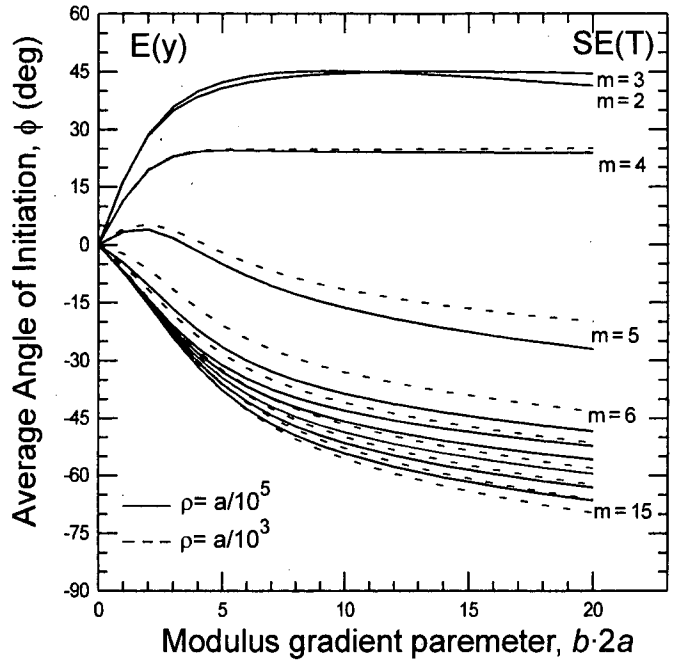

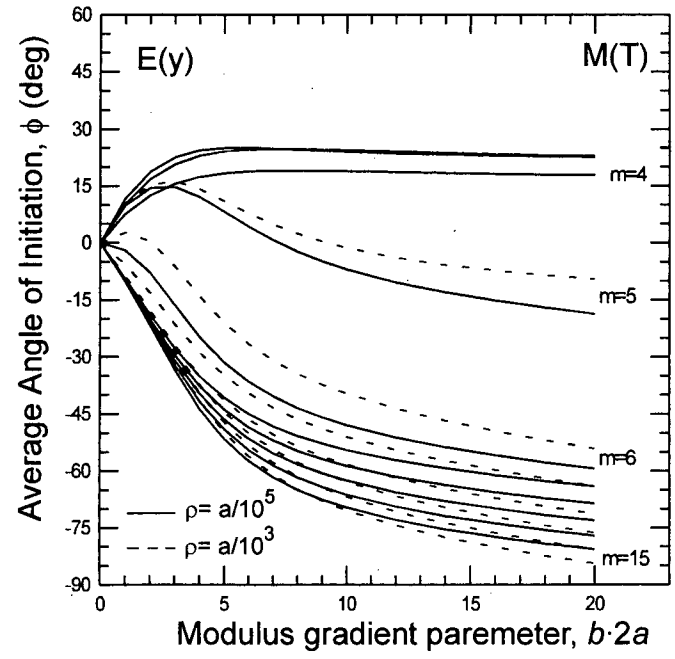

Figure 4.20: Average initiation angle for a material with modulus gradient $E(y)$ in a (a) single-edge notched tension, SE(T), and (b) middle-cracked tension, M(T), specimen geometry. Results using for near-tip cutoff radius $\rho=a/10^5$ (solid lines) and $a/10^3$(dashed lines) and for Weibull moduli m={2-7,9,11,13,15} are displayed. The gradient induces a positive phase angle as seen in Fig. 4.15, but the gradient-induced stresses cause a positive initiation angle for very low m. The substantial gradient-induced trends are seen in both the SE(T) and M(T) sample geometries.

Chapter 5: Finite Crack Kinking in Functionally Graded Materials

5.1 Introduction

For cracks loaded in tension and shear, the direction of crack growth is an important aspect of fracture behavior. For FGMs with variable modulus, mixed-mode cracks are common. A thorough analysis of the kinking problem for FGMs will incorporate both traditional fracture mechanics parameters and higher-order terms in the stress field, which will depend on the gradient. This will allow the calculation of the optimum crack path given the loading and material parameters.

5.2 Crack Kinking in Homogeneous Materials

Historically, fracture mechanics research first sought to determine the conditions for stability of straight cracks extending in their own plane. For mixed-mode loading, this is often not the mechanically or energetically most favorable path. In fact, a variety of methodologies have been employed to determine the direction of crack growth under mixed-mode (tensile and shear) loading in homogeneous and layered materials.

The first calculations are those of Erdogan and Sih (1963) who used two simple criteria to determine the kink angle under in-plane loading:

1) that the growth should extend in a radial direction from the tip of the existing crack, and

2) the crack extension starts in the plane perpendicular to the direction of greatest normal stress.

This implies that the direction of crack growth is determined by the angle of maximum $\sigma_{\theta\theta}$ (hoop stress) near the tip of the preexisting (unkinked) crack; using the Williams (1957) K-field solution the optimal kink angle ω can be determined by

$$K_1 Sin(\omega) - K_2(3Cos(\omega) - 1) = 0\,. \qquad (5.1)$$

This somewhat simplistic formulation (referred to as the $\sigma_{\theta\theta,max}$ criteria) tends to under-predict experimental results (Finnie and Saith, 1973). Subsequent analysis (Cotterell, 1966) shows, for small kink angles, that this direction coincides with the direction of maximum energy release, G_{max}.

The analysis of the problem was advanced to include the geometry of a small off-plane extension (kink) (Fig. 5.1). The stress intensity state (K_I, K_{II}) of a kink can be calculated in terms of the stress field surrounding the tip of the original crack (with stress intensities K_1, K_2). Using Erdogan and Sih's (1957) analysis, the subsequent direction of crack growth can be determined. Utilizing the power series description of the each component of stress near the unkinked crack,

$$\sigma = a_1 f_1(\theta) r^{-1/2} + a_2 f_2(\theta) + a_3 f_3(\theta) r^{1/2} + a_4 f_4(\theta) r^{3/2} + O(r^{5/2}), \qquad (5.2)$$

the role of the coefficients (a_i) describing the stress state near the crack in determining the tendency of a kink to grow increasingly away from y=0 (or to return to the original crack plane) was established (Cotterell, 1966).

The first term, a_1, is the stress intensity factor, $K_1/\sqrt{2\pi}$, which is preeminent in most fracture mechanics analysis. The second term, a_2, represents the strength of a constant σ_{xx} stress, and is usually referred to as the T-stress. It has been found to have a

major effect on ductile fracture behavior (Du and Handcock, 1991) as well as in the determination of the extent of kinking.

The T-stress is, in general, independent of the stress intensity factor; that is, two cracked bodies can have the same K_1, K_2, but different T's. For a compressive (negative) value of T, the crack path is stabilized. For a positive (tensile) T-stress, the path is destabilized; that is, for a mode-I crack, if a small random positive kink is formed along ω, subsequent crack growth will occur at an angle greater than ω. Similar analysis was performed on curved cracks (Cotterell and Rice, 1980). Both are restricted approximations that are only accurate to the first order of ω.

For analysis of finite angled cracks, the kink angle corresponding to the G_{max} criteria was determined for both sharp interfaces and homogeneous materials by He and Hutchinson (1989) and He *et al.* (1991). Here the stress intensity factors for a kink are calculated in the form

$$K_I = c_I K_1 + d_I K_2 + b_I T\sqrt{\Delta a} \tag{5.3a}$$

$$K_{II} = c_{II} K_1 + d_{II} K_2 + b_{II} T\sqrt{\Delta a} \tag{5.3b}$$

where K_1 and K_2 are the stress intensity factors of the unkinked crack tip (Fig 5.1). For homogeneous materials, the coefficients $c_{I,II}$ and $d_{I,II}$ are also given in the earlier work of Hayashi and Nemat-Nasser (1981). The strain energy release rate of the kink can subsequently be calculated via $G = (K_I^2 + K_{II}^2) / E'$. Using the tip state, the angle for which $K_{II}(\omega)=0$ or $G(\omega)$ is the maximum ($G = \max(G(\omega), \forall\ \omega{:}-\pi<\omega<\pi)$ can be calculated from K_1, K_2, and T.

A comparison of the stress intensity and energy criteria can be found in Suo and Hutchinson (1991) (Fig 5.2); the two methodologies agree at $\psi=0°$ (pure tension, $K_{II}=0$)

and diverge by about 3° at Ψ=90° (pure shear, K_I=0). Cotterell (1965) showed the equivalence of the direction of maximum hoop stress prediction with that of maximum energy release for small ω. The agreement for large ω is surprisingly good. Experimental evidence clearly shows the advantage of the finite ω criteria over $\omega_{\sigma\theta\theta,max}$ (Finnie and Saith, 1973), but the scatter is sufficiently large that discriminating between the K_{II}=0 and G_{max} criteria is difficult.

The K_{II}=0 criteria can be understood from a symmetry argument. For brittle materials, failure is associated with normal (rather than shear) stresses. Mixed-mode cracks, by definition, then have a mechanical driving force to grow off their plane. Therefore, the kink in pure mode-I is the only stable path. However, for finite-length straight cracks, this criteria has less appeal, as it focuses solely on the conditions near the tip of the kink. The G_{max} formulation of the problem suppresses any influence of the mechanism of crack advance, but instead appeals to the variation principle for linear elasticity.

Palaniswamy and Knauss (1978) used Betti's reciprocal theorem to explain the close agreement of the two methodologies. The energy release, G, rate can be written as

$$G(\omega) = \lim_{\Delta a \to 0} \frac{1}{2\Delta a} \int_0^{\Delta a} \left(\sigma'_{\theta\theta}(r,\omega)\delta''_{\theta}(r,\omega) + \sigma'_{r\theta}(r,\omega)\delta''_{r}(r,\omega)\right) dr \qquad (5.4)$$

where $()'$ denotes the unkinked solution (Figure 5.1a), $()''$ the kinked (Figure 5.1b), and δ the opening displacements across the kink faces. The G_{max} criteria is satisfied by the combined effect of both of the integrals, where as the K_{II}=0 criteria infers restrictions on terms in the second.

5.3 Crack Kinking in FGMs

FGMs, like discrete elastic interfaces, are inherently prone to developing mixed-mode cracks. Nevertheless, few studies on crack kinking in FGMs have been performed. Lee and Erdogan (1995) calculated the effect of modulus gradient on the angle of maximum hoop stress near the free edge of a graded joint and discussed the implications on the direction of fracture initiation. The coincidence of the asymptotic stress solution of the crack problem with the homogeneous William's solution (1957) motivated Gu and Asaro (1997) to apply the analysis of Cotterell and Rice (1980) to various geometries with modulus gradients. This analysis inherits the approximation for suitably small kink angles. Furthermore, it assumes no gradient effect on the kinking behavior besides that which is characterized in the near-tip phase angle ψ. The direction of crack growth will vary from this prediction for any non-zero length. The authors give no guidance as to the range over which this analysis will be accurate.

5.4 Problem Formulation

5.4.1 Kinked crack geometry

To assess the dependence of the optimal kink angle on kink length, a finite geometry with various combinations of kink angle and length was analyzed. Ideally, the far-field boundary conditions should be set such that the results are the most general. For instance, in studying the near-crack behavior of a nonlinear elastic material Geubelle and Knauss (1995) employed a boundary layer methodology where the far-field boundary conditions were assigned to be those of the linear elastic crack solution. The body was sufficiently large that the distance to the boundary did not effect the outcome of the

solution. This is the familiar small-scale yielding condition. Such results could be applied to any body large enough that it could be expected to contain a sufficiently large linear K-dominant zone.

Such a methodology presupposes a nested set of singular solutions, namely that a nonlinear field is bounded by linear K-field. No such set of solutions is known for an FGM. However, as shown in Chapter 4, the gradient-induced terms should be important in the neighborhood near the crack tip such that $r \sim 1/b$ (Jin and Batra, 1996). For a homogeneous linear body, the K-dominant region should scale with about 1/10 to 1/100 of the smallest in-plane dimension. Therefore, for $r \sim 1/b \ll r_K^{hom}$ the stress state should be characterized by crack-tip and gradient terms. For $r < r_K^{fgm} \ll 1/b$ the stress state is describable by K_1 and K_2 alone.

The geometry analyzed here is a square sheet with a centered crack with length $2a$ (Fig. 5.3). The outer dimensions are much greater than the crack length, with W/a=20. Therefore, the details of the size and shape of the boundary are of minimal consequence to the near-tip conditions[1]. The tip and kink regions are refined (Fig. 5.4) to accurately model the stress singularities. Solutions were obtained with the finite element package FEAP (Zienkiewicz and Taylor, 1989) as described in Section 2.6. Meshes consisted of 10,000-13,000 quadrilateral plane-strain elements.

The edges of the sheet are have set displacements. The deformation is characterized by the linear strain in a homogeneous crack-free sheet normal to the plane of the crack, ε_y^∞, parallel to the crack, ε_x^∞, and in shear, ε_{xy}^∞. The corresponding

[1] Analysis of a sheet with W/a=40 yielded results for kink angles within 0.2° of those for W/a=20.

reference stresses are $\sigma_{xx}^{\infty} = E_o \dfrac{\varepsilon_{xx}^{\infty}(1-\nu)+\nu\varepsilon_{yy}^{\infty}}{1-\nu-2\nu^2}$, $\sigma_{yy}^{\infty} = E_o \dfrac{\varepsilon_{yy}^{\infty}(1-\nu)+\nu\varepsilon_{xx}^{\infty}}{1-\nu-2\nu^2}$ and $\sigma_{xy}^{\infty} = \dfrac{E_o\varepsilon_{xy}^{\infty}}{(1+\nu)}$. The biaxiality of the deformation B_ε is the ratio of the normal strain in the x-direction to that in the y-direction is $\dfrac{\varepsilon_{xx}^{\infty}}{\varepsilon_{yy}^{\infty}}$ and can be related to the biaxiality of the reference stress through $B_\sigma = \dfrac{\sigma_{xx}^{\infty}}{\sigma_{yy}^{\infty}} = \dfrac{B_\varepsilon(1-\nu)+\nu}{(1-\nu)+\nu B_\varepsilon}$. The far-field (or reference) phase angle is defined as $\psi^{\infty} = \tan^{-1}(\sigma_{xy}^{\infty}/\sigma_{yy}^{\infty})$. For a homogeneous material, the phase angle at the tip of a crack $\psi = \tan^{-1}(K_{II}/K_I) = \psi^{\infty}$. However, for graded structures, there will be a shift in the phase angle corresponding to gradient strength (Erdogan, 1995). Furthermore, for homogeneous materials the T-stress is a linear function of the stress biaxiality, B_σ. Less well understood is the nature of the T-stress for FGMs.

5.4.2 Kink angle selection methodologies

5.4.2.1 Maximum energy release rate criteria

The energy release rate, G, is derived from the work, W, necessary to close the kink. This uses the tractions t_i of the unkinked solutions and the crack opening displacements δ_i of the kinked solution (schematically, the geometries in Figure 5.1a and 5.1b) via

$$W = \left(\int_0^{\Delta a} t_i u_i \, da\right)_{\substack{top\\face}} + \left(\int_0^{\Delta a} t_i u_i \, da\right)_{\substack{bottom\\face}} = \int_0^{\Delta a} t_i \delta_i \, da \,, \tag{5.5}$$

(summing over repeated index i=1,2.) Given the spatially discrete nature of the finite element solution, the nodal stresses and displacements are used as integration points to numerically evaluate Eq. 5.5; however, the linear elastic stresses at the root of the kink (r=0) are infinite. Therefore the stresses at those nodes cannot be directly used in a numerical integration. (The FEA *will* report finite stress values, but they will be mesh dependent.) The integration along the kink is divided into two parts, one to be solved analytically $(\text{from } r = 0 \; to \; \frac{\Delta a}{M})$ and one numerically $(\text{from } r = \frac{\Delta a}{M} \; to \; \Delta a)$. The stresses and displacements in the two elements closest to the kink root were approximated analytically; this corresponds to an M of 12.5 for the kink modeled with 25 elements.

For the analytical calculation of the work, approximations are made for the stress behavior for the unkinked crack and the opening displacements for the kinked crack. Near the root of the kink, the stress is assumed to behave as a Williams singularity. Near the tip of the kinked crack, opening displacements scale with $\sqrt{(\Delta a - r)}$, but near $r = 0$ they can be seen to be approximately linear. The work is therefore an integral of the product of the singular (unkinked) stresses and the linear kink face opening:

$$W(r = 0 \; to \; \frac{\Delta a}{M}) = \int_0^{\Delta a / M} \frac{\overline{\sigma_{r1}}}{\sqrt{r}} \cdot \left(\overline{\delta_{r1}} + \overline{\delta_{r2}} \cdot r\right) + \frac{\overline{\sigma_{\theta 1}}}{\sqrt{r}} \cdot \left(\overline{\delta_{\theta 1}} + \overline{\delta_{\theta 2}} \cdot r\right) da \quad (5.6)$$

The values for $\overline{\sigma}_{r1}, \overline{\sigma}_{\theta 1}$, which scale the singular unkinked stresses, are fit from the stresses from the 3rd and 4th elements from the crack tip (as the two elements neighboring a singularity are not considered to be accurate (Williamson *et al.*, 1995)). $\overline{\delta}_{(r,\theta)(1,2)}$ are fit from the kinked solution displacements. The work over the remainder of the length

(from $r = \frac{\Delta a}{M}$ to Δa) is integrated using Simpsons rule and the nodal values from stress and displacement.

The formal definition of the strain energy release rate, G, refers to the change in potential in the small crack limit. A finite kink energy release rate is defined by, $G^{\Delta a} \equiv \frac{W}{2\Delta a}$; clearly as $\Delta a \longrightarrow 0$, $G^{\Delta a} \longrightarrow G$. When comparing kinks with different angles, this methodology yields the angle at which a kink of a given length, Δa, is most energetically favorable to form. This will be referred to as the G_{max} angle, ω_{Gmax}.

5.4.2.2 Pure opening mode criteria

To determined the phase angle of the kink, the crack opening displacements were fit using the known near-tip behavior:

$$\delta_\theta + i\delta_r = \frac{\sqrt{\Delta a - r}}{E'}\left(K_I + iK_{II}\right) \tag{5.7}$$

Rearranging yields:

$$\psi^{\Delta a} = \arctan\left(\frac{\delta_r}{\delta_\theta}\right) \tag{5.8}$$

The displacements of the 2nd element behind the tip of the kink are fit to (5.7) and the phase angle calculated. Note, that as the G_{max} criteria is integrated over Δa, the results reflect conditions along the entire kink length, but the K_{II}=0 criteria only depends on conditions near the tip of the kink.

5.4.3 Procedures

For each far-field phase angle, ψ^{∞}=45°,0°,-45° and deformation biaxiality B_{ε}={1,0,-1}, kink lengths of $\Delta a/a$={10^{-4}, 10^{-3}, $3\cdot10^{-3}$, 10^{-2}, $3\cdot10^{-2}$, 10^{-1}, $3\cdot10^{-1}$} are analyzed. In addition to the homogeneous case, a gradient in the Young's modulus was assumed for analysis, where

$$E(y) = (c-1)\tanh(b \cdot y) + c \qquad (5.9)$$

and b=100/a, c=10.5. This allows for a twenty-fold change in the Young's modulus. Ninety percent of the change occurs over a distance Δy ~3/b and $\frac{\nabla E}{E(0)} = \frac{b(c-1)}{c} \approx b$.

Possion's ratio, ν, was taken be 0.3 for all cases.

A family of kink angles was analyzed for each phase angle and kink length, from ω=-85° to 85° in increments of 5°. For each kink angle, the work and kink-tip phase angle were calculated. A parabola was fit to the angles with the 3 largest $G^{\Delta a}(\omega)$. The angle corresponding the maximum of that parabolic equation was set to be $\omega_{Gmax}(\Delta a)$. The two points with phase angles closest to 0 were also selected and $\omega_{KII=0}(\Delta a)$=0 linearly interpolated.

5.5 Results and Discussion

5.5.1 Homogeneous material kink angles

The optimal kink angle predicted by the two criteria are displayed in Fig 5.5 for a homogeneous material with phase angle ψ^{∞}= 45° and 75° and B_{ε}=0. Solid lines indicate the predictions under the G_{max} formula: -56.6° and–69.3° respectively. Dashed lines show that for the K_{II}=0 criteria: –57° and –71.5° (Suo and Hutchinson, 1992). These

analyses assume an infinite K-field and are therefore independent of the length scale of the kink, Δa. This independence has been confirmed numerically by Geubelle and Knauss (1995).

The finite element analysis results show excellent agreement for the smallest kink lengths $\Delta a/a=10^{-4}$. For longer kink lengths, there is a monotonic deviation of the finite element results from the analytical. This is due to the influence of finite geometry, primarily the T-stress. For both phase angles, $T/(|K|/\sqrt{a})=-0.2$. (This is nearly the same value as a sheet in uniaxial tension under load boundary conditions (Sherry, 1995)).

A negative T-stress stabilizes a straight-ahead crack (Cotterell, 1965), which corresponds to a decrease in the optimal ω for the sample studied. The deviation of the numerical results from the analytical theories will be used for comparison with the graded material results, allowing for a baseline of a kink-length effect due simply to pure T-stress effects. This effect will be quantified in subsequent sections.

For $\psi^{\infty}= 0°$ and 45°, the finite kink energy release calculated for extension along $\omega=0$ are shown in Figure 5.5(b). The results are compared to the analytical $G=\sqrt{K_1^2+K_2^2}\,/\,E'$, which holds in a pure K-field. There is no change in the results from $\Delta a/a=10^{-4}$ to 10^{-2}, but as in Figure 5.5(a), there is a change between $\Delta a/a=10^{-2}$ and 10^{-1}. This corresponds to the common assumption that of $r_K=a/10$ –$a/100$. The offset seen, ~1% for $\psi^{\infty}= 0°$ and 2% for $\psi^{\infty}= 45°$, is due to the approximate nature of the finite element results, which will always under-predict the displacements. This offset error could be reduced with additional mesh refinement.

5.5.2 Graded material

5.5.2.1 Kink angles

The optimal kink angle predicted by the two criteria are displayed in Figure 5.6a for far-field phase angle ψ^{∞}= 45°, 0°, -45°, deformation biaxiality B_{ε}=1, and $E(y)$ with $b{\cdot}a$=100. Table 5.1 shows the results for the smallest kink calculated $\Delta a/a=10^{-4}$ and the asymptotic short-kink limit (denoted for $\omega_{KII=0}$ by ◁ on the y-axis in Figure 5.6a). These agree within 4°.

Table 5.1 Tip parameters for graded sheet

ψ^{∞}	ψ	$\omega_{Gmax}(\Delta a\rightarrow 0)$	$\omega_{KII=0}(\Delta a\rightarrow 0)$	$\omega_{Gmax}(\Delta a/a=10^{-4})$	$\omega_{KII=0}(\Delta a/a=10^{-4})$
-45°	-10°	19.2	19.1	19.4°	19.6°
0°	32°	-46.9	-47.3	-50.6°	-50.5°
45°	75°	-69.3	-71.3	-73.3°	-74.2°

As kink lengths increase, the value of the kink angle is found to decrease (become more negative). This trend is steady until roughly $\Delta a/a=10^{-2}$ (or $\Delta a{\cdot}b$=0.1). The effects for even longer kink lengths are twofold: 1) the two criteria drastically diverge and 2) for most cases the trend in optimal kink angle rapidly increases (becomes less negative).

The first of these effects is due to the fact that the K_{II}=0 criteria is localized to the tip of the kink, whereas the energy criteria used here depends on the tractions and displacements all along the kink. For cracks, in radially self-similar stress fields, there is no change with kink length. However, for longer kinks, with lengths comparable to the governing elastic dimension, this no longer holds. The change in the nature of the stress field is due the modulus gradient. Comparable disparity would be expected in a homogeneous sample for $\Delta a/a\sim 1$.

The effect of biaxiality is displayed in Fig 5.6b and 5.6c. These display the kink angles for cases with deformation biaxiality B_ε=0 and –1. The trend in most cases is that the magnitude of kinking is decreased with decreasing biaxiality. To the first approximation this can be understood through the same effect as in the homogeneous case. The application of a far-field compressive stress $\sigma_{xx}^{\infty} < 0$ will decease the T-stress by $T(\sigma_{xx}^{\infty})=T(0)+\sigma_{xx}^{\infty}$. This simple relation does not hold for the graded case.

5.5.2.2 Modulus affected stresses

The change in the stress fields with radial distance from the tip is demonstrated in Fig 5.7. This shows the $\{\sigma_{rr},\sigma_{\theta\theta},\sigma_{r\theta}\}\cdot\sqrt{(2\pi r)}$ at distances of $r=10^{-4}a=10^{-2}/b$ (a) and $r = 10^{-2}a = 1/b$ (b). For comparison, the results of the Williams equation are in Fig. 5.8a. Although the finite element results agree well with the Williams field at the smaller dimension, at the larger there are drastic differences in the fields. First, the location of the maximum hoop stress has shifted roughly 40°. Second, focusing along θ=0°, there is a large difference between σ_{rr} and $\sigma_{\theta\theta}$. In a Williams field, regardless of phase angle, these are the same at this angle. Somewhat more subtle is the larger variation in σ_{rr} with angle.

It is interesting to compare these results with the analytical description of the stress field in the neighborhood of an interface crack. In the limit of $b\rightarrow\infty$, the gradient will form a sharp interface with E_1/E_2=20. In the notation of interface mechanics, this corresponds to Dundurs parameters of $\{\alpha,\beta\}=\{0.9,0.26\}$(Dundurs, 1968) and an oscillatory index ε= -0.084. Setting the reference phase angle to be the same as the FGM case at $r=10^{-4}a$ and using the equations for an interface crack (Rice *et al.*, 1990), the

results of Fig 5.8b are obtained. It can be seen that the shift in the location of maximum hoop stress in predicted by the interface equations, although with a sharper maximum than in the FGM case. The radial stresses are discontinuous across the interface, but at this distance from the tip in an FGM, the change in properties is still experienced over a number of elements and such discontinuities are not allowed. The trend for substantially larger stresses for $\theta>0$ is seen in the interface analysis just as in the finite element results for the FGM. In addition, the normalized difference between the σ_{rr} and $\sigma_{\theta\theta}$ is greater in the FGM case than predicted by either the homogenous or interface-crack solutions.

Thus it is apparent that the interface mechanics solution captures some of the effect of the gradient at this distance from the crack tip. For sufficiently large bodies and long kinks ($\Delta a \cdot b \gg 1$) the distinction between the sharp and the graded sigmoidal interface could be diminished. In this situation, interface fracture mechanics solutions could be applied directly.

5.5.2.3 Parallel stress approximation

The power-series solution to the homogeneous crack problem indicated that the second term in the stress solution is constant. For free crack faces, the normal and shear tractions must be zero, so the only constant non-zero component must be σ_{xx}. For graded materials, this line of argument is on weaker ground, as a constant stress in a material with varying modulus violates the conditions of compatibility. Suffice it to say that the next-order term in the stress solution will be *T*-like in that the boundary conditions still dictated that the effect of the higher order terms will be strongest in the *xx*-component of

stress. To what extent this term for FGMs, denoted T_b, is constant, has not been established analytically. It also is evident from Fig. 5.7b that there are terms acting on all components of stress within $r < 1/b$.

To attempt to capture the effects of the gradient-induced stresses, the apparent T-stress, σ_{xx}-σ_{yy} (θ=0), was calculated for the FGM cases. Theses are displayed in Fig. 5.9abc for a range of distances from the crack tip. In the homogeneous case, T is independent of ψ^∞. However, just as the tip phase angle is shifted for the FGM case, T_b is as well, with its value adjusted significantly by the far-field phase angle, ψ^∞. It is apparent for each case that sufficiently close to the crack tip (r<0.1 b) the apparent T-stress is approximately constant. There are variations (roughly 50% from $r=10^{-5}a$ to $10^{-3}a$), but given the dominance of the singular components of the stress field at theses dimension, changes on the order of 1000% are expected. A single value for T_b was defined to be the average over two elements as $r \longrightarrow 10^{-5}a$.

The effect of biaxiality is seen with a nonlinear decrease in the apparent T-stress with decreasing deformation biaxiality (Table 5.2). For a given ψ^∞, T_b shifts roughly linearly with the nominal far-field stress σ_{xx}^∞, although a more thorough exploration of the dependence of T_b on both B_ε and ψ^∞ would be required to establish the explicit dependence.

Table 5.2 Normalized apparent T-stress, $T_b\sqrt{a}/|K|$

ψ^∞	B_ε=1	B_ε=0	B_ε=−1
-45°	-0.2	-0.77	-2.2
0°	4.8	4.1	2.2
45°	7.3	6.9	5.4
B=0, all ψ^∞	0.13	-0.20	-1.0

Combining asymptotic T_b with the tip phase angle ψ, Eq. 5.3b allows a prediction of the dependence of kink angle on kink length expected by the K_{II}=0 criteria in a homogeneous material. These predictions are included in Fig 5.6 (dashed-dot lines). As expected, these curves asymptote to the short-crack values for small $\Delta a/a$. There is excellent agreement with the prediction for homogeneous materials and the FGM results for small $\Delta a/a$. The agreement ends as $b \cdot \Delta a$=0.1, where, as discussed, the next-order term not captured by a constant T_b in the stress analysis is expected to begin altering the behavior of the kink.

5.5.2.4 Bifurcation in energy criteria

The kink angle resulting for the G_{max} criteria are not displayed in Figure 5.6abc for the ψ^{∞}=-45° case and $\Delta a/a > 10^{-3}$ ($\Delta a \cdot b > 0.1$). This is due to a bifurcation in $G^{\Delta a}$, as displayed in Figure 5.10. For short kinks $\Delta a/a \leq 10^{-2}$, there is a single maximum, as in the homogeneous case. However, it is evident that kinking down into increasingly compliant material as ω<0° is conducive to increasing values of energy release in a direction not predicted by either the far-field or tip phase angles. Note that for fixed K, the analytic expression $G=K^2/E'$ predicts an inverse relationship between energy release rate and elastic stiffness.

This behavior is limited to the ω_{Gmax} criteria, as the kinks below 0° are subject to a high amount a shear and only a single ψ^{kink}=0 angle is found, as displayed in Fig 5.6. Beyond ω=45°–60° the kink closes (δ_θ=0) and the energy release is due entirely to sliding opening, δ_r. For kink angles beyond this limit, the crack faces come into contact.

If detailed results of crack behavior in this regime were to be studied, then a contact-element routine would be required. This is beyond the scope of this investigation.

It is apparent that for kinks of sufficient length there is a competition between the traditional near-tip driving force and that energy release available by growing the crack in shear into the very compliant region. Negative far-field loading drives the crack up into the stiffer material and the compliance effects are of opposite direction. Naturally, for conditions of positive tip phase angle (ψ^{∞}=0°, 45°), the driving forces compliment each other, rather than compete, and this bifurcation is not observed.

5.6 Concluding Remarks

Even with a full accounting for the effect of a modulus gradient in an FGM, accurate modeling of the fracture behavior requires additional analysis. For sharp interfaces, the balance of the mechanical driving force and the relative toughness determines the direction of crack propagation. For the crack to kink off the interface and into the substrate (along ω), the criteria $G(\omega)/G_c^{Sub} > G(0)/G_c^{If}$ (where G_c^{Sub},G_c^{If} are the toughness, in terms of energy release rate, of the substrate and the interface) has been established (He *et al.*, 1991). In general, the fracture toughness of inhomogeneous material will also vary with direction. This may be due to variance in the composite surface energy, Γ, and atom trapping for an elastic material or the yield strength for an elastic-plastic material. Therefore a similar competition between regions of higher stress (or potential energy release rate) and lower material resistance will be established. The domains in which each of these effects are dominant or are in competition must be determined in order to successfully predict the experimental fracture behavior.

5.7 SUMMARY

Established theories for the kinking of a mixed-mode crack use the tip phase angle to determinate the optimal angle. For homogeneous materials, the K_{II}=0 and G_{max} criteria agree within 5° for all but the most extreme kink angles. There is an additional effect of the T-stress, which will increase the magnitude of kinking when positive and inhibit kinking when negative. For very short kinks in FGMs the phase angle predictions agree with finite element results within 4°. For kink lengths within $\Delta a<1/b$ the K-dominant regime for homogeneous bodies, the dependence of kink angle on kink length is well modeled by calculating the apparent T-stress. This was found to be much larger for the FGMs studied than for the a homogeneous material with the same geometry and loading. For a positive apparent T-stress, the crack path was less stable, with the crack closely following the asymptotic kink angle predictions only for $\Delta a/a<10^{-3}$. Outside of the gradient dimension, $1/b$, there is a drastic effect of kink length that cannot be characterized by either the stress intensity factors or a constant parallel stress, including a widened divergence between the predictions base on energy maximization (G_{max}) and on kink symmetry (K_{II}=0).

5.8 REFERENCES

Bogy, D., 1971. Two edge-bonded elastic wedges of different materials and wedge angles under surface tractions. *J. Appl. Mech.*, 38, 377-89.

Cotterell, B., 1965. On brittle fracture paths. *Int. J. Fract. Mech.*, 1, 96-103.

Cotterell, B., 1966. Notes on the paths and stability of cracks. *Int. J. Fract.*, 2, 526-33.

Cotterell, B. and Rice, J. R., 1980. Slightly curved or kinked cracks. *Int. J. Fract.*, 16, 155-69.

Du, Z. Z. and Hancock, J. W., 1991, The effect of non-singular stresses on crack-tip constraint. *J. Mech. Phys. Solids*, 39, 555-67.

Dundurs, J. J. , 1969. Edge-bonded dissimilar orthogonal elastic wedges under normal and shear loading. *J. Appl. Mech.*, 36, 650-2.

Delale, F. and Erdogan, F., 1983. Interface crack in a nonhomogeneous elastic medium. *Int. J. Engng. Sci.*, 26, 559-68.

Du, Z. Z. and Hancock, J. W., 1991, The effect of non-singular stresses on crack-tip constraint. *J. Mech. Phys. Solids*, 39, 555-67.

Erdogan, F., 1985. The crack problem for bonded nonhomogeneous materials under antiplane shear loading. *J. Appl. Mech.*, 52, 823-28.

Erdogan, F., 1995. Fracture mechanics of functionally graded materials. *Compos. Engng.*, 5, 753-70.

Erdogan, F. and Sih, G. C., 1963. On the crack extension in plates under plane loading and transverse shear. *J. Basic Engng.*, 85, 519-27.

Evans, A. G., 1978. A general approach for the statistical analysis of multiaxial fracture. *J. Am. Ceram. Soc.*, 61, 302-08.

Finnie, I., and Saith, A., 1973. A note on the angled crack problem and the directional stability of cracks. *Int. J. of Fract.*, 9, 484-6.

Geubelle, P. H. and Knauss, W. G., 1995. Crack propagation in homogeneous and bimaterial sheets under general in-plane loading: Nonlinear analysis. *J. Appl. Mech.*, 62, 601-06.

Gu, P. and Asaro, R. J., 1997. Crack deflection in functionally graded materials. *Int. J. Solids Struct.*, 34, 3085-98.

Hayashi, K. and Nemat-Nasser, S. , 1981. Energy-release rate and crack kinking under combined loading. *J. Appl. Mech.*, 48, 520-4.

He, M.-Y. and Hutchinson, J. W. , 1989. Kinking of a crack out of an interface. *J. Appl. Mech.*, 56, 270-8.

He, M.-Y., Bartlett, A., Evans, A. G. and Hutchinson, J. W. , 1991. Kinking of a crack out of an interface: role of in-plane stress. *J. Am. Ceram. Soc.*, 74, 767-71.

Hutchinson, J. W. and Suo, Z. , 1992. Mixed Mode Cracking in Layered Materials. *Advances in Appl. Mech.*, 29, 64-191.

Jin, Z.-H. and N. Noda, N., 1994. Crack-tip singular fields in nonhomogeneous materials. *J. Appl. Mech.*, 61, 738-40.

Jin, Z.-H. and Batra, R. C. , 1996. Some basic fracture mechanics concepts in functionally graded materials. *J. Mech. Phys. Solids*, 44, 1221-35.

Konda, N. and Erdogan, F., 1994. The mixed mode crack problem in a nonhomogeneous elastic medium. *Engng. Fract. Mech.*, 47, 533-45.

Lee, Y.-D. and Erdogan, F., 1994-1995. Residual/thermal stresses in FGM and laminated thermal barrier coatings. *Int. J. Fract.*, 69, 145-165.

Palaniswamy, K. and Knauss, W.G., 1978. On the problem of crack extension in brittle solids under general loading. in: S. Namat-Nassar (ed.) *Mechanics Today*, Vol. 4. Pergamon Press, New York, 1978.

Rice, J. R., Suo, Z. and Wang, J.-S. ,1990. Mechanics and Thermodynamics of Brittle Interfacial Failure in Bimaterial Systems, in *Metal-Ceramic Interfaces*. M. Ruhle, A. G. Evans, M. F. Ashby and J. P. Hirth. Oxford, Pergamon Press: 269-94.

Singh, D. and Shetty, K.S., 1989. Fracture toughness of polycrystalline ceramics in combined mode I and mode II loading. *J. Am. Ceram. Soc.*, 72, 78-84.

Sherry, A. H., France, C.C. and Goldthorpe, M. R., 1995. Compendium of *T*-stress solutions for two and three dimensional cracked geometries. *Fatigue Fract. Engng. Mater. Struct.* 18, 141-55.

Tada, H., Paris, P. C. and Irwin, G. R., 1985. *The Stress Analysis of Cracks Handbook.* Del Corp./Paris Productions, Inc., St. Louis, Mo.

Williams, M. L. , 1957. On the stress distribution at the base of a stationary crack. *J. Appl. Mech*, 79, 109-14.

Williamson, R. L., Rabin, B. H. and Byerly, G. E. , 1995. FEM study of the effects of interlayers and creep in reducing residual stresses and strains in ceramic-metal joints. *Compos. Engnrg.*, 5, 851-63.

Zienkiewicz, O.C. and Taylor, R.L., 1989. *The Finite Element Method.* McGraw-Hill, New York, N.Y.

5.9 FIGURE CAPTIONS

Figure 5.1 Schematic of straight (a) and kinked (b) cracks. The state at the tip of the unkinked crack is characterized by stress intensities K_1, K_2. The kink at angle ω to the y=0 plane with length Δa is characterized by K_I, K_{II}.

Figure 5.2 Comparison of three theories for optimal crack kinking angle in homogeneous materials. Predicted kink angles are based on loading phase angles ψ. Up to ω~45°, they agree within 5°. Maximum stress criteria, $\sigma_{\theta\theta,max}$ is based solely on the stress state before kinking. The K_{II}=0 criteria dictates that kinks will grow only in a state of pure crack tip tension. The maximum energy release rate criteria, G_{max}, selects paths based on a global reduction in energy.

Figure 5.3 Schematic of the problem studied, a cracked sheet in tension and shear. Displacements were fixed on all boundaries and loading characterized by the apparent normal and shear strains, $\varepsilon_{xx}^{\infty}$, $\varepsilon_{yy}^{\infty}$ and $\varepsilon_{xy}^{\infty}$. The crack was small compared to the sheet, W/a=20 and the kink was smaller than the crack, $\Delta a/a$<0.3.

Figure 5.4 Detail of the finite element mesh near the kinked crack. Refinement was employed to capture the details of the stress singularities. The fan array set elements every 5° with 20 elements positioned along the length of the kink. An 8-element fan was meshed at the tip of the kink.

Figure 5.5 (a) Kink angles for homogeneous sheet with phase angle ψ=45° and 75°. The optimal kink angles determined by two criteria are displayed (closed symbols) and compared with those from the short-kink theories (lines). (b) Finite kink energy release, $G^{\Delta a}$, normalized by the energy release rate $G = \sqrt{K_1^2 + K_2^2} / E'$. These measures will agree in a pure K-field. The T-stress in the homogeneous sample causes the deviations for the longer kink lengths.

Figure 5.6 Kink angle for finite kink length in an FGM with $E(y)$ and deformation biaxiality B_ε=1 (a), 0 (b) and −1 (c). The asymptotic short kink angle under the K_{II}=0 criteria is displayed as ◁ on the y-axis. The effect of the T-stress is modeled by the analysis of He *et al.* (1991) which includes the effect of $T\sqrt{\Delta a}$ for homogeneous materials. The dependence of kink length for $\Delta a < 1/b$ is found to follow the results of this analysis.

Figure 5.7 Polar stress components calculated at $r=10^{-2}/b$ (a) and $1/b$ (b) for ψ^{∞}=0°. At the smaller distance, the finite element results compare well with the Williams field (Fig. 5.8a). The stresses in (b) are dramatically different, including a shift in the angle of maximum hoop stress, $\sigma_{\theta\theta}$.

Figure 5.8 The analytical stress fields for cracks in homogeneous materials (a) and on bimaterial interfaces (b) for a reference phase angle of 32° (at L=0.0001 a). For the homogeneous materials, these results are independent of r. For the interface case, r is set to be $100L$, which facilitates comparison with Fig 5.7b. The shift in the angle of maximum hoop stress compares to that in Fig 5.7b, as well does the relative increase in σ_{rr} for $\theta>0$.

Figure 5.9 The apparent T-stress, $T_b=\sigma_{xx}-\sigma_{yy}$ for the FGM sheet with deformation biaxiality $B_\varepsilon=1$ (a), 0 (b) and –1 (c). When calculated sufficiently close to the crack tip. T_b is roughly constant, varying 50% from $r/a=10^{-5}$ to 10^{-3}, where the singular stress field changes 1000%. However, this has a much different value than a homogeneous sample.

Figure 5.10 The variation of the finite kink energy release, $G^{\Delta a}$, for a range of kink angles, ω, normalized to $G^{\Delta a}$ (ω=0) . Deformation biaxiality, $B^e=1$ and far field phase angle ψ^∞=-45°. For the shortest kink displayed, $\Delta a/a=10^{-2}$, there is a single maximum, as in homogeneous materials. The competition between the far-field and gradient-induced effects leads to multiple stationary points for longer kinks.

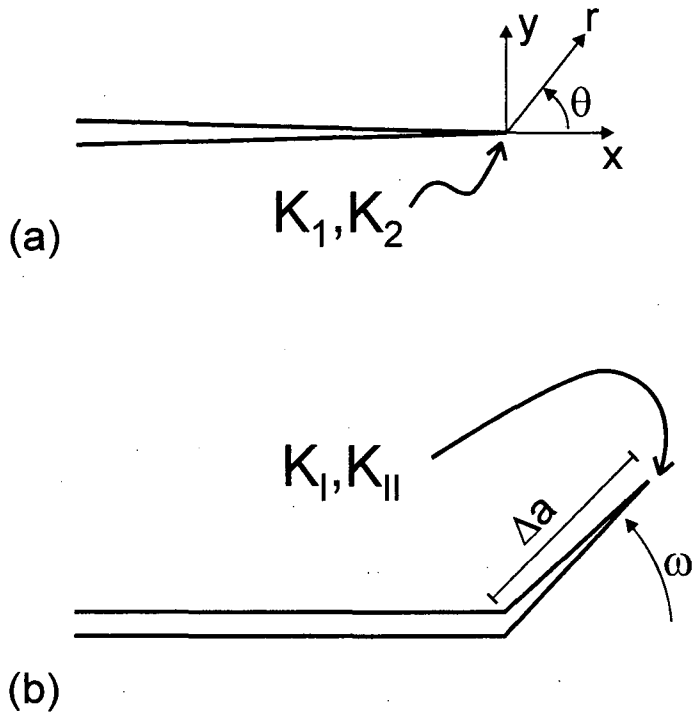

Figure 5.1 Schematic of straight (a) and kinked (b) cracks. The state at the tip of the unkinked crack is characterized by stress intensities K_1, K_2. The kink at angle ω to the y=0 plane with length Δa is characterized by K_I, K_{II}.

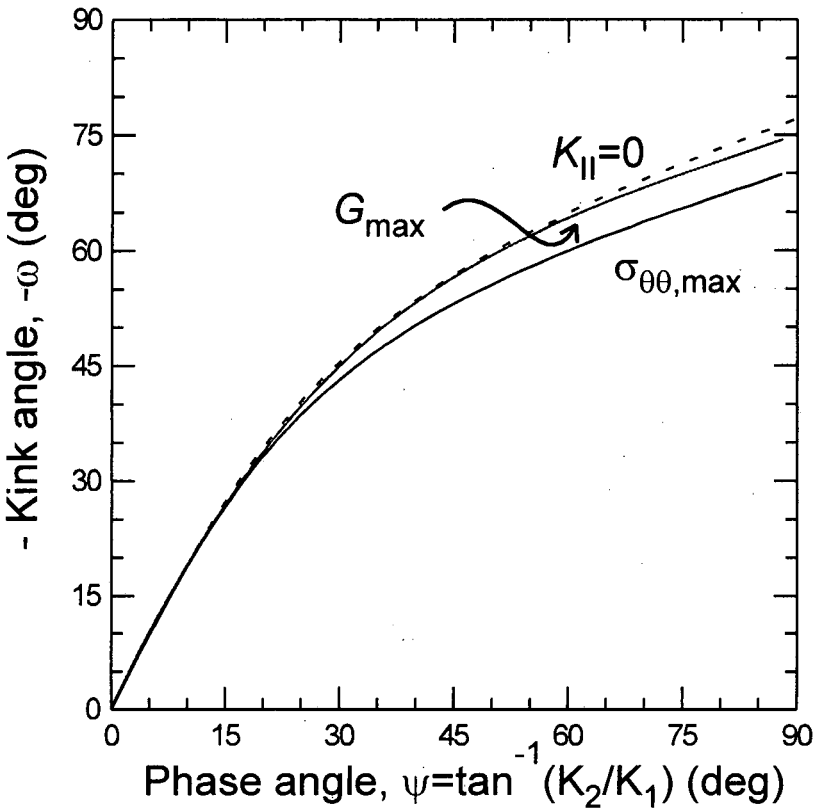

Figure 5.2 Comparison of three theories for optimal crack kinking angle in homogeneous materials. Predicted kink angles are based on loading phase angles ψ. Up to ω~45°, they agree within 5°. Maximum stress criteria, $\sigma_{\theta\theta,max}$ is based solely on the stress state before kinking. The K_{II}=0 criteria dictates that kinks will grow only in a state of pure crack tip tension. The maximum energy release rate criteria, G_{max}, selects paths based on a global reduction in energy.

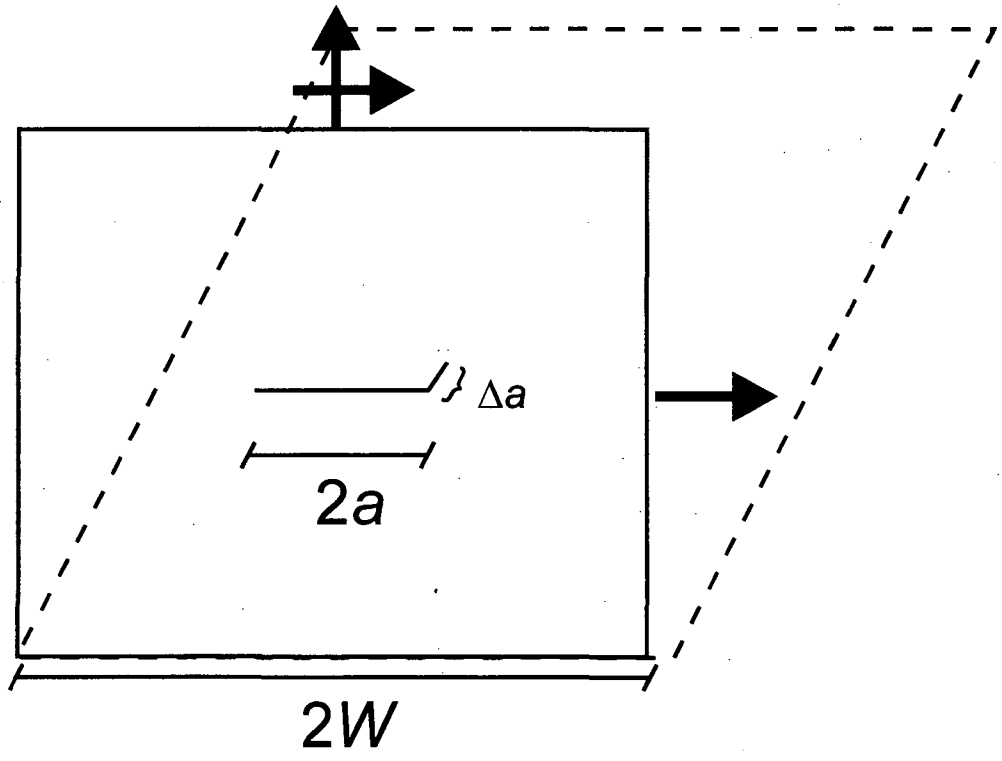

Figure 5.3 Schematic of the problem studied, a cracked sheet in tension and shear. Displacements were fixed on all boundaries and loading characterized by the apparent normal and shear strains, $\varepsilon_{xx}^{\infty}$, $\varepsilon_{yy}^{\infty}$ and $\varepsilon_{xy}^{\infty}$. The crack was small compared to the sheet, W/a=20 and the kink small compared to the crack, $\Delta a/a$<0.3.

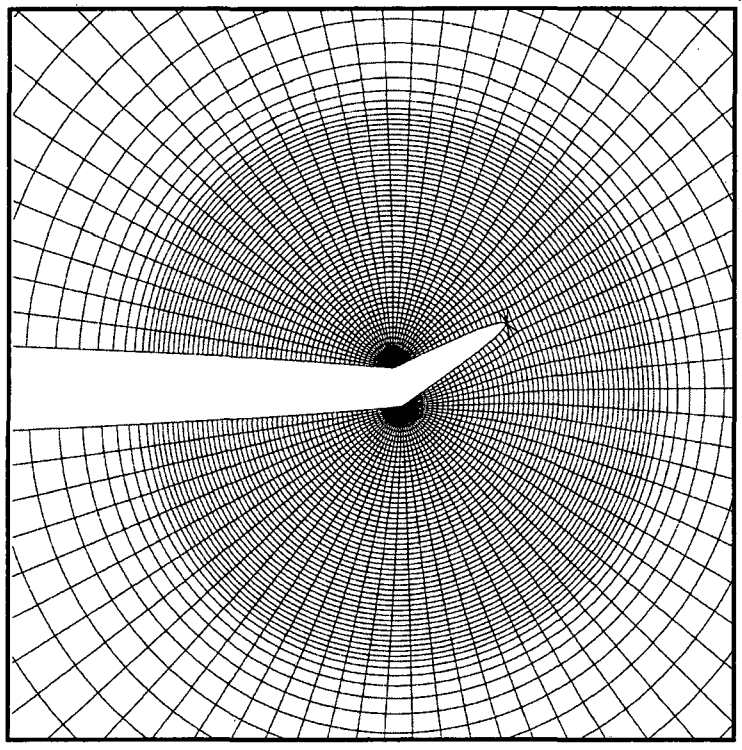

Figure 5.4 Detail of the finite element mesh near the kinked crack. Refinement was employed to capture the details of the stress singularities. The fan array set elements every 5° with 25 elements positioned along the length of the kink. An 8-element fan was meshed at the tip of the kink.

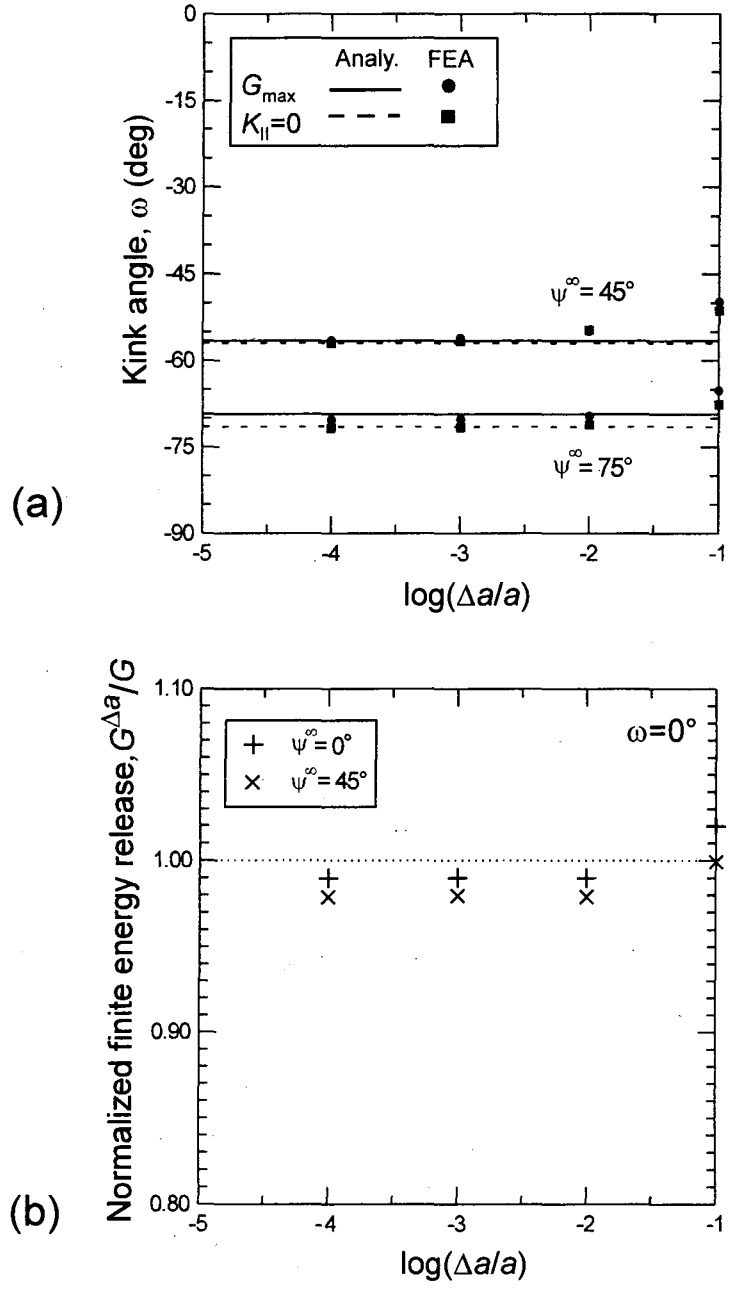

Figure 5.5 (a) Kink angles for homogeneous sheet with phase angle ψ=45° and 75°. The optimal kink angles determined by two criteria are displayed (closed symbols) and compared with those from the short-kink theories (lines).
(b) Finite kink energy release, $G^{\Delta a}$, normalized by the energy release rate $G = \sqrt{K_1^2 + K_2^2} / E'$. These measures will agree in a pure K-field. The T-stress in the homogeneous sample causes the deviations for the longer kink lengths.

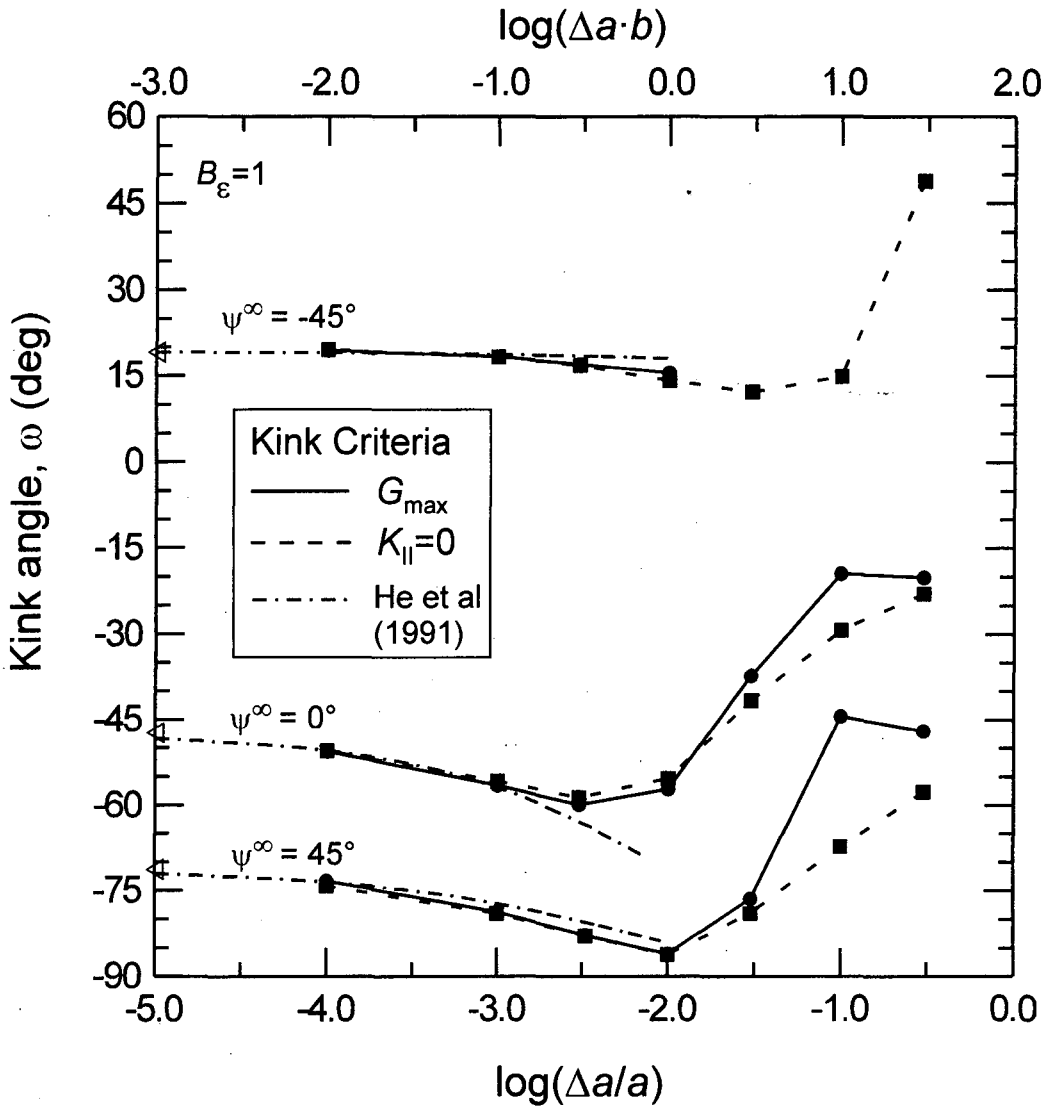

Figure 5.6 Kink angle for finite kink length in an FGM with $E(y)$ and deformation biaxiality B_ε=1 (a), 0 (b) and –1 (c). The asymptotic short kink angle under the K_{II}=0 criteria is displayed as ◁ on the y-axis. The effect of the T-stress is modeled by the analysis of He *et al.* (1991) which includes the effect of $T\sqrt{\Delta a}$ for homogeneous materials. The dependence of kink length for $\Delta a < 1/b$ is found to follow the results of this analysis.

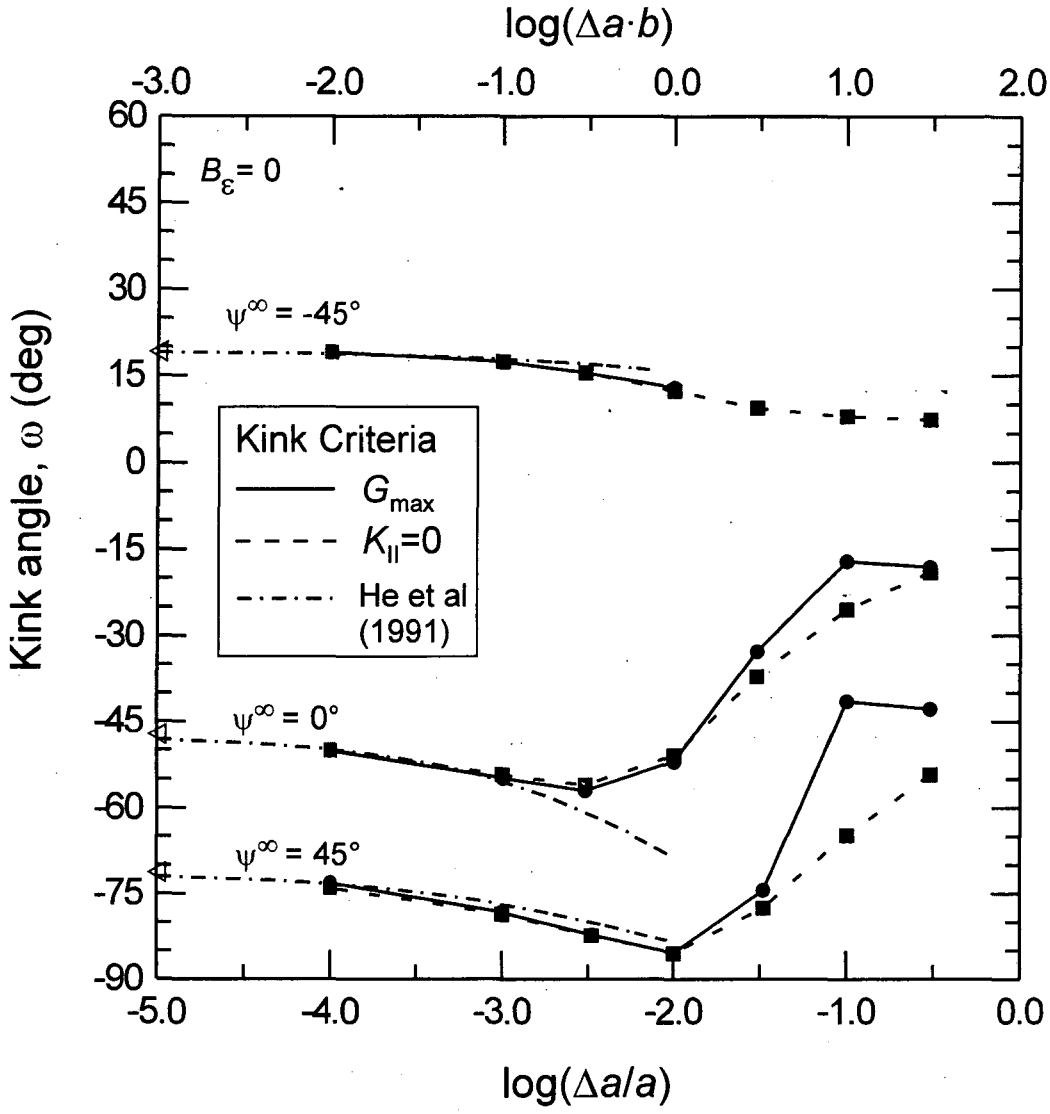

Figure 5.6 (b) Finite kink length results for a FGM with deformation biaxiality, B_ε=0.

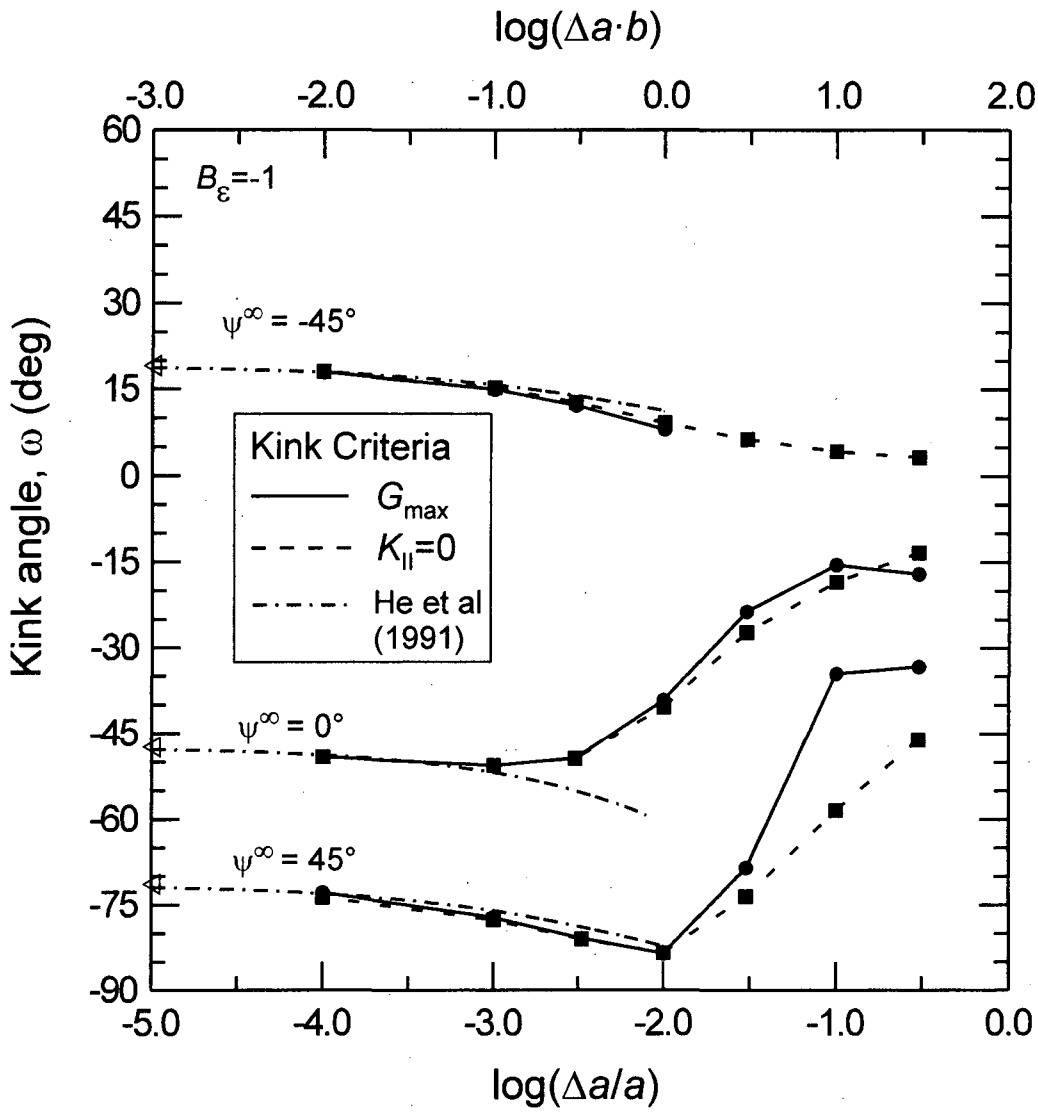

Figure 5.6 (c) Finite kink length results for a FGM with deformation biaxiality B_ε=-1.

(a)

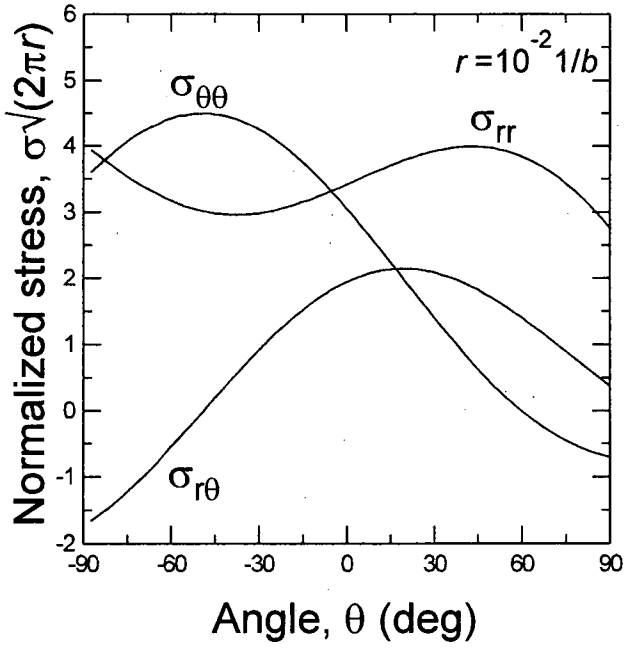

(b)

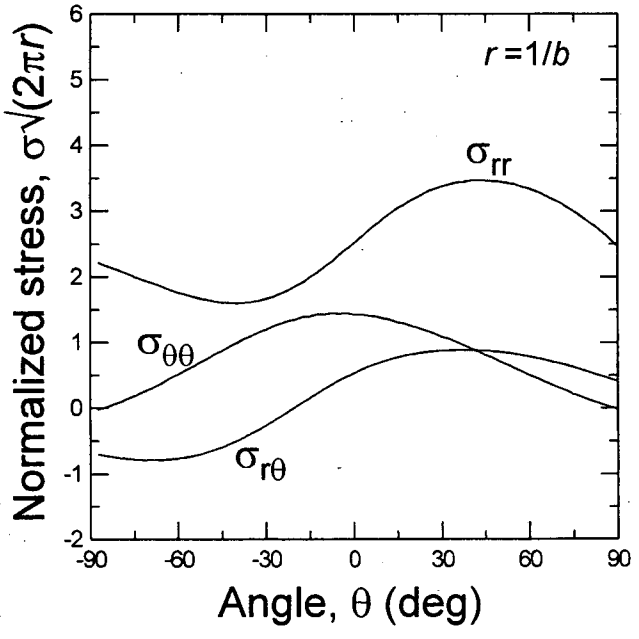

Figure 5.7 Polar stress components calculated at $r=10^{-2}/b$ (a) and $1/b$ (b) for $\psi^{\infty}=0°$. At the smaller distance, the finite element results compare well with the Williams field (Fig. 5.8a). The stresses in (b) are dramatically different, including a shift in the angle of maximum hoop stress, $\sigma_{\theta\theta}$..

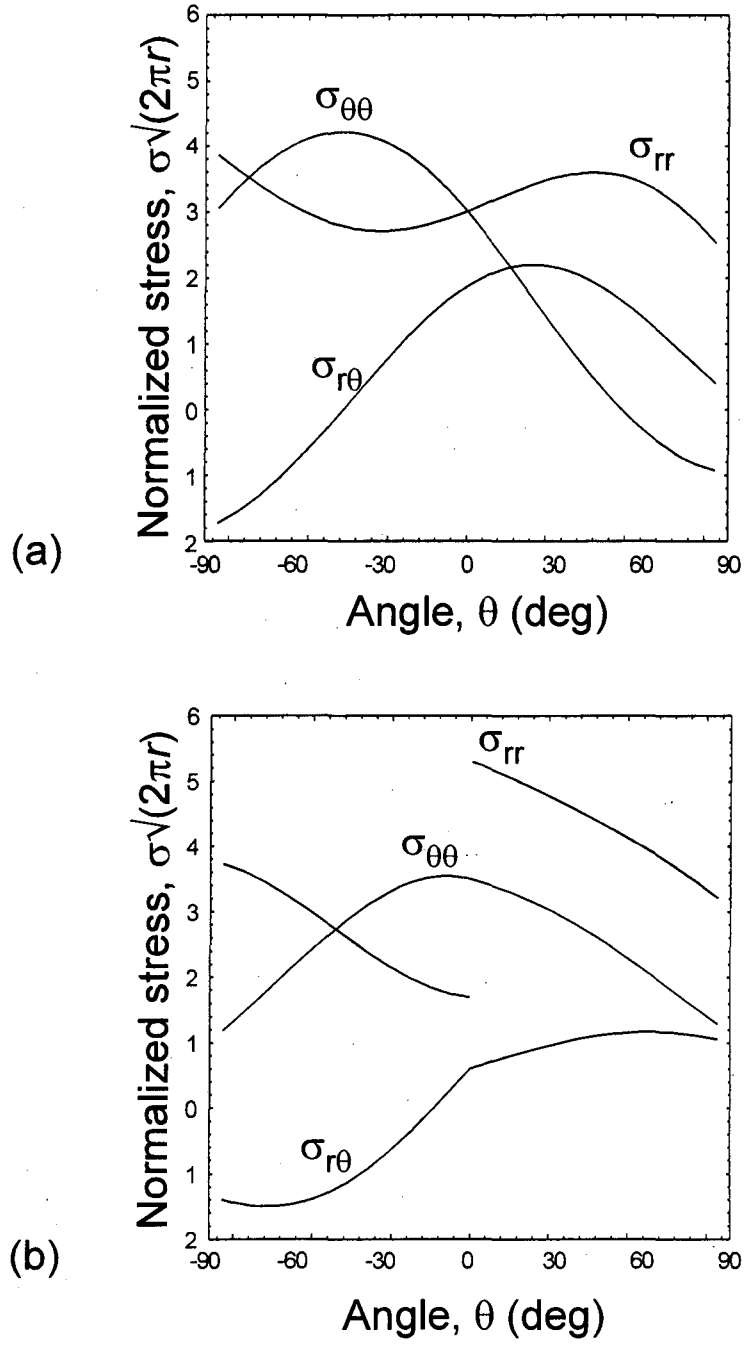

Figure 5.8 The analytical stress fields for cracks in homogeneous materials (a) and on bimaterial interfaces (b) for a reference phase angle of 32° (at L=0.0001 a). For the homogeneous materials, these results are independent of r. For the interface case, r is set to be 100L, which facilitates comparison with Fig 5.7b. The shift in the angle of maximum hoop stress compares to that in Fig 5.7b, as well does the relative increase in σ_{rr} for θ>0.

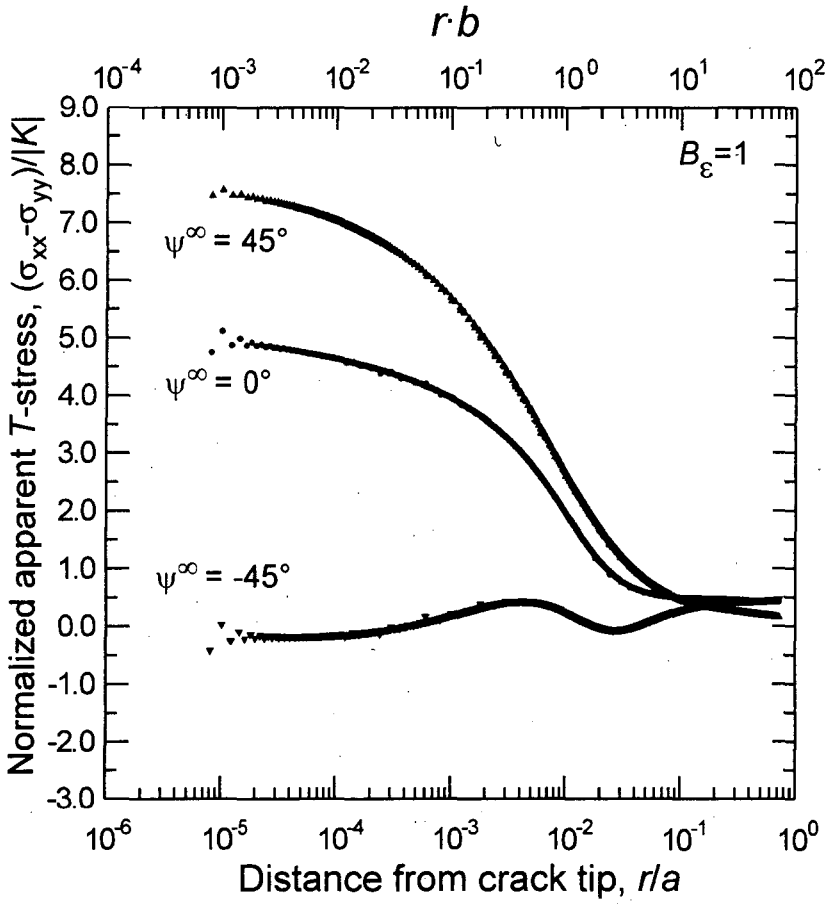

Figure 5.9 The apparent T-stress, $T_b=\sigma_{xx}-\sigma_{yy}$ for the FGM sheet with deformation biaxiality $B_\varepsilon=1$ (a), 0 (b) and -1 (c). When calculated sufficiently close to the crack tip. T_b is roughly constant, varying 50% from $r/a=10^{-5}$ to 10^{-3}, where the singular stress field changes 1000%. However, this has a much different value than a homogeneous sample.

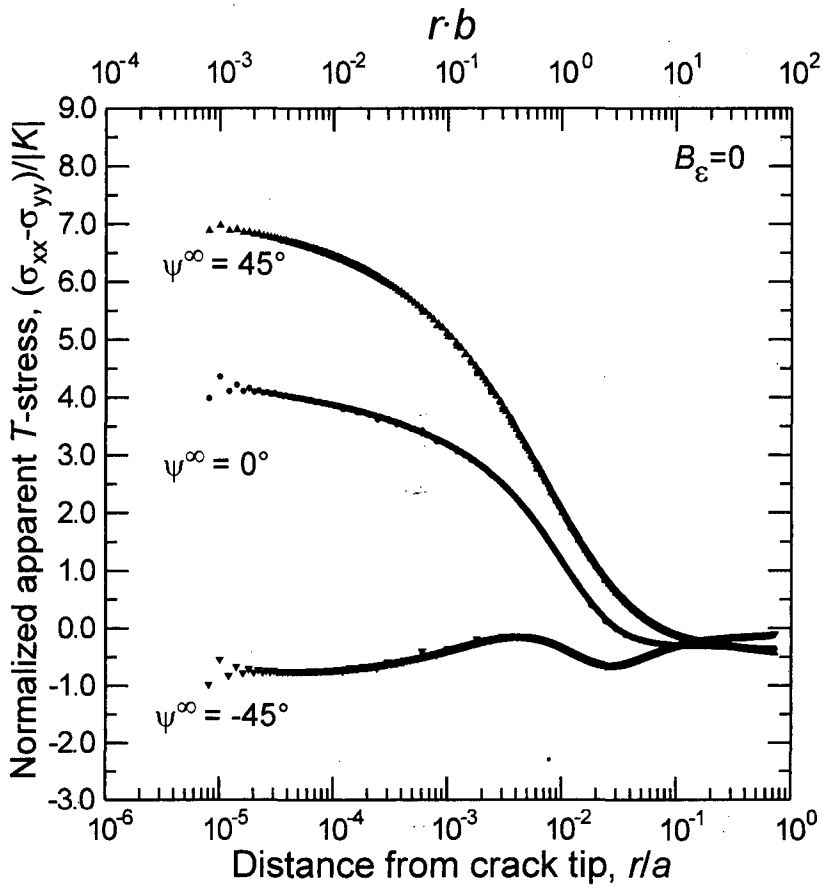

Figure 5.9 (b) The apparent T-stress, $T_b=\sigma_{xx}-\sigma_{yy}$ for the FGM sheet with deformation biaxiality $B_\varepsilon=0$.

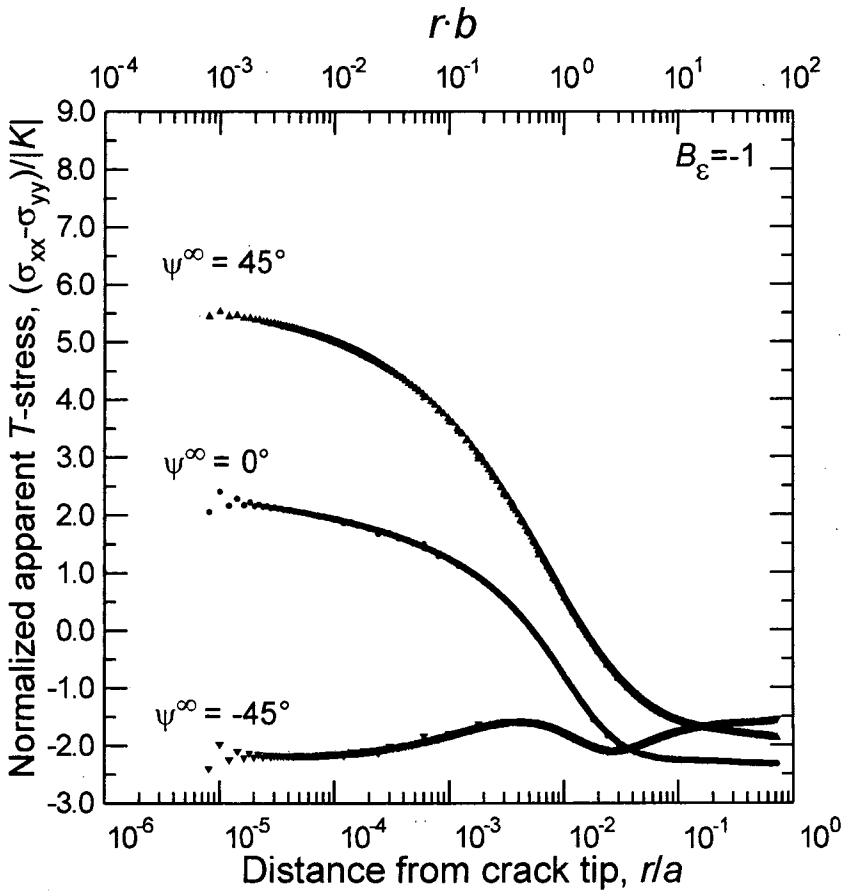

Figure 5.9 (c) The apparent T-stress, $T_b=\sigma_{xx}-\sigma_{yy}$ for the FGM sheet with deformation biaxiality B_ε=-1.

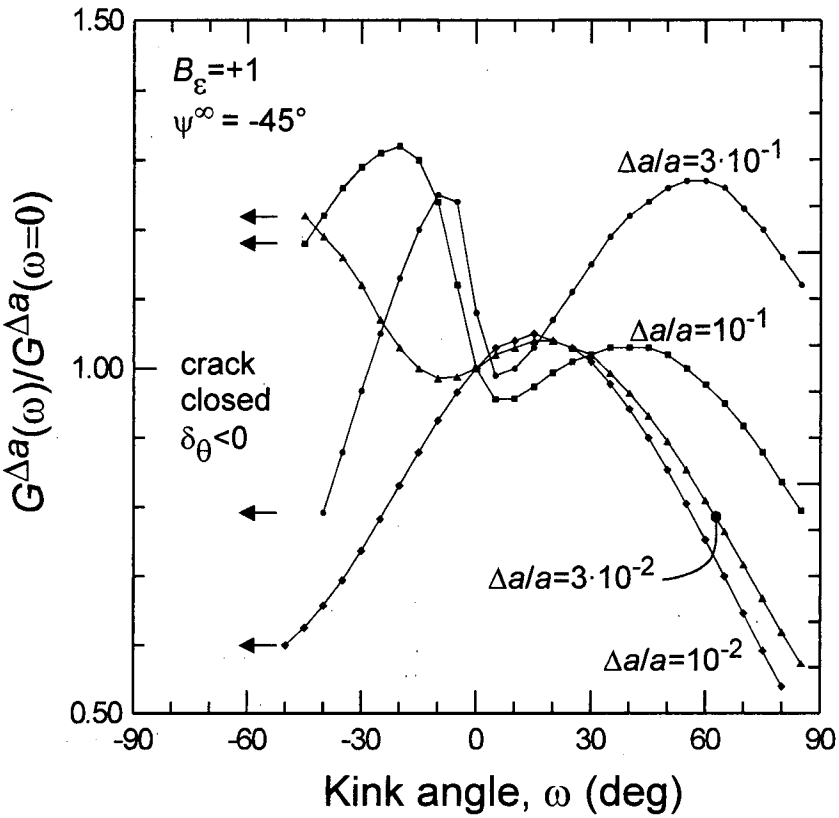

Figure 5.10 The variation of the finite kink energy release, $G^{\Delta a}$, for a range of kink angles, ω, normalized to $G^{\Delta a}$ (ω=0) . Deformation biaxiality, B^e=1 and far field phase angle ψ^∞=-45°. For the shortest kink displayed, $\Delta a/a=10^{-2}$, there is a single maximum, as in homogeneous materials. The competition between the far-field and gradient-induced effects leads to multiple stationary points for longer kinks.

Ernest Orlando Lawrence Berkeley National Laboratory
One Cyclotron Road | Berkeley, California 94720

Prepared for the U.S. Department of Energy under Contract No. DE-AC03-76SF00098